Interactions of high energy mesons with complex nuclei

Welton, Margaret G. E.

INTERACTIONS OF HIGH ENERGY MESONS WITH COMPLEX NUCLEI.

Thesis submitted for the degree of
Doctor of Philosophy
in the University of Durham.

by

Margaret G.E. Welton.

January 1967.

"Interactions of High Energy Mesons with Complec Nuclei".

M.G.E. Welton

Abstract

In order to study further the reaction of 300 MeV π^- mesons with carbon nuclei, it was necessary to acquire with good statistics the energy of the secondaries at different angular intervals. Apparatus was designed and built to support nuclear emulsion plates in a vertical plane around a central target. The apparatus was inserted between the poles of a magnet in a field of 25.5 kilogauss during the exposure. The plates were then area scanned for suitable tracks. A method of analysis was developed especially to cope with the problem of a finite target.

$p\beta$ measurements were also made on secondaries from interactions in a carbon target. The actual incident beam energy was determined and was 285 MeV in both cases. The two sets of results agreed well over the angular interval where comparison could be made. The results

were also compatible with previous experimental results at 300 MeV.

Comparison was also made with the results predicted by a Monte Carlo nuclear cascade calculation (Bertini), but although the energy-angular distributions were almost identical, the momentum distributions at any one specific emission angle did not give good agreement. The observed angular distribution can be explained if the pion is subject to a potential on entering the nucleus, and if the nucleons have a momentum distribution extending up to at least 275 MeV/c. The nuclear well depth is estimated to be on average 53 MeV. An exclusion principle operates preventing pion-nucleon interaction if the nucleon is not thereby raised to the top of the nuclear well.

CONTENTS.

Preface

The aim of the experiments described in this thesis was to find a method of detecting the secondaries from a π-nucleus interaction, and of accurately and rapidly measuring the secondary pion energy so that good statistics could be achieved. A framework to hold and accurately locate emulsion plates was designed and calibrated by Dr. A.J. Apostalakis and the author, and made in the Physics Department workshop. The matrix method of analysis was worked out by Dr. J.V. Major. The computer programs were written and run by the author. The scanning of the spectrographic plates was done by Mrs. E. Errington and the author. $p\beta$ measurements were made by Drs. J.V. Major, A.J. Apostalakis, N.A. Kahn, G.A. Briggs and C. Kitchen. The π beam was located and aligned from the data supplied by the CERN Laboratory, and the exposure made by Drs. J.V. Major, A.J. Apostalakis, P.J. Finney and the author.

LIST OF FIGURES.

LIST OF TABLES.

1. PION INTERACTIONS WITH COMPLEX NUCLEI.

Since the smallest atomic nucleus, that of hydrogen, has approximately nine times the mass of a pi meson, a target pion of sufficiently low energy may see a nucleus as a collection of separate nucleons. Examination of emulsion stacks exposed to meson beams have shown that in the region of 300 MeV pi-nucleus interactions give rise to at the most only one emerging nucleon of high energy, and several protons of low energy. The cross-section for pi-nucleon interaction predicts only one collision between the meson and a nucleon within the nucleus (Finney et al. 1962; Yuan, 1956). This struck nucleon will emerge with a higher energy than the nucleons emitted by the unstable residual nucleus, and hence all the evidence indicates pi-nucleon rather than pi-nucleus interactions as predominating.

In the following report therefore, pi-nucleon interactions will be considered first, followed by an attempt to determine the effect of the nuclear structure on the interaction.

1.1. Summary of Pion-Nucleon Interactions.

The observed interactions of pi-mesons with nucleons at energies below 1 GeV are as follows:-

elastic scattering	$\pi^- + p \rightarrow \pi^- + p$	1.1.1.
	$\pi^- + n \rightarrow \pi^- + n$	1.1.2.
charge exchange	$\pi^- + p \rightarrow \pi^0 + n$	1.1.3.
radiative capture	$\pi^- + p \rightarrow \gamma + n$	1.1.4.

The cross-section for radiative absorption is negligible compared with the first three. It is expected from charge symmetry that $\sigma(\pi^+ n) = \sigma(\pi^- p)$ and $\sigma(\pi^- n) = \sigma(\pi^+ p)$. At 190 MeV, the cross-sections $\sigma(\pi^+ p)$ and $\sigma(\pi^- p)$ show a definite maximum, the $\frac{3}{2} - \frac{3}{2}$ resonance. At 300 MeV the values of these cross-sections are (75 ± 5) mb and (32 ± 2) mb respectively. The latter cross-section including about 22 mb for elastic scattering and 11 mb for exchange scattering (Yuan, 1956).

1.2. Interactions with Complex Nuclei.

Even when a pion interacts only with a single

nucleon within a nucleus through processes 1.1.1 to 1.1.4, the transfer of energy by the meson to the struck nucleon upsets the nuclear equilibrium, and the interaction leaves the nucleus in an excited state.

The impulse approximation assumes that no transfer of energy to the residual nucleus takes place during the time of the collision, and is valid in interactions where the projectile particle on average makes only one collision in the nucleus. If the struck nucleon escapes from the nucleus without making any further collisions, it must have received enough energy to lift it out of the nuclear potential well. The residual nucleus recoils in order that momentum may be conserved, and attains equilibrium by the ejection of particles or photons. When a large momentum transfer to the nucleus occurs, then equilibrium is attained by the ejection of several low energy nucleons, known as 'evaporation particles'. Inelastic interactions with two or more nucleons are possible, especially if the cluster models of the nucleus apply at the interaction energy. An example is the absorption of pi-mesons in the nucleus by the following processes:-

$$\pi^- + p + n \rightarrow n + n$$

and $$\pi^+ + p + n \rightarrow p + p$$

These processes can occur particularly at zero and low kinetic energies.

A meson incident on a nucleus may thus be scattered elastically by the whole nucleus, or react inelastically, being scattered by one or more nucleons, undergoing charge exchange, or being absorbed. A process cannot be completely identified unless all the secondaries can be observed. There is however, no means of directly observing the neutral particles.

As an association of elementary particles the nucleus itself presents many problems, and not least among these is the distribution within the nucleus of these particles, the energy states which they occupy, and the appearance which this entity presents to an incident particle. Probe particles used to examine the nucleus, which appear to interact only with one nucleon, indicate that the nucleons are distributed in momenta. Various models have been proposed to explain the distribution of nucleonic momenta and energies.

a) The Fermi Model. One of the first hypotheses concerning the structure of the nucleus was that the nucleus was a gas of protons and neutrons confined to the nuclear volume. To each nucleon is assigned an energy state and as they are Fermions, no two nucleons can occupy identical states. Furthermore it is assumed that there are no collisions between nucleons. Except at high excitation energies, the gas would be completely degenerate (zero temperature, T=0) and the momentum distribution would be:-

$$N(p)dp = \frac{3p^2.dp.}{P_{max}} \qquad 1.2.1$$

where P_{max} is the Fermi momentum corresponding to the Fermi energy, E_F, and is the maximum possible momentum, determined by the nuclear volume. The Fermi energy is about 25 MeV, ($P_{max} \sim 220$ MeV/c). The total depth of the potential well for protons is about 30 MeV.

b) The Shell Model. This model describes the nucleus by a system of nucleon orbits similar to the electron orbits of the atom. As the nucleons are Fermions the same exclusion rules apply. These nucleonic

energy states or levels may have a specified spatial density, but no momentum density is ascribed to them. However, for an unexcited nucleus the lowest states will be filled, and the Pauli exclusion principle will prohibit interactions involving the transfer of nucleons to already occupied states.

The orbital angular momentum of an energy state is denoted by $\ell = 0, 1, 2, 3$, etc, or the orbital letters s, p, d, f, g..... An orbit or shell is referred to as 1s, 4s, 2p, etc, where the number before the letter is the radial number. Allowing for spin-orbit coupling (Mayer, 1949 and Haxel et al. 1949) the energies of the particles in the shells are split into subshells characterised by $j(= \bar{\ell} + \bar{s})$. For example, in carbon the six protons (or the six neutrons) are distributed as follows, two protons in the $1s_{1/2}$ energy states, and the remaining four in the $1p_{3/2}$ energy states; i.e. $1s^2_{1/2}\ 1p^4_{3/2}$. The four $p_{3/2}$ protons are differentiated by their relative orientation of the j vector.

c) Cluster Models. These models describe the nucleus as configurations of stable units such as alpha

particles or deuterons. The nucleons are thus bound to smaller units within the nucleus, and are more localised than in the Fermi model. This localisation of the target nucleon within the nucleus during impact will give rise to apparent higher momentum components through the operation of the Uncertainty Principle. The cluster models have only limited success in explaining nuclear phenomena, especially in nuclei where all the nucleons cannot be incorporated into alpha or deutron units.

d) The Optical Model. Although the following model does not yield information on the momentum distribution within the nucleus, it provides an invaluable overall description of nuclear interactions. A particle incident on a nucleus can be compared with a light wave incident on a finite medium which both diffracts and refracts the light with absorption of the refracted beam. The nucleus is thus a region of complex refractive index, or complex potential. This model tends to disregard the structure of the nucleus, and hence the density fluctuations across the nuclear volume. It has no means of describing changes which take place in the nucleus due to an interaction, but does give an expression for

the scattered particle in elastic scattering. All other processes are classed as absorption. It also yields only the average values for the cross-section, and ignores any structural effects such as resonances.

The complex potential was first introduced to describe the scattering of nucleons by nuclei, (Fernbach et al. (1949); Feshbach et al. (1954)), and later extended to cover the scattering of alpha particles and mesons. If the nucleus is considered as having a complex potential, then the real part $V'(r)$ introduces a phase difference between that part of the wave traversing the nucleus and the rest of the wave. Interference between these two wave fronts produces diffraction, and absorption of the wave in the nucleus due to $W(r)$ can enhance the diffraction effect. If the complex potential is V, then

$$V = V'(r) + iW(r).$$

The Schroedinger equation and its complex conjugate for an incident particle are:-

$$\nabla^2\psi + 2M/\hbar^2 (E - V' - iW)\psi = 0$$

$$\nabla^2\psi^* + 2M/\hbar^2\ (E - V' + iW)\ \psi^* = 0$$

multiplying by ψ^* and ψ, and subtracting gives -

$$\psi^*\nabla^2\psi - \psi\nabla^2\psi^* = 4M/\hbar^2 . iW \cdot \psi\psi^*$$

i.e. $$\hbar/2iM . \nabla . (\psi^*\nabla^2\psi - \psi\nabla^2\psi^*) = 2W\psi^*\psi/\hbar$$

The left-hand side is the divergence of the probability current, and equals the increase of particle density per unit volume. For absorption this must be negative. On the right-hand side therefore W<0, and the absorption is proportional to the imaginary part of the potential and the particle density.

Nuclear forces are short range, and therefore, as the nucleus is stable, the resultant force at the centre is zero and hence the potential is constant, while at the surface a strongly attractive force operates. The real part of the potential is thus similar to the nuclear density, and an equation of the following form has been widely used

$$V'(r) = -V_o/(1 + e^{(r-c)/a})$$

where c and a are closely related to the corresponding quantities for the nuclear radius.

W(r) is much more difficult to derive. Because of the short range of nuclear forces, it should, like V'(r), be constant in the central nuclear region, and it seems reasonable that absorption by the nucleus should be proportional to the nuclear density. Hence one can use

$$W(r) = -W_o/(1 + e^{(r-c)/a})$$

where c and a are not necessarily the same as before.

There is however an alternative view which considers the operation of the exclusion principle within the nucleus. As the nucleus is a highly degenerate Fermi-Dirac system, the principle prevents the transfer of momentum and energy between particles, which would normally occur due to the strong forces present. In this case the mean-free-path of a particle in the system may be much longer than it would be if the exclusion principle did not operate. However in the surface region this exclusion effect is much reduced, and hence the absorption rate may be higher despite the reduction in nucleonic density. An alternative equation is thus

$$W(r) = -W_o.e^{(r-c)^2/b^2}$$

Again, neither W_o nor c are necessarily the same as in the previous equations. In the absence of experimental determination the former equation is more commonly used to define W(r).

The effect of the potentials is seen when considering the incidence of a beam of particles of momentum p on a nucleus. The beam can be represented as a wave of wave number k (where $k = p/\hbar$), and wavelength λ (where $\lambda = \hbar/p$). As this beam enters the nucleus the wave number changes by k_1, and in the non-relativistic case with a constant nuclear potential then

$$k_1 = k.((1 + V/E)^{\frac{1}{2}}-1) \quad \text{(Fernbach } \underline{\text{et}} \text{ } \underline{\text{al}}\text{. 1949).}$$

In the relativistic case

$$k - k_1 = k(1 + 2.V'/p\beta c + (V'/pc)^2)^{\frac{1}{2}}$$

The effect of the imaginary potential can be represented by the absorption coefficient K ($\propto W$), or the mean-free path for interaction in nuclear matter λ_N (where $\lambda_N = 1/K$).

The absorption coefficient for scattering by a nucleus, where scattering takes place on single nucleons of scattering cross-section σ is

$$K = 3A\sigma/4\pi R^3.$$

where R is the nuclear radius.

Therefore for an incident pion

$$K = \frac{3A}{4\pi R^3}\left(\sigma_{\pi^- p} Z + \sigma_{\pi^- n}(A - Z)\right) \qquad 1.2.2$$

or if capture by nucleon pairs predominates

$$K = \frac{3A\sigma_D}{4\pi R^3} \qquad 1.2.3$$

Experiments on pion-nucleus scattering revealed that the cross-section was not geometric. Two reasons for this have been suggested. One is that the cross-section could be increased by the coulomb effect, the negative mesons being attracted towards the positive nucleus resulting in a cross-section σ_A'.

$$\sigma_A = \pi R^2(1 - [1 - (1 + 2KR)\exp(-2KR)] / 2K^2R^2)$$

(Fernbach et al. 1949)

$$\sigma_A' = \sigma_A\left(1 \pm \frac{2Ze^2E}{R(pc)^2}\right)$$

where E and p are the pion energy and momentum respectively. Alternatively Feshbach and Weisskopf (1949) suggested that the meson had a characteristic "size" equal to the reduced de Broglie wavelength λ yielding the new cross-section σ_A''.

$$\sigma_A'' = (\sigma_A^{\frac{1}{2}} + \pi^{\frac{1}{2}}\lambda)^2$$

At low energies where λ is large, the correction will be important and the nucleus will lose all its transparency as the size of the pion will be comparable with σ_A. Having measured the cross-section, and obtained K from equations 1.2.2 or 1.2.3, then the imaginary potential W can be calculated

$$W = \tfrac{1}{2}.hcK\beta$$

The change in wave number k_1 on entering the nucleus can be determined from the angular distribution of the scattered particles, and hence V' and W can be calculated.

1.3. Experimental Results.

a) Nuclear Momentum Distributions. Some of the earliest work which indicated a momentum distribution of the nucleons, was work on the formation of deuterons, where a nucleon from the nucleus unites with the incident nucleon. From observations of the emission angle and energy of the deuteron, the momentum distribution of the target nucleons can be obtained. The fermi distribution (eq: 1.2.1) for nucleon momenta with E_F = 25 MeV did not produce the observed deuteron distribution, and from data where the target nucleus was C^{12}, the following distribution was derived, where N(p) is the number of nucleons with momentum p.

$$N(p) = \frac{8\pi \alpha}{(\alpha^2+p^2)^{\frac{1}{2}}} \qquad 1.3.1$$

(Chew and Goldberger, 1950)

with α^2 = 18 MeV.

A distribution was needed which would provide a high momentum component, which the Fermi distribution does not possess, and such a distribution had already been

derived from proton-nucleon scattering, where it had been assumed that the high momenta were contributed by the strong interactions between a pair of nucleons.

$$N(p) = \frac{e^{-p^2/\alpha^2}}{\alpha^2 \pi^{3/2}} \qquad 1.3.2$$

(Henley, 1952)

with $\alpha^2/2M \sim 14$.

The above equation (1.3.2) fitted the experimental results for deuteron pick-up satisfactorily.

Simultaneously the results of many nucleon-nucleon scattering experiments were being explained by the hypothesis of a distribution of nucleon momenta in the nucleus.

In one such experiment 314 MeV protons were incident on C^{12}, and the scattering and proton-nucleon cross-sections for scattering were determined. Attempts were made to fit the data using a Chew - Goldberger distribution (eq: 1.3.1), and an equation of the form

$$N(p) = C_A((\alpha^2+p^2)^2 \ (\beta^2+p^2)^2) \qquad 1.3.3$$

where $\beta = 2.5\ \alpha$, and C_A is a normalisation factor.

The above momentum distribution gave an average kinetic energy of 48.1 MeV for the nucleons, whereas a Fermi distribution with a P_{max} of 200 MeV/c would have an average kinetic energy of 12.8 MeV, which was not compatible with the experimental results. However, the best fit was acquired with a gaussian distribution (eq: 1.3.2), which gives an average kinetic energy of 19.3, but any exclusion effect was ignored since it was expected to be observable only in the beam direction (Henley, 1952).

In later work (Winsberg and Clements, 1960) examining the theory of nucleon-nucleon scattering, it was assumed that the nuclear particles had the same nucleon-nucleon cross-sections as they would have had in the unbound state. The only alteration being due to the Pauli exclusion principle. Isotopic elastic scattering in the region 10 MeV - 6 GeV was investigated. Consideration of a Fermi gas of nucleons with E_F of 18.8 - 33.4 MeV, led to the conclusion that the data required an E_F of 48.1 MeV which implies a P_{max} of 303 MeV/c for the nucleons, which is far above the accepted range of values.

Extensive investigations of the nucleonic momentum distribution have been made using quasi-elastic scattering. This is scattering of an incident particle by a bound nucleon, which at the moment of impact is considered to act as a free particle with its nuclear momentum.

Before 1958 quasi-elastic p-p scattering was already being considered as a means of obtaining information about the nuclear structure (Maris et al. 1958). The nucleons were considered to make only one collision within the nucleus, and thus needed a high energy and small de Broglie wavelength. It was decided to use closed shell nuclei with assumed j-j coupling in the shells. If the last shell is not filled, the collision can leave the residual nucleus in one of many states so that the energy balance is not unique. The exclusion principle would not have an observable effect for incident nucleons of above 400 MeV. The results obtained in a quasi-elastic experiment were expected to be similar to those from deuteron pick-up except that the latter probably favoured surface nucleons and hence higher momentum components, whereas quasi-elastic

scattering would sample throughout the nucleus. The method involved the simultaneous detection of two secondaries of equal energies and emission angles ($\sim 45°$ to beam direction) when a proton beam was incident on light nuclei. A series of such experiments were carried out in different laboratories.

At 185 MeV the binding energies for the s and p shells of light nuclei were measured (Tyren et al. 1958). These are compared in Table I with values obtained by other workers performing similar experiments and within the estimated errors the results agree. A table of the experimentally determined values of the binding energies of light nuclei has been drawn up by Ajzenberg-Selove et al. (1959), which includes the Tyren et al. results.

Among attempts to fit momentum distributions for the nucleons in these experiments were the following. For 660 MeV protons on beryllium and C^{12}, the Fermi distribution was rejected outright because of the lack of high momentum components, and three other distributions were tried (Azhgirey et al. 1959).

Projectile energy	Target	Binding energy p shell. MeV.	Binding energy s shell. MeV.	Reference
155 MeV	Li^6	4.5 ± 1.5	20.3 ± 1.5	a
155 MeV	Li^7	10.2 ± 1.6	23 ± 1.5	a
185 MeV		10 ± 1.5	24 ± 1.5	b
185 MeV	Be^9	18 ± 1.5	25 ± 1.5	b
155 MeV	B^{10}	7 ± 1.1	31.5 ± 1.5	a
		13 ± 1.2		
155 MeV	B^{11}	10.4 ± 1.6	34 ± 3	a
		15.2 ± 1.7		
		14 ± 1.5	37 ± 5	b
155 MeV	C^{12}	15.8 ± 1.2	34.5 ± 1.5	a
158 MeV		17		d
185 MeV		16		e
		17 ± 1.5	35 ± 1.5	b
185 MeV	N^{14}	8 ± 1.5		b
		16 ± 1.5		
185 MeV	O^{16}	12 ± 1.5		b
		19 ± 1.5		

Results of proton quasi-elastic scattering.

a) Garron *et al.* (1962)
b) Tyren *et al.* (1958)
d) Gottschalk and Strauch (1960)
e) Gooding *et al.* (1960)

TABLE I

1) a gaussian. $N(p) \propto e^{-p^2/\alpha^2}$ 1.3.4

with $\alpha^2/2M$ = 16, 18, 20 and 22 MeV.

2) a Selove distribution. $N(p) \propto e^{-p^2/\alpha_1^2} \pm 0.15 e^{-p^2/\alpha_2^2}$

with $\alpha_1^2/2M$ = 7 MeV, α_2^2 = 50 MeV. 1.3.5

3) sum of two gaussians. $N(p) \propto e^{-p^2/\alpha_1^2} + e^{-p^2/\alpha_2^2}$ 1.3.6

The best fit was in fact obtained using 1.3.6 with $\alpha_1^2/2M$ = 16 MeV, $\alpha_2^2/2M$ = 50 MeV and β = 0.09. For copper and uranium targets multiple collisions prevented detection of the nucleon energy.

For light elements with 155 MeV incident protons the following two distributions were tried as a result of a preliminary Born approximation calculation.

for the s shell. $N(p) \propto e^{-p^2/\alpha^2}$ 1.3.7

for the p shell. $N(p) \propto (p/\alpha)^2 . e^{-p^2/\alpha^2}$ 1.3.8

By adjusting α a satisfactory fit was obtained for the energy distribution of the secondaries, the final values of α are shown in Table II.

α in MeV	Li^6	Li^7	B^{10}	B^{11}	B^{12}
s shell	110	115	120	120	160
p shell	110	70	80	90	95
Garron et al. (1962)					
p shell					74
Gottschalk & Strauch (1960)					

Experimental determinations of α for nucleon momenta distributions

$$N(p)\alpha \quad e^{-p^2/d^2}$$

TABLE II

1.3.6 was used successfully to explain the quasi-elastic interactions of 660 MeV protons on C^{12} (Zhadonov and Fedotov, 1961).

The quasi-elastic scattering interaction

$$p + C^{12} \rightarrow Be^{8} + p + \alpha$$

has been studied at 150 MeV. Rejecting free helium collisions the momentum distribution of the emitted α was studied for a fixed momentum transfer, $q = 2.0$ fm^{-1} and $E_{\alpha} = 22.5$ MeV. It was concluded that the ground state of C^{12} probably could be described completely in terms of α cluster model, but the experiment was not accurate enough to derive an expression for the α momenta, (James and Pugh, 1962).

Further in the reaction

$$p + C^{12} \rightarrow p + n + C^{11}$$

the recoil momentum will be equal in magnitude and opposite in direction to the target nucleon momentum before the collision. For incident proton beams of 0.25 to 6.2 GeV the recoil momentum was independent of

the incident energy and corresponds to an average kinetic energy of 19 MeV, which agrees with the deuteron pick-up results, (Sarjant Singh and Alexander, 1962).

Deuteron sub-units in the nucleus have been studied using the reaction

$$\gamma + N \rightarrow N' + p + n$$

where the momenta of the out-going particles can provide information about the quasi-deuteron momenta. Further, the reaction

$$\gamma + N \rightarrow N'' + p$$

yields information about the binding energy of the protons. To form deuteron sub-units the nucleons should be within a radius $\hbar/\mu c$ (μ is the pion rest mass), and this is more probable for nucleons belonging to the same shell than for those from different shells. Kim (1963) examined the experimental results existing for C^{12}, assuming that the pairing for 1s nucleons was stronger than for the 1p ones. He obtained the following distributions and binding energies

1s nucleons $E_B = 20$ MeV

$$N(p) = (3\pi M)^{-3/2}\exp(-p^2/3M) \qquad 1.3.9$$

1p nucleons $E_B = 5$ MeV

$$N(p) = (2\pi^{-\frac{1}{2}}/3)(10M)^{-5/2}\exp(-p^2/10M) \qquad 1.3.10$$

deutrons $N(p_D) = (0.37\ \exp(-p_D^2/4ME_1)/(4\pi ME_1)^{\frac{1}{2}}$

$$+ 0.82\ \exp(-p_D^2/4ME_2)\ /1.5\ (4ME_2)^{2.5} \qquad 1.3.11$$

where $E_1 = 1.5$ MeV $\quad E_2 = 5$ MeV

The different quasi-elastic proton-proton experiments give compatible results for the binding energies of the nucleons in the s and p shells of the light nuclei. These binding energies of 10 - 30 MeV are not completely contradicted even when deuteron subunits only are considered as in Kim's work. Both the deuteron pick-up experiments and the incident proton work at 0.25 to 6.2 GeV suggest an average nucleonic kinetic energy of 19 MeV which is inconsistent with the Fermi distribution.

Finally the distribution of nucleon momenta indicated by both deuteron pick-up and quasi-elastic scattering from 100 - 660 MeV is of a gaussian form with α always in the region of 100 MeV.

b) Nuclear Potentials. In the quasi-elastic scattering experiments, no accurate determination of the potential has been made. Table III shows the only measured values.

It has been pointed out by Strnad (1962) that although distributions of the form shown in 1.3.7 and 1.3.8 can, with a suitable choice of α , be fitted to the cross-section curves, estimates of the binding energy based on these distributions differ greatly from the measured values. Using the observed binding energies and potential well form factors, curves were fitted to the results of Garron et al. for Li^7 and C^{12} with the radius of the potential well, r, as the variable parameter. The nuclear potential can then be estimated from the equation, and in fact the potential radii which gave the best fit almost coincide with radii found by high energy electron scattering (see Table IV).

Projectile	Energy	Target	Potential in MeV.	
p	660 MeV	Be	30	Azhgirey et al.1959.
		C^{12}	30	
p	0.25 - 6.2 GeV	C^{12}	37 - 45	Sarjant Singh and Alexander, 1962.

Estimations of the Nuclear Potential from Experimental Results.

TABLE III

	By experiment		From equation		Variable parameter	
	B_s MeV	B_p MeV	V_s MeV	V_p MeV	r_s fm	r_p fm
Li^7	23.5	10	43	25	2.5	4.5
C^{12}	36	16	79	40	1.6	3.4

B - binding energy

V - potential well depth

	re_{ff}(fm)	r_{equ}(fm)
Li^7	3.5	3.5
C^{12}	2.94	3.0

re_{ff} - effective potential radius

r_{equ} - equivalent radius from electron scattering (Hofstadter, 1956)

TABLE IV.

1.4. Pauli Exclusion Principle Effects.

a) General Outline. The Pauli exclusion principle forbids any two Fermions to occupy identical energy states.

The effect of the exclusion principle on the refractive index of nuclei at high energies was examined by Glauber (1956). Glauber stated that to find the effective scattering properties of nucleons in nuclei, it is better to use the position correlations of the particles in the Fermi gas than their momentum distribution. Correlation which keeps similar particles apart, leads to destructive interference effects, and at low energies the nucleon-nucleon cross-sections in the opacity expression are smaller than the free particle cross-sections. At high energies ($\lambda <$ nucleon-nucleon range) shadowing and multiple scattering effects also become important. In this case the tendency of nucleons to stay apart increases their effectiveness as collision targets. Therefore the nucleon-nucleon cross-sections for nuclear opacity are greater than the free nucleon-nucleon cross-sections by a term proportional to

$$\frac{i.f^2(0).\ p^2_{max}}{p^2}$$

where p is the initial momentum.

This term changes sign when

$$Im|f(0)|^2 = Re|f(0)|^2$$

The effect of nucleon separation is exactly the inverse to that which causes non-additivity of cross-sections, as for example in deuterium, where the nucleons are drawn together.

Examining proton collisions with a 30 MeV proton beam, Elton and Gomes (1957) concluded that the exclusion principle does not operate in the diffuse rim of the nucleus where the nucleons are almost free, and their momentum can be represented by a gaussian function (e.g. 1.3.2).

The exclusion principle tends to freeze particle motion and to minimise the effects of the excitation of small clusters (Bruecker, 1958). If however, all the lowest energy levels are not filled, small momentum transfers can take place, moving nucleons into unoccupied

positions. Alternatively the nucleus can be considered as a Thomas-Fermi gas, where the density is given by

$$\rho(r) = 2/h^3 . \ 4\pi/3 \ . \ p_F^3(r) \qquad 1.4.1$$

where $p_F(r)$ is the maximum momentum at radius r.
If $N > Z$, then the neutron density has a larger radius than the proton density (Oda and Harada, 1958).
Electron scattering data indicate that

$$\rho(r) = a(\exp((r-c)/b) + 1)^{-1} \qquad 1.4.2$$

where a is a normalisation factor, c is the half-way radius, and b is a diffuseness parameter with b = 0.57 f and $c = 1.1xA^{1/3}f$. $p_F(r)$ can be obtained from 1.4.2 and 1.4.1. Estimating the potential for an incident proton, the differential cross-section for scattering can then be calculated. In the nuclear region chosen, the exclusion principle was found to make no difference to proton-nucleon scattering at 31 MeV, and fairly satisfactory agreement was obtained with the experimental points.

In estimating the effect of the exclusion principle at high energies Karplus and Yamaguchi (1961) used a

gaussian momentum distribution for uncorrelated nucleons (incident energies 300 MeV). Their value of α was 168 MeV/c (see 1.3) for incident nucleon energies between 15 and 26 GeV. They neglected the effect of nuclear binding on cross-section except to the extent which the Pauli exlcusion principle and coherent effects, reduce the quasi-elastic scattering at very small angles. They obtained a distribution width

$$\frac{p.\theta.p_{max}}{M}$$

for the secondary nucleons at angle θ due to the Fermi motion of the nucleons, and then considered a degenerate Fermi distribution making a gaussian approximation to the average fraction, f, of states not available to a nucleon when it receives an impulse $p\theta$.

f is given by

$$f = \left(1 - \frac{p\theta}{2p_{max}}\right)^2 . \left(1 + 1/4 . \frac{p\theta}{p_{max}}\right)$$

$$\sim \exp\left(-1.25 . \frac{p^2\theta^2}{p^2_{max}}\right)$$

$$= \left(-\frac{5}{2} . \alpha . p^2\theta^2\right)$$

Scattering at angles such that $p\theta \gtrsim 2p_{max}$ is only slightly reduced, but the amplitude of the momentum spectrum is reduced by a factor $(1 - \exp(-5p^2\alpha\theta^2/2))$. This gives the same effect as if the struck nucleons were smaller scatterers than free nucleons.

Watson and Zemach (1958) performed a Monte Carlo calculation for pions incident on a nucleus. They found an effective mass for the pion, as the dispersive nature of the medium alters the magnitude of the pion flux and the density of the states. However, their calculations did not agree with experimental results.

Further calculations have been carried out for π-nucleon scattering, above 600 MeV, which disagree with Watson and Zemach's results. The calculations indicate an increase in cross-section due to the exclusion principle, and in the limit agree with Glauber's earlier calculations. They also give good agreement with the experimental results in this region (Baqui Bég, 1960).

b) 300 MeV Meson Interactions with Complex Nuclei. Continuing observations on the interactions of π^- mesons in complex nuclei, this laboratory analysed the scattering

of a 300 MeV π^- beam incident on a G5 emulsion stack. Previously at 750 MeV and 4.2 GeV the optical model of the nucleus was used to explain the results and satisfactory agreement was obtained using a reduced meson size (Allen et al. 1961; Clarke and Major, 1957). At 300 MeV (Finney et al. 1962) and 88 MeV (Allen et al. 1959) however, the value of K, the absorption coefficient, obtained differed greatly from the theoretical value.

For 300 MeV the observed value of K was 3 to 4 times smaller than the expected value. 140 metres of track were scanned, and 255 elastic events including 42 disappearances were found. Thus the mean-free-path for elastic scattering ($\geqslant 5°$) was (77 ± 5.8) cm. The forward-backward ratio, F/B, is the ratio of the number of mesons emitted in the forward direction, that of the incident beam, to the number emitted in the backward direction. The value obtained experimentally was $F/B = 0.74 \pm 0.17$ for stars with secondary mesons. Misclassification would increase the elastic mean-free-path by a maximum of 12% and decrease the inelastic mean-free-path by 5%.

The mean interaction cross-section in emulsion is

$$\bar{\sigma} = \Sigma (N_i \sigma_i)/\Sigma N_i \qquad 1.4.3$$

where there are N_i nuclei/cm of the ith element whose interaction cross-section is σ_i.

Using the observed inelastic mean-free-path, 1.4.3 and 1.2.3, a value for K was obtained

$$K = (1.5 \pm 0.15).10^{12} cm^{-1}.$$

which gives $\lambda_N = 6.7 \pm 0.7.\ 10^{-13}$cm, and an opacity of 66%. Thus the mean-free-path in nuclear matter is calculated to be (1.5 x nuclear radius).

Calculations performed with the individual free nucleon cross-sections (75 ± 5.6 and 32 ± 2 see earlier) give $K = (5.2 \pm 0.3).10^{12} cm^{-1}$.

Because of the long mean-free-path in nuclear matter only one scattering of the projectile is expected to occur, and therefore the relative probabilities of scattering and absorption are 30% and 70% respectively. Adding the expected values of K (scattering) and K (absorption) in these proportions leads to an expected

value which agrees with the observed value.

$$K = K_{scatt} + K_{abs} = (1.9 \pm 0.2).\ 10^{12} cm^{-1}$$

The average kinetic energy of the secondary mesons was 107 MeV (corresponding to E = 250 MeV and p = 205 MeV/c). For secondary pion energies greater than 85 MeV, then the average kinetic energy was (164 ± 26) MeV, and the F/B ratio was (1.1 ± 0.35), which corresponds to the following nuclear potential components:-

$$V'(r) = (25 \pm 1)\ MeV$$

$$W_o(r) = -(14 \pm 1)\ MeV$$

The observed and calculated K values could be brought into agreement only if r was reduced to $1.12.10^{-13}$cm, when the values were both $9.3\ 10^{12} cm^{-1}$. However this value of K would imply that the meson makes on average about five collisions in the nucleus. Also this high value for K predicts an average energy for the secondary mesons of about 70 MeV, not the observed 107 MeV, and the value for r_o is outside the accepted

range. The results are consistent therefore with a single collision within the nucleus, with absorption not scattering as the predominant feature. The cross-section for interaction of a meson with a single nucleon is however smaller by a factor of 3.

If the mean energy of the scattered π^- mesons is plotted against the laboratory angle of scattering, then in the forward direction the energy is found to be much lower than would be observed if the struck nucleons were stationary. This suggests that small momentum transfers are forbidden, and that the exclusion principle is operating within the nucleus. Describing the nucleon states within the nucleus using a Fermi momentum distribution, it proved impossible either to account for the reduction in cross-section of about 3, or for the F/B ratio of about unity (Finney et al. 1962; P.G.J.T. Parkhouse, M.Sc. Thesis, Durham University).

1.5. Monte Carlo Calculations.

Metropolis (1958) performed nuclear cascade calculations for heavy nuclei, Al, Bi, U, etc. The

earlier calculations were made for incident protons and neutrons of 82 to 365 MeV, and were general Monte-Carlo calculations picking a point of entry to the nucleus, and then following the particle until absorption occurred or it escaped. The Fermi model of a degenerate gas was used to describe the nucleus, comprising a nuclear volume whose radius was $R = rA^{1/3}$. The degree of forbiddenness of a collision depended on whether or not the resulting energy of the nucleon was less than E_F. Overall good agreement was obtained both quantitatively and qualitatively with the experimental results.

The calculations were then extended for incident energies of up to 1.8 BeV and incident pions, pion production, scattering and absorption were included. The calculated emission angle spectra of protons agreed well with the experimental results except at angles $< 10°$. However, for pions the emission spectra did not agree. At smaller angles of emission the calculations gave far too many high energy pions, which had the effect of raising the average kinetic energy. In fact, the experiments indicated that small energy transfers were

being prohibited thus reducing the forward scattering. For example, for 500 MeV π^- incident on heavy emulsion nuclei the calculated average kinetic energy was 174 MeV, but the observed average was 110 MeV. For 162 MeV π^- a similar discrepancy was observed, but it was not as great.

An attempt was made to follow a suggestion of Nikol'skii's (1957) and to introduce a pion-nucleon potential. With an attractive potential of 18 MeV the agreement was better for the energy spectrum of the secondaries. Any secondaries with negative kinetic energy were assumed to be absorbed. However, the angular distributions still did not agree, and the calculated distribution was not isotropic enough. It was thought that the introduction of a diffuse nuclear boundary, also suggested by Nikol'skii, might remedy this.

Bertini (1963) followed up this work by introducing such a nuclear boundary effect into the calculations. The diffuse nuclear boundary was approximated to, by dividing the nucleus into three concentric spheres of decreasing density as the radius increased. In each region the nucleus was assumed to be behaving as a

degenerate Fermi gas, but the overall effect approximated to a gaussian distribution with a kT of 15 MeV. This agreed well with experimental results (see 1.3), and it appears that the detected distributions are partly the effect of varying nuclear density.

Here, the pion potential was assumed to equal the potential of the struck nucleon, and again collisions were forbidden, if a nucleon energy occurred below E_F. The results agreed well with experimental data for incident nucleons as long as $A < 12$, except that again more small momentum transfers were expected than observed. The pion data however, showed large discrepancies, the most extreme being for charge exchange. It was postulated that the discrepancy might be due to the incoherence indicated by the resonance in the pion-nucleon cross-section.

1.6. Pion Potentials

In 1958 Watson and Zemach performed a series of calculations, which gave the momentum of the pion within the nucleus. This momentum had two components, and from

this it was possible to calculate the pion potential corresponding to a particular pion kinetic energy. Their calculations were for the 10 to 400 MeV region. Their results however, only gave qualitative agreement with experimental data.

Nikol'skii (1957) estimates the pion potential for a kinetic energy of 160 MeV as $V = -(24 \pm 6)$ MeV. The minus sign indicating that the potential is attractive. It was also found that a change in V of 30 MeV led to a change in kinetic energy of 7 MeV for backward scattered pions. In Table V a list of experimentally determined pion potentials are shown. Within experimental error the values are consistent, but the accuracy is not high.

1.7. Reasons for this Experiment.

It is obvious that theory and experiment do not agree on the results of pion interactions with complex nuclei. Previous work at 300 MeV (see 1.4) had shown that the optical model was not applicable, and no explanation of the results other than that a Pauli effect might be responsible for the discrepancy, could be found.

Experimentally Determined Pion Potentials

Energy	Particle	Target	V	V_i
48	$\pi^{\pm}$	C	$-(15 \pm 15)$	
62	π^-	G5	-	~ -19
80	π^+	G5	-	~ -24
120	$\pi^{\pm}$	G5	-	~ -24
70	$\pi^{\pm}$	C	~ -18	~ -9
78	$\pi^{\pm}$	Cu	$\sim -(35 - 40)$	~ -20
80	π^+	Al	~ -20	$\sim -(10 - 25)$
80	π^-	Al	$\sim -(30 - 40)$	-
88	π^-	G5	$-(28 \pm 3)$	$-(32 - {}^{+20}_{-6})$
300	π^-	G5	(25 ± 1)	$-(14.1 \pm 1.4)$
60	$\pi^{\pm}$	He	$-(20 \pm 10)$	-
62	$\pi^{\pm}$	C	-18	-
105	$\pi^{\pm}$	He	$-(18 \pm 14)$	-
125	π^-	C	-30	-

All values in MeV.

Values taken from tables in

Nikol'skii *et al.* (1957)

Allen *et al.* (1959)

Finney *et al.* (1962)

TABLE V

However, in order to be able to construct a model for the struck nucleons it is necessary to have more accurate data on the emitted pions. This means measuring large numbers of inelastic scatters quickly and accurately.

Making normal pβ measurements on secondary tracks from interactions is a slow process, as each track has to be aligned along the traverse of the stage. Scattering measurements and grain counts have then to be made on the track in order to identify it, and if the tracks are steep, passing rapidly into another plate, measurements are impossible. Often the track cannot be resolved as definitely belonging to a pion, but could be that of a charged particle of higher mass. Also in cases of charge exchange, positive and negative pions cannot be distinguished.

The spectrograph, described in chapter 2, uses a magnetic field to sort the charged particles. Thus using an incident pion beam, only a negligible number of the secondaries which have negative curvature will not be pions. Also using this method, of the order of 100 tracks per scanner per day, can be measured.

The experiment was thus planned in the hopes of

obtaining energy and angular distributions with good statistics. From these distributions, the discrepancies between the experimental results and the prediction of a particular model, could be accurately determined, and the model altered or rejected accordingly.

1.8. Basic Calculations made for the Present Experiment.

These calculations were based originally on a classical model of the nucleus as an association of isotropically moving nucleons. A pion of momentum π_1, and energy W, is incident on this nucleus, and collides with a nucleon, moving with momentum P and energy Wp, at an angle α to the direction of motion of the pion. The resultant momenta and angles of emission can then be calculated.

The centre of mass of the two particles is found, and the cross-section corresponding to the centre of mass momentum of the pion is calculated, using the differential cross-section $(d\sigma/d\Omega)$ of 1.9, and the equation

$$d\sigma^{\pm} = 2.\ \sin\alpha.d.\alpha.\sin\theta.\frac{d\sigma}{d\Omega}.\pi./(\text{number of angular intervals}) \quad 1.8.1$$

where θ is the angle of emission.

A table is then drawn up showing the cross-section for scattering into a certain angular interval with a given momentum for that value of P. Each table contained the total cross-section for 18 values of α from 0 - 180°. The calculations were then repeated using a different P. P ranged from 25 → 475 MeV/c in 50 MeV/c intervals and α in 10° intervals from 5° upwards.

Three nucleon momentum distributions were assumed, giving the fraction F with momentum P.

a) the Fermi with $F = 3.P^2.dP/P^2_{max}$

with $P_{max} = 240$ MeV/c.

b) the gaussian with $F = 2.e^{-p^2/\alpha^2}.dP/\pi^{\frac{1}{2}}.\alpha.$

with $\alpha = 191$ MeV/c.

c) a composite with $F = 4.P^2.e^{-p^2/\alpha^2}.dP/\pi^{\frac{1}{2}}.\alpha^3.$

with $\alpha = 191$ MeV/c.

Sets of cross-section tables were then produced for each distribution. Summing over all tables for a distribution gave the total cross-section.

Cut-offs could then be applied by forbidding collisions in which the secondary momentum or energy of the struck nucleon failed to satisfy some chosen condition.

The calculations were carried out originally on the Ferranti Pegasus computer at the University of Newcastle-on-Tyne. Subsequent adaption of the cross-sectional tables was done on the Elliott 803 computer of Durham University.

1.9. Pion Interaction Cross-Sections.

In order to calculate the effect of the Pauli exclusion principle in π-nucleon collisions, detailed information on the π-nucleon cross-section is required.

For a pion incident on a free nucleon, the differential cross-section in the centre of momentum at an angle θ, can be represented by the following series

$$\frac{d\sigma}{d\Omega} = A + B.\cos\theta + C.\cos^2\theta + D.\cos^3\theta + \ldots . \quad 1.9.1$$

where A, B, C, etc. are functions of the phase shifts at the energy under consideration. It is possible to obtain expressions of the form

$$A = a + bq + cq^2. \qquad 1.9.2$$

for each of these functions, where a, b and c are numerical constants, and q is the momentum of the pion. The terms of 1.9.1 are of decreasing importance, and only the first three or four need be considered.

In order to obtain the constants a, b and c, and thus be able to calculate the differential cross-section, experimental values for A, B, C and D were plotted for various values of q. These experimental values were obtained from the following papers:- Deahl *et al.* (1960, 1961), Kellman *et al.* (1963), Zinov and Korenchenko (1959), Ashkin *et al.* (1956, 1957), Helland *et al.* (1962) and Yuan (1956). The curves were plotted for both π^--P collisions (Fig. 1a) and π^+-P collisions (Fig. 1b). Assuming charge independence the π^+-P curves also apply to π^--N collisions. The constants were found for equation 1.9.2 by curve fitting to the experimental

Cross-section π^--P scattering.

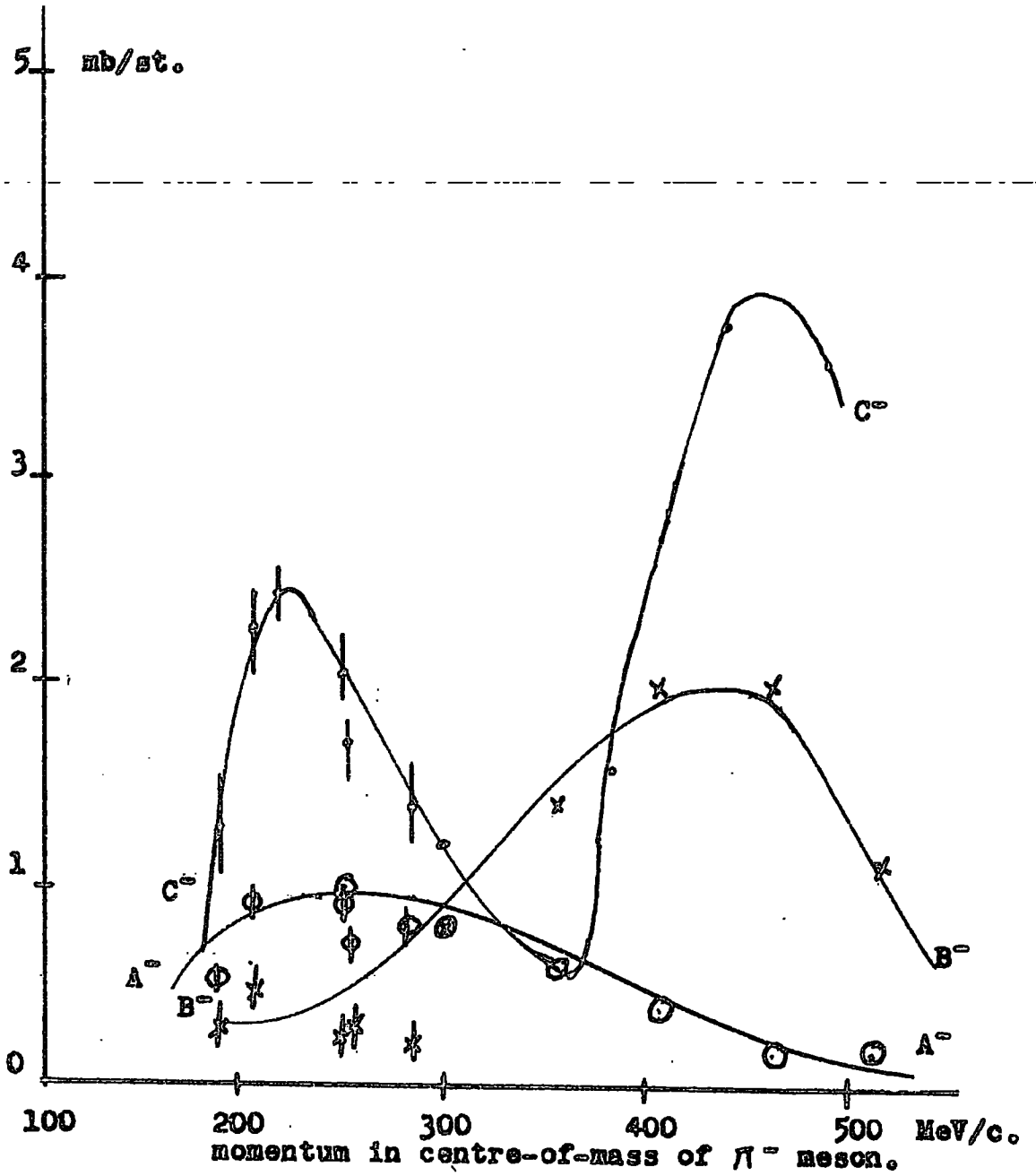

Figure 1a

Cross-section π^+-P scattering.

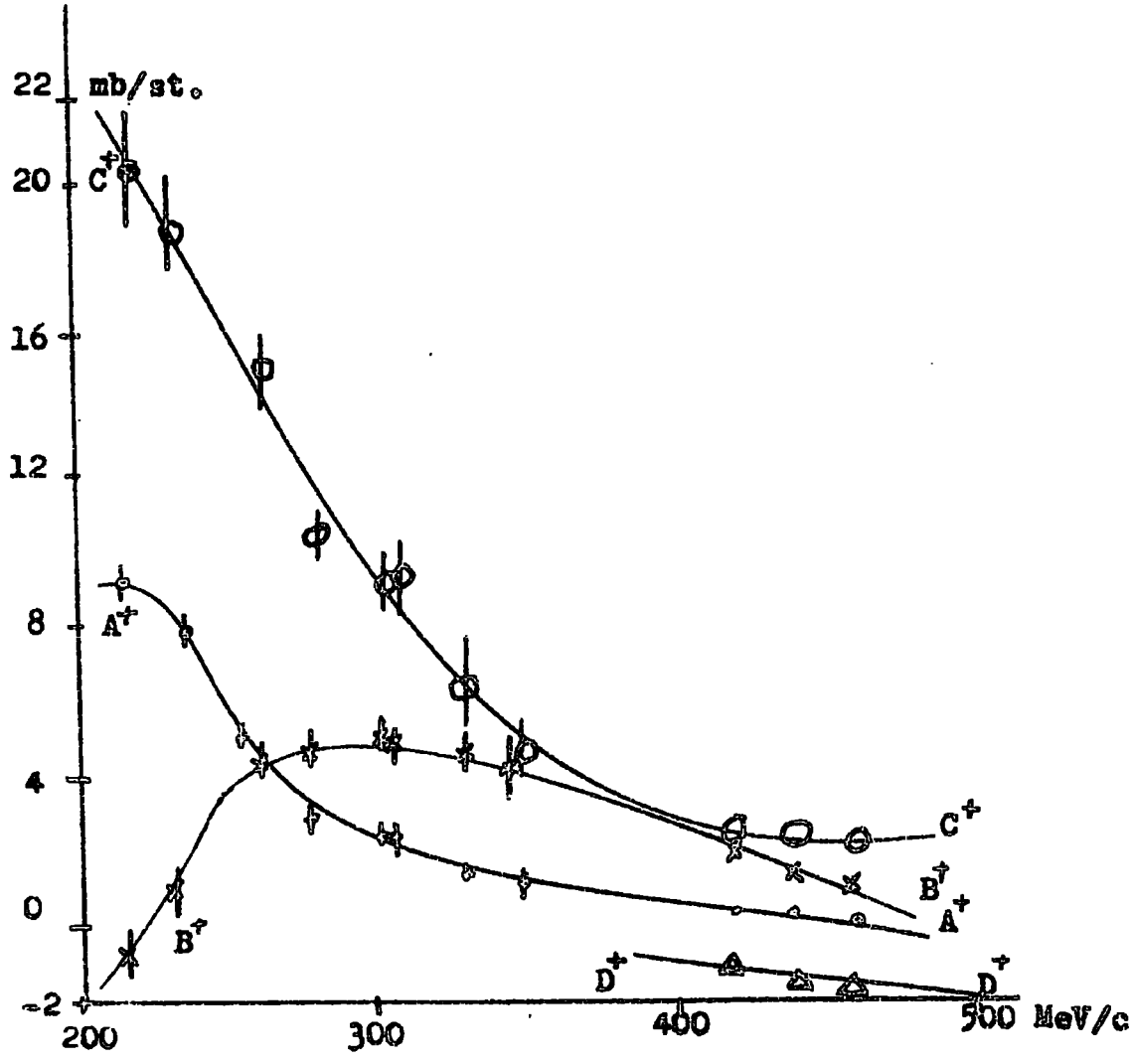

Figure 4b.

q range in MeV/c	f_i	a	b	c
$q < 270$	A	-15.997	+0.29850	-0.00082
	B	-30.203	+0.13453	0
	C	-0.368	+0.32098	-0.000986
$q < 250$	D	0	0	0
$250 < q < 355$	D	-1.724	+0.029	-0.000088
$270 < q < 460$	A	+29.565	-0.13209	+0.000150
$270 < q < 355$	B	-22.128	+0.17528	-0.0002735
	C	+76.36	-0.3235	+0.000349
$355 < q < 460$	B	+12.30	-0.01481	-0.0000114
	C	+61.27	-0.2810	+0.000349
	D	+41.096	-0.2218	+0.00028

where $f_i = a + bq + cq^2$.

and the f_i are the phase shift functions in the equation for the differential cross-section.

TABLE VI

points. The expression for pi-nucleons cross-section is the sum of π^-P and π^-N cross-sections. The constants for A, B, C and D are shown in Table VI for the various ranges of q.

1.10. Some Results of the Calculations.

a) Effect of nucleonic momentum distributions on the scattering of pions. In figure 2a, is shown the energy of the pion as a function of scattering angle resulting from a pion collision with a stationary nucleon, at a pion energy of 300 MeV. Compared with it are the mean energies of pions for scattering angles determined from the calculations outlined above. In the calculations the collisions are with moving target nucleons. It is found that for the Fermi and the composite Gaussian distributions, the mean energies are almost exactly equal to each other, and very close to that of a pion scattered from a stationary target.

The differential cross-section for scattering on a stationary nucleon becomes modified as seen in figure 2b,

where the nucleon is allowed to move according to the Fermi and composite Gaussian distributions.

b) The effect of the nuclear potential. The nuclear potential experienced by pions has been described in table V (section 1.6) and is shown in figure 2c. In the same figure, the relation between kinetic energy within and without the nucleus is shown. The potentials were determined experimentally for several nuclei, and it is assumed that they are constant throughout the periodic table. Since the potential varies with energy, it introduces a considerable modulation on the mean energy of the scattered pions.

A primary pion of 285 MeV is reduced to 260 MeV inside the nucleus. Therefore the scattering of a 260 MeV pion is the reaction being investigated. Using the Oxford Kinetic Tables, the energy of the secondary pion within the nucleus can be found after the collision with a stationary nucleon. As this pion leaves the nucleus there is a further potential effect which can be estimated using figure 2c. The expected modulation for a pion-stationary nucleon collision is shown in figure 2a,

Variation of Mean Energy with Scattering Angle.

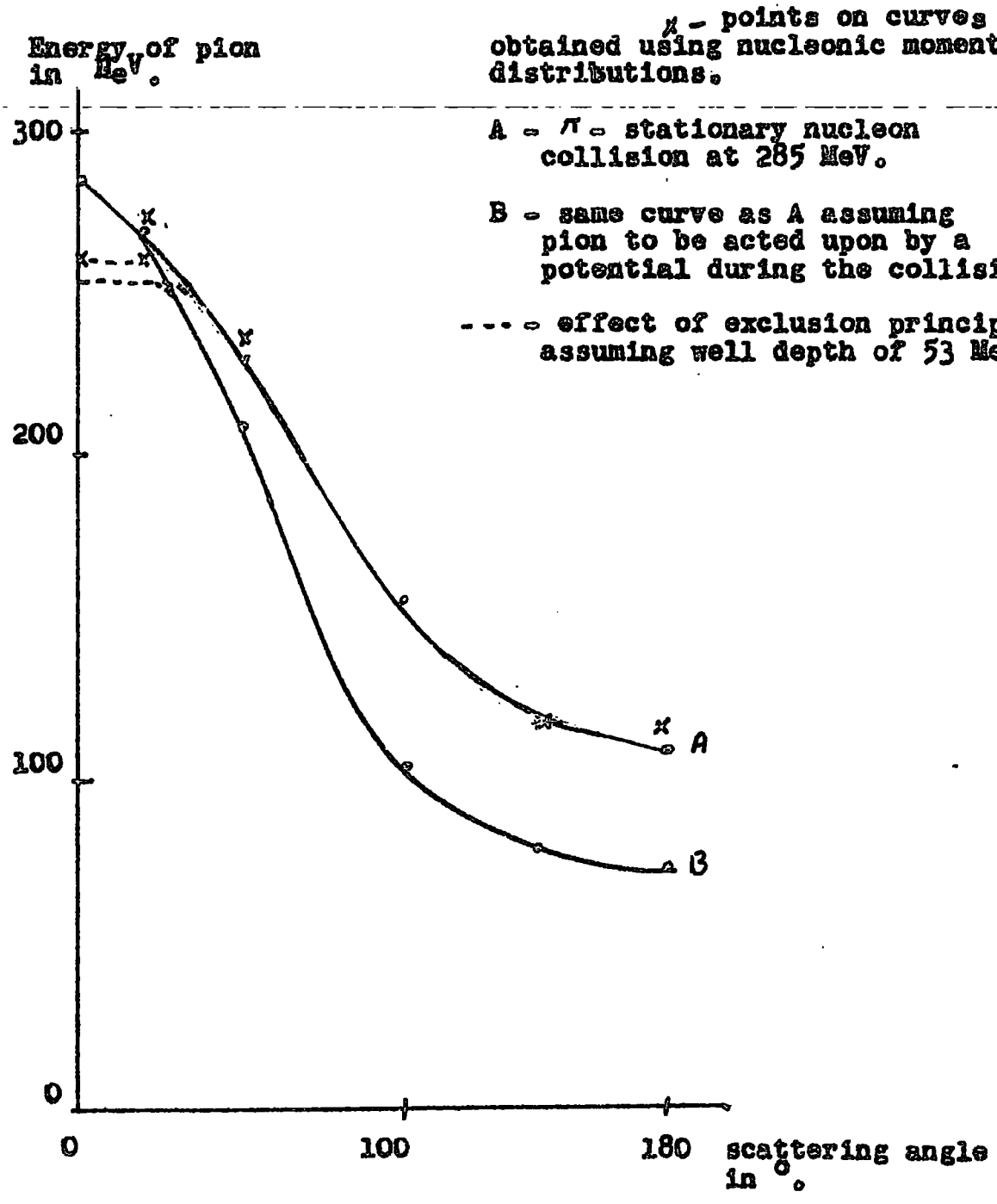

Figure 2a.

Variation of Cross-section with Scattering Angle.

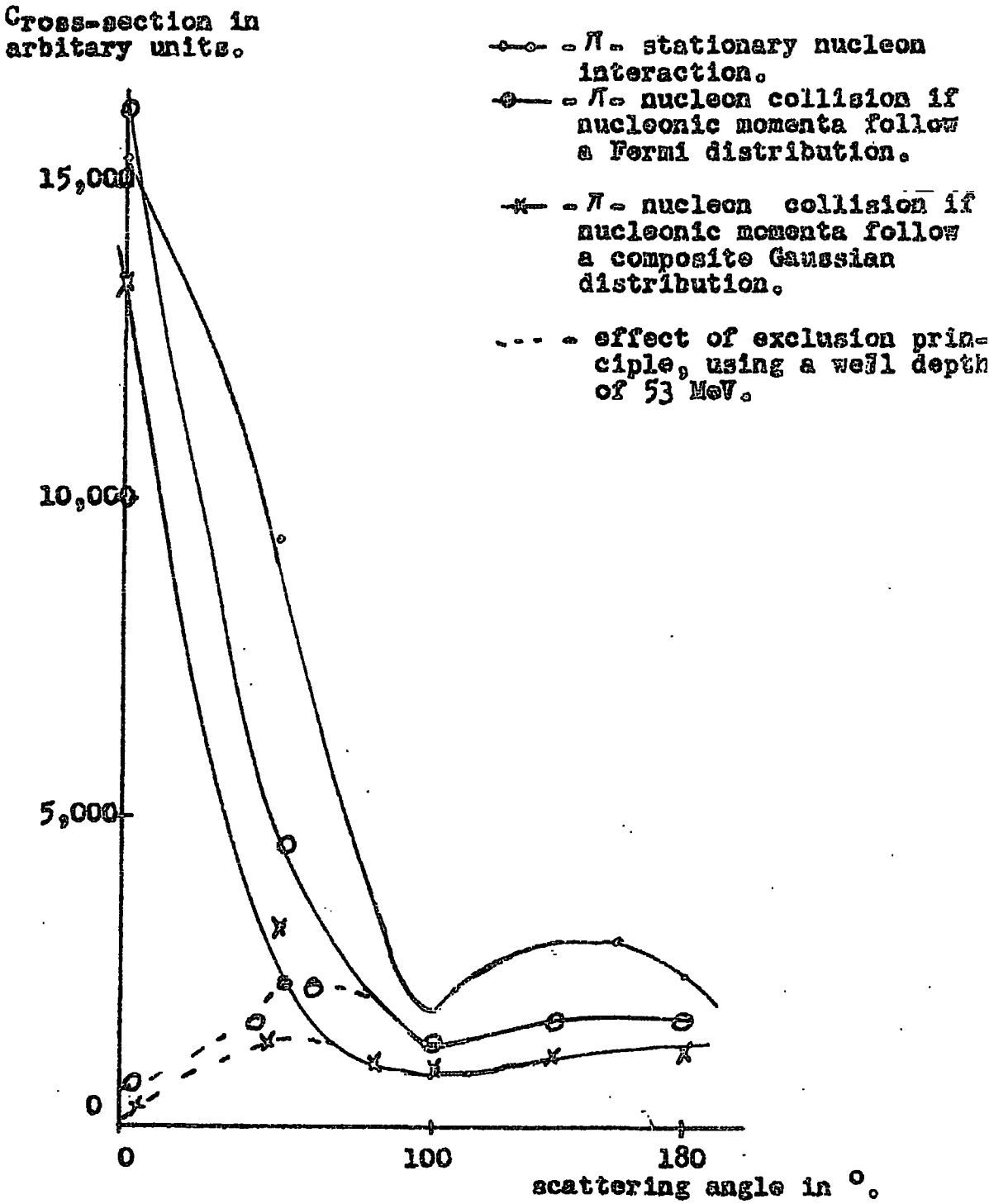

Figure 2b.

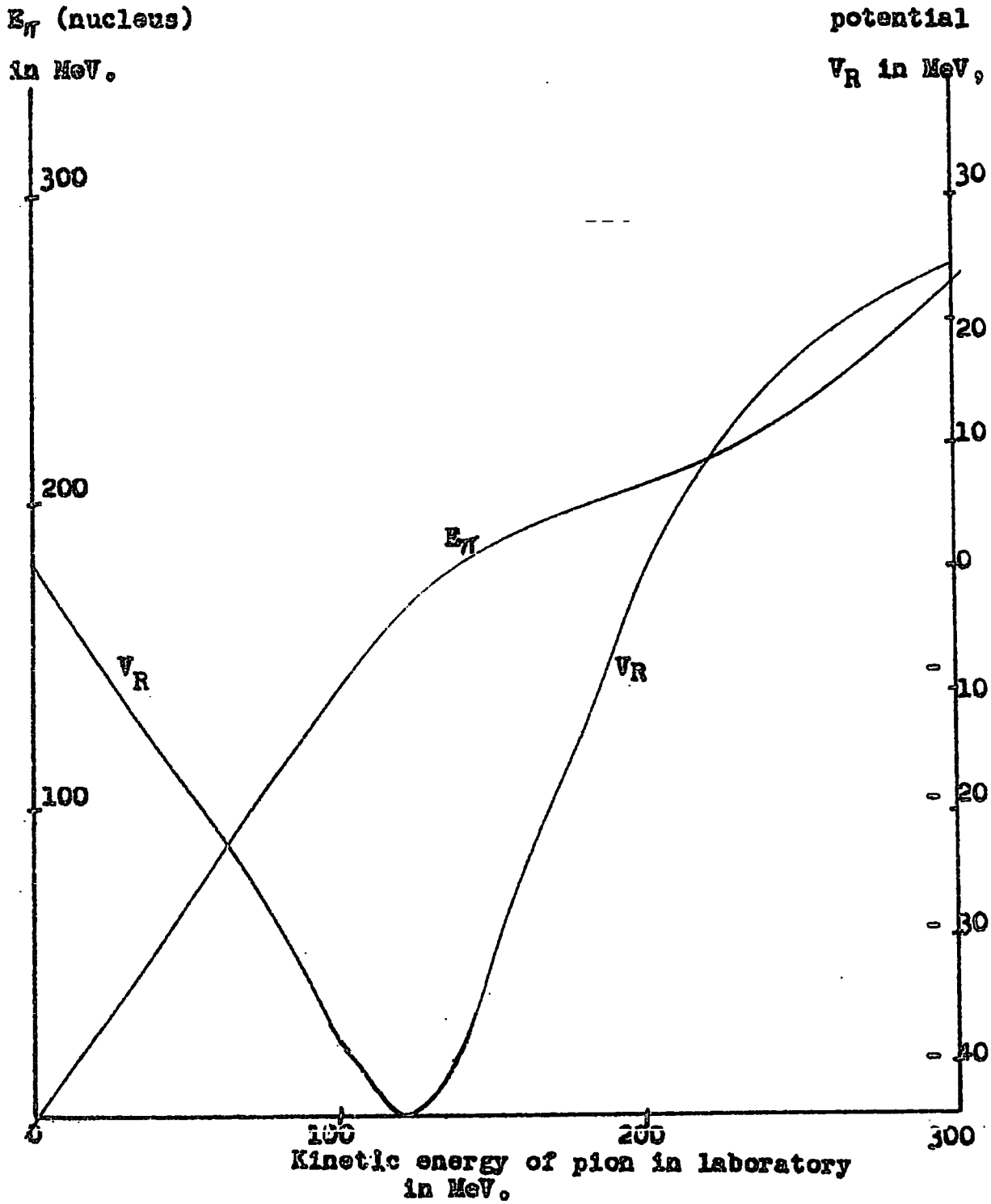
E_π (nucleus)
in MeV.
potential
V_R in MeV.
300
200
100
0
30
20
10
0
-10
-20
-30
-40
E_π
V_R
V_R
0
100
200
300
Kinetic energy of pion in laboratory
in MeV.

Figure 2c.

where it is seen to be most pronounced at larger angles of scattering. In a similar manner using the assumed momentum distributions, the potential effect can be determined, and the modulation of the mean energy curve is in fact the same whether the nucleons are considered to be stationary or distributed over a momentum range. The modulation depends on the shape of the potential curve in figure 2c.

c) Exclusion effects. The exclusion principle inhibits small momentum transfers of momentum, so that it depresses the scattering through small angles. For the Fermi and composite Gaussian ($p^2e^{-p^2/\alpha^2}$) distributions the effect is shown in figure 2b, where the reduction of forward scattering is plainly seen. Using the Fermi model, the reaction was assumed forbidden under different conditions. If a momentum restriction was assumed, such that the nucleon must be raised to 240 MeV/c if the reaction was allowed, a decrease of the forward cross-section was obtained, but not of the mean energy. The other two momentum distributions tried gave the same result.

If a nucleonic potential well is assumed of depth V, then the energy required by the nucleon to escape is (V- K.E.), where K.E. is the kinetic energy of the nucleon in the nucleus. Using the exclusion principle, a collision will be forbidden if the energy transferred to the nucleon is not enough to allow it to escape. An example of such an energy limitation is shown in figure 2b, where it can be seen that the effect becomes negligible at around 70°. In figure 2a, the effect on the mean energy of the scattered pions is shown.

d) Distribution of momenta at a fixed angle of scattering. The effects of momenta distributions of the struck nucleons is seen to be negligible if average effects are considered. For example, the mean energy and mean cross-section of the scattered pion are virtually unchanged. However, the differential cross-section is smeared out. So are the individual momenta of the secondary pions as is shown in figure 2d. Here as an example, the scattering of 290 MeV pions through 90° is shown. The effect of the momentum distribution is to broaden the line spectrum by about $\pm$ 150 MeV/c.

Momentum Spectrum at a Given Scattering Angle.

Expected spectrum at 90^0 of secondary pions, if the nucleons have a composite Gaussian distribution of momenta with a maximum p around 275 MeV/c. No corrections have been made for potential or exclusion effects. Incident pion momentum is 290 MeV.

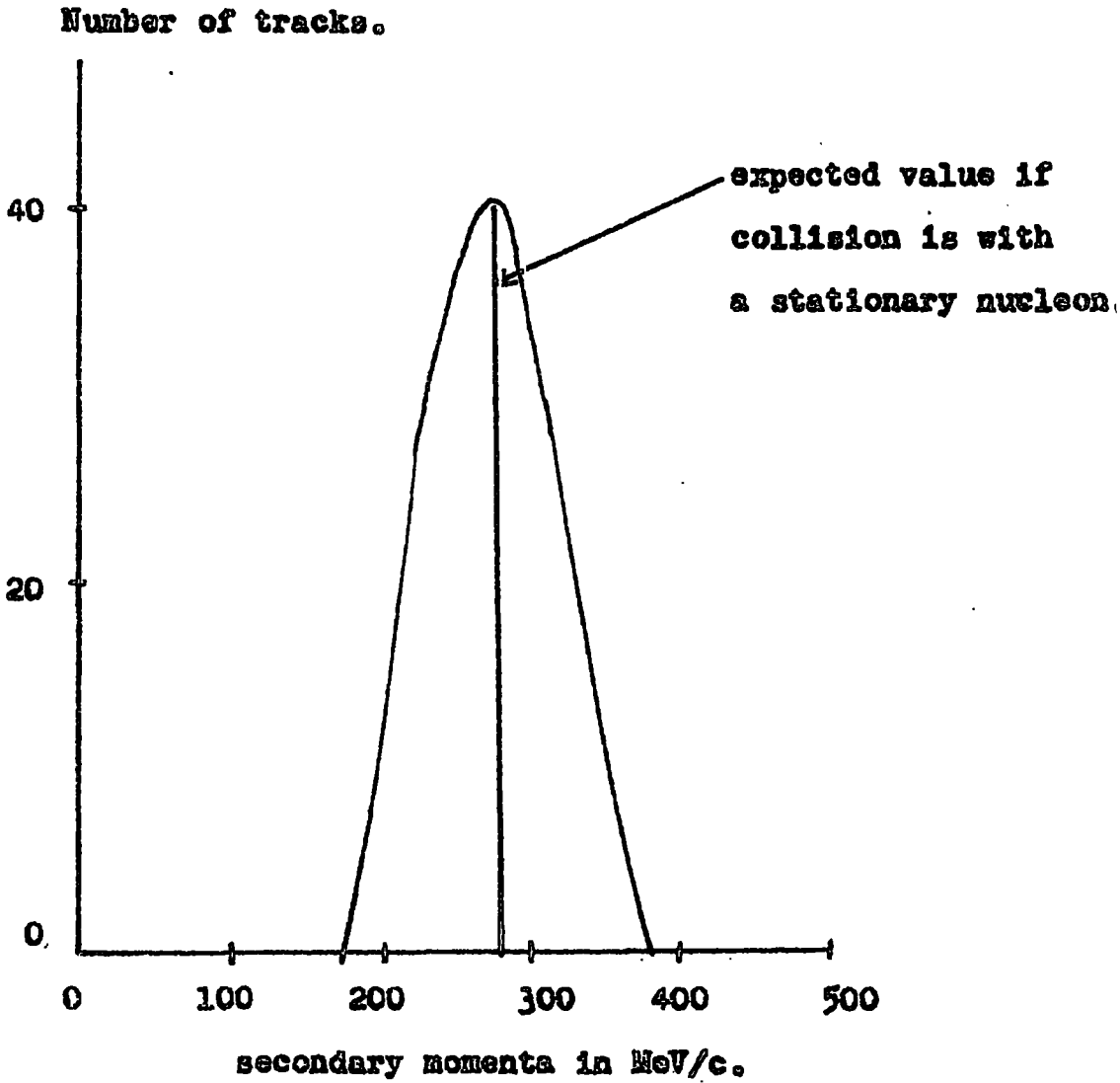

Figure 2d.

Exclusion effects which are small at 90° have been excluded.

2. THE SPECTROGRAPH.

2.1. The Principle of the Spectrograph.

As was stated in the first chapter, section 1.7, the emission angles and momenta of the secondaries from a pi-nucleus interaction are required with good statistics. The ideal system would have cylindrical symmetry and would consist of a point target set in a magnetic field and surrounded by a circular detecting device. The detecting device in this case being flat sheets of nuclear emulsion in the plane of the magnetic field.

The beam enters the system and strikes the target. The secondaries then strike the emulsion at an angle to the perpendicular to the surface, and pass through, out of the spectrograph. Knowing the central target point and the angle of the track in the emulsion, it is possible to determine ε the angle of emission. If ε is the horizontal, and ε' the vertical component of the angle of emission, then:-

$$\cos\varepsilon = \cos\theta \cdot \cos\varepsilon' . \qquad 2.1.1.$$

By placing the spectrograph in a magnetic field an estimate of the particle momentum p, can be made. A singly charged particle in a magnetic field of strength H, will describe a circular trajectory with radius of curvature R, perpendicular to the field direction, where:-

$$p = 300.H.R. \quad eV/c \qquad 2.1.2$$

If ρ is the chord of this circle from the target, O, to the point of contact with the emulsion, Z, (see Fig. 3b) then:-

$$\sin \phi = \rho/2R. \qquad 2.1.3$$

and from 2.1.2 and 2.1.3 -

$$p = \frac{300.H\rho.}{2.\sin \phi}$$

With a known magnetic field, H, p can be calculated if ρ and ϕ are determined by measurement.

The presence of the magnetic field will give antitropic curvature to the tracks of oppositely charged particles. Thus from the angle in the emulsion it will

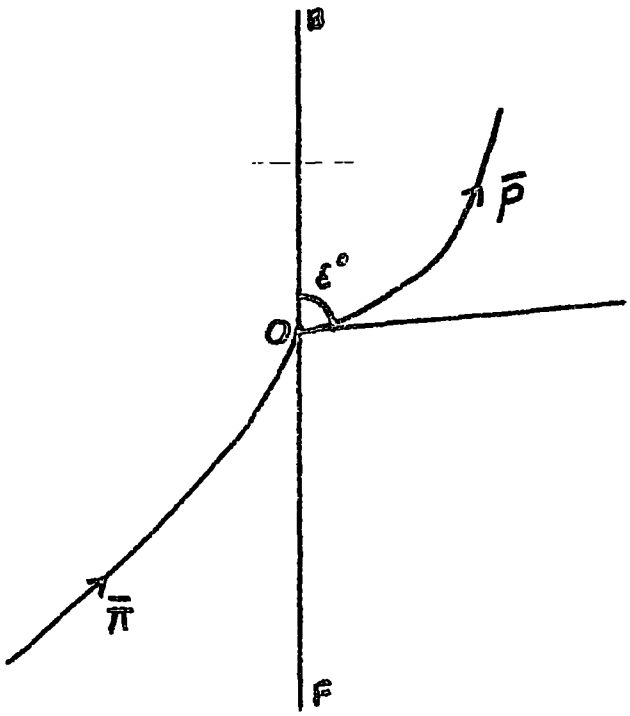

BF = the perpendicular to the target face.

O = the point of scattering in the target.

FIG: 3a. Horizontal Plane of Interaction.

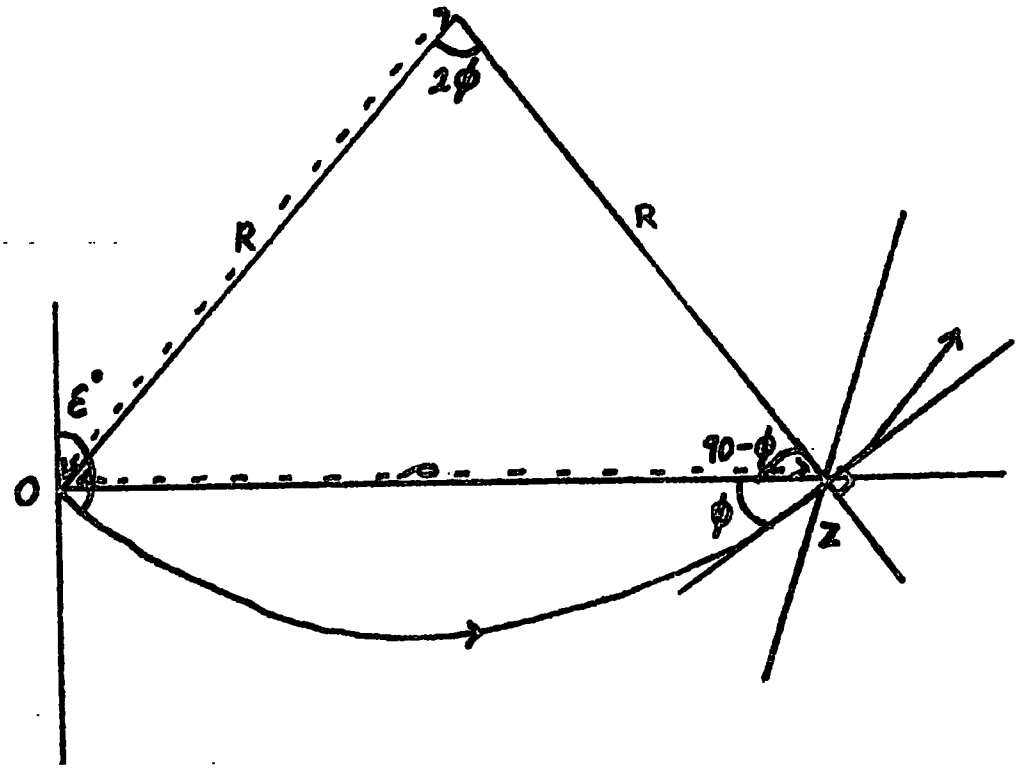

O = point on the target.

Z = point on the plate.

FIG: 3b. Trajectory of a Particle in a Magnetic Field.

be possible to distinguish the tracks of negatively charged particles and to make measurements only on these tracks. Therefore pions which undergo charge exchange are automatically excluded.

With regard to the magnetic field, there were two requirements, a steady constant value over the area of the spectrograph and a value high enough to render the curvature of the tracks easy to detect and measure. It was obvious that the smaller the radius of the spectrograph the easier it was to have a constant value for the field strength over the experimental area, but the deflection of the particle would be very small and the curvature of the track hard to detect. Also the finite size of the target necessitated having a large radius (see below). The value of the field required was of the order of 10 kilogauss.

Particle Flux. One of the most important factors affecting the choice of the radius of detection, is the flux per unit area of detector. If the incident pion flux on a target of thickness t, is F, then the total path length is Ft. Therefore the number of inelastic events giving rise to secondaries is:-

$$\frac{Ft}{\lambda}$$

where λ is the interaction path length. If d is the radius of the circle on which the detectors are set, the flux per unit area per pulse is -

$$\frac{Ft}{\lambda\ 4\ \pi\ d^2}$$

The maximum tolerable flux is about 2.10^3 particles per cm. The time to obtain this is then -

$$\frac{\lambda\ 4\ \pi\ d^2.2.10^3}{Ft}$$

This time should be as short as possible in order to keep the background low, and so that the experiment is feasible with regard to the use of a beam from a high energy accelerator for this exposure. Obviously once F is the maximum possible, the time depends on the ratio between d and t. This ratio is very important because on it depends also the size of the error in the determination of p (see later). If t is large compared with d then the errors on both p and E increase.

The highest flux of 300 MeV negative pi-mesons was obtainable from the C.E.R.N. synchrocyclotron, where a beam of the order MeV had already been built. The flux was quoted at about 4.10^4 π^- per second over an area of 6 x 8 cm^2. On a target of 2 x 2 cm^2, this is 4.10^3 π^- per second. λ for inelastic scattering is 3 x 38 cm (for scattering with an emergent pion), and taking d as 5 cm and t as 1 cm, this requires an exposure time of 6 hours; whereas for the same t but with d increased to 10 cm, the exposure time is 22 hours. Hence in adjusting d and t to the practical optimum some sacrifice in accuracy was necessary in order to achieve better statistics and vice versa.

2.2. The Actual Spectrograph.

In practice the ideal system of a central point target surrounded by a circular detector can only be approximated to. The aim is to set a finite target in the centre of a circle of frames, which support flat nuclear photographic emulsion in a vertical plane (see Fig. 4). Each frame supports a glass coated on both

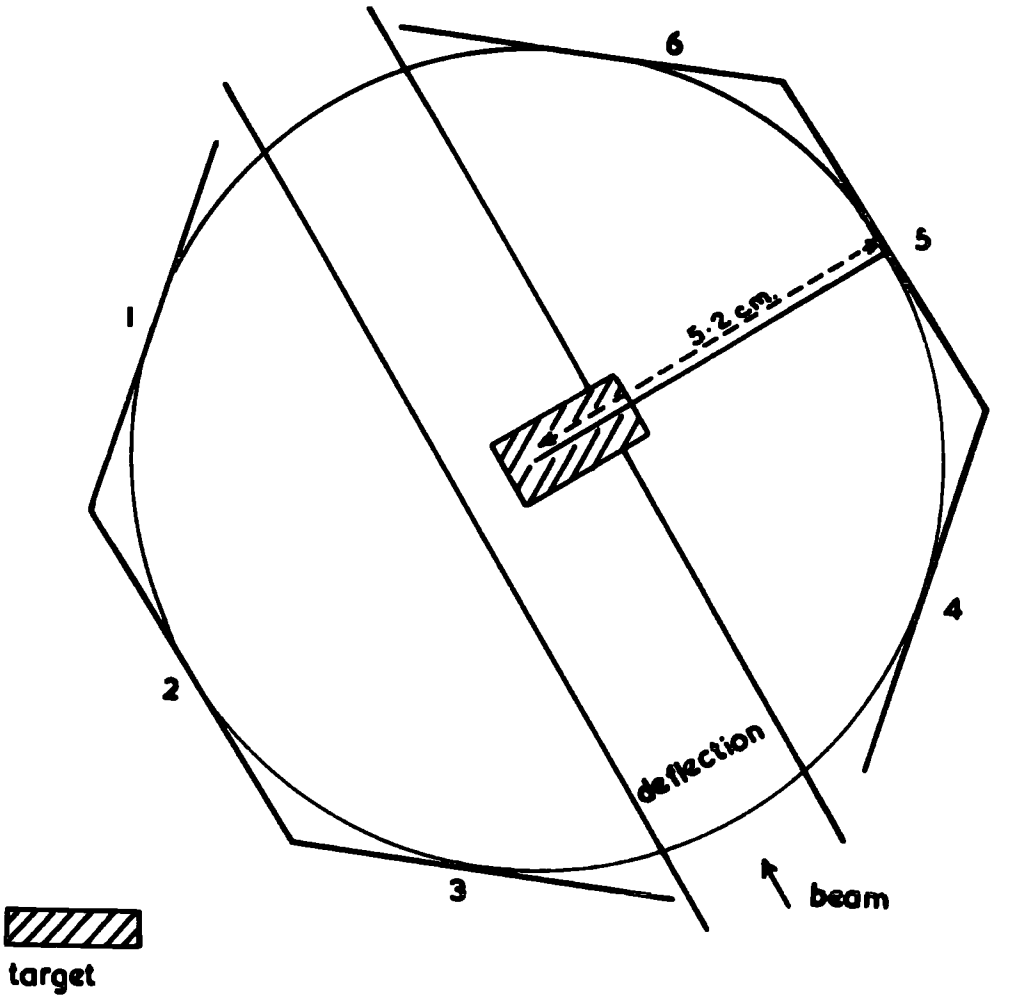

Diagram showing layout of

six plates and target

Target dimensions are 2cm x 1cm x 5cm.

Figure 4

sides with nuclear emulsion. The position of each frame must be located accurately, so that a frame can be removed, and replaced in exactly the same position. To achieve this accuracy a three point locating system was used.

Each frame is set along a tangent of the detection circle, radius d. The equations in section 2.1. have to be modified, since they assumed cylindrical symmetry. Let θ now be the angle in the horizontal plane which the track makes with the perpendicular to the plate at the point of entry, Z, (see Fig. 5a). It is necessary to determine for each plate both d, the length of the perpendicular from the target to the plate, and the position D, where this perpendicular reaches the plate. For each track then, θ, and x the horizontal co-ordinate of the track relative to D, can be measured. Thus -

$$\tan(\theta - \phi) = x/d. \qquad 2.2.1.$$

and ϕ is the only unknown in the equation. Also

$$\rho = (x^2 + d^2)^{\frac{1}{2}} \qquad 2.2.2.$$

and by substituting for ρ and ϕ in 2.1.4 p can be found

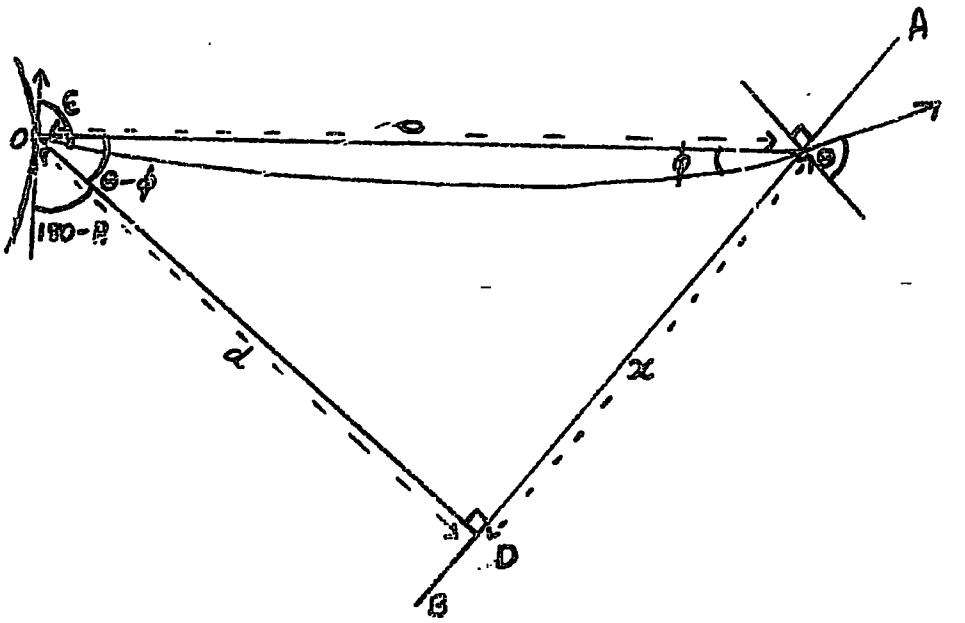

a) The Geometry of the Trajectory in a Horizontal Plane.

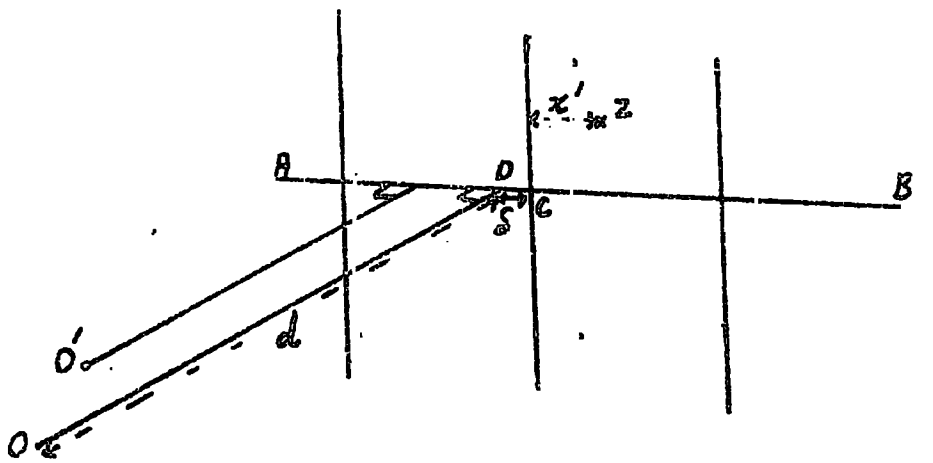

b) Co-ordinates of a point Z.

Figure 5.

if the point of emission is known (see chapter 4).

ε' can be obtained from measurements on the track in the emulsion since the vertical angle is unaffected by the magnetic field. Let d make an angle A with the emerging unscattered beam. Then

$$\varepsilon = A - (\theta - \phi) - \phi \qquad 2.2.3.$$

θ and ϕ may be positive or negative depending on the charge of the particle and the segment of the detecting circle in which the frame is located. In fact it is no longer possible by simple visual inspection to separate positively from negatively charged particles (see Fig. 6), for two reasons. Firstly, the fact that the frame lies along a tangent to the detection circle means that tracks reaching opposite edges of the frame appear to have different curvature even when they have the same momentum. Secondly, because the target has a finite size, if all tracks are assumed to have come from the target centre then some negative particles will appear positive and vice versa (see chapter 4).

Once d has been determined, ε and p may be estimated

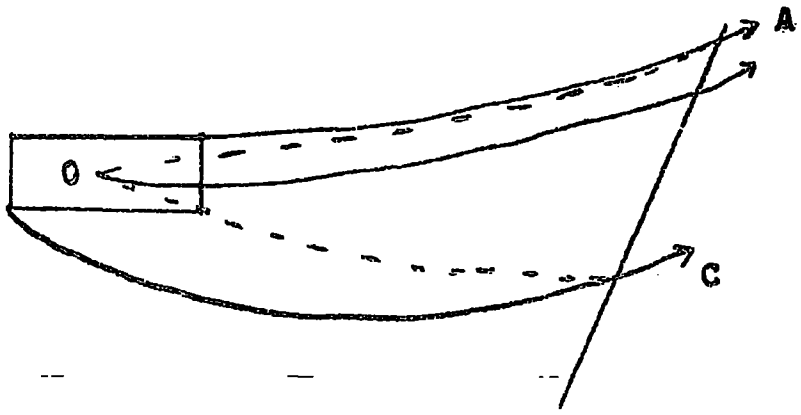

a) The effect of emission from a different centre. If all are considered as coming from O, then A is estimated to have a different curvature and C a higher momentum than is the actual case.

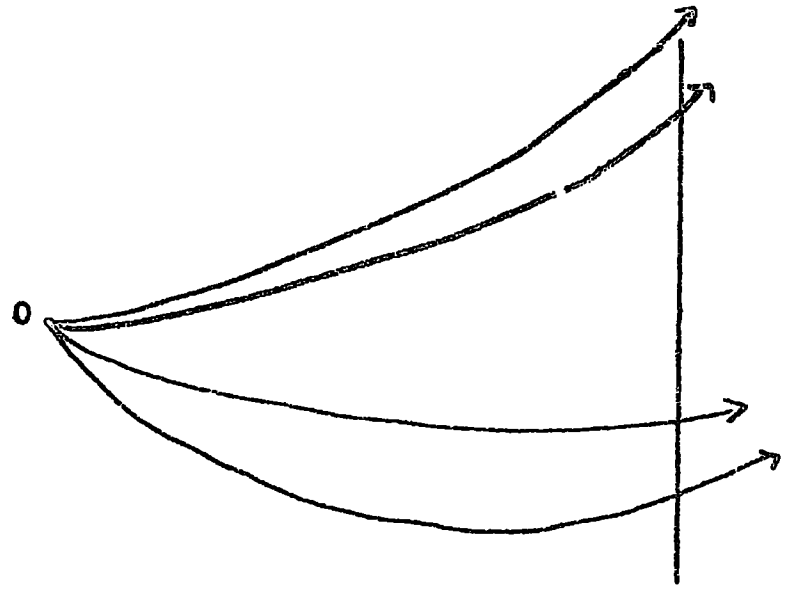

b). Pairs of particles emitted at the same spatial angle with different momenta.

Figure 6.

from the co-ordinate measurements made for each track.

Accuracy

Misalignments of the frames. Small misalignments of the frames would very quickly introduce large errors into the evaluations. Examples of misalignments are shown in Fig. 7, where A-B is the emulsion plane.

In a) θ is the actual angle of the track with the perpendicular to the emulsion, if the plate is correctly aligned. When misaligned by $\delta\phi$ the error in momentum is given by:-

$$P = p\left(1 - \frac{\sin\theta}{\sin(\delta\phi + \theta)}\right)$$

and if $\delta\phi = 1°$, then the error at 400 MeV/c is 102 MeV/c. However, by accurately determining the plane of the plate this error can be reduced to below 40 MeV/c.

In b) one end of the frame is higher than the other. As long as $\delta\phi$ is less than 0.5° the error in p is negligible, and the error in the angle of emission is about $(0.3 \times \delta\phi°)$.

From c) it can be seen that if the plate is inclined

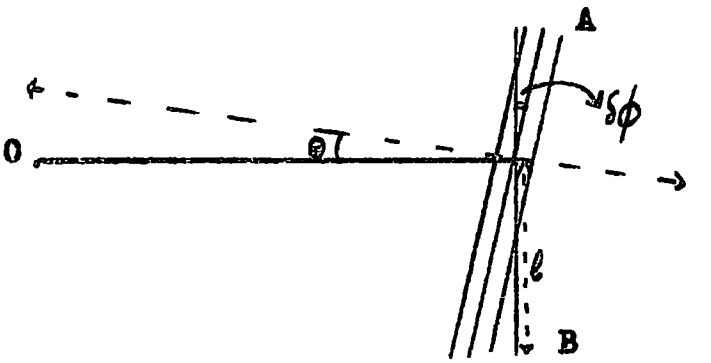

a). Plate inclined in plane of curvature of track.

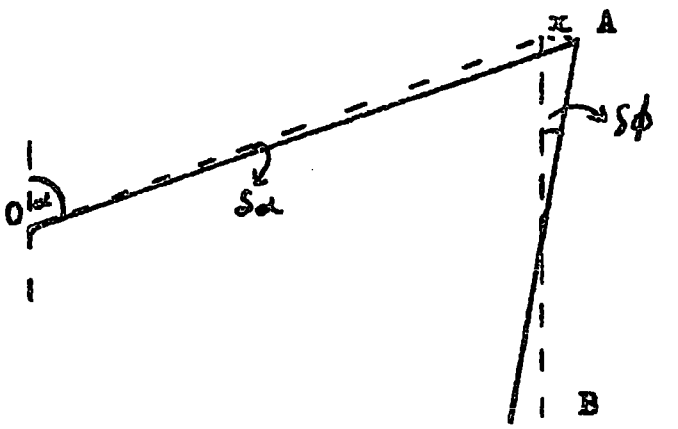

b). Plate not horizontal, one end higher than the other.

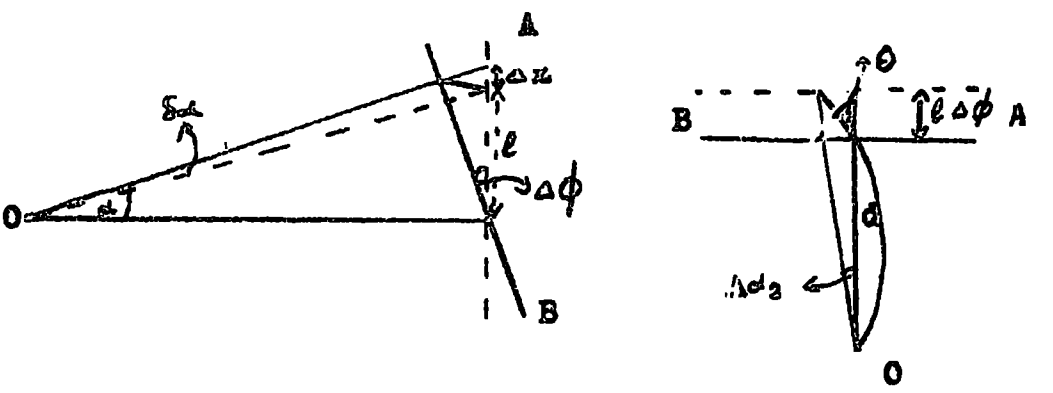

c). Plate inclined towards target in vertical plane.

Figure 7.

towards the target in the vertical plane, then the error in p is of the same order as that introduced by the increased target size. The error in the angle of emission is ($0.3 \times \delta\phi \times \tan\theta$), and is 1°, if θ equals 45° and $\delta\phi$ is 5°.

Obviously when the alignment of the plates was known accurately, corrections could be made to all measurements.

Target Size. All the equations given above assume that the particles are emitted from a known point in the target. For a finite target this is obviously not the case. From Figure 5 it can be easily seen that moving the point of emission from O to some other point O', alters completely the reference system used to obtain the co-ordinates of any track in the emulsion. The length d is altered and also the point D where the perpendicular meets the plate, and hence the curvature of the track cannot be estimated without knowing the point of emission. Similarly the horizontal angle of emission relies on a knowledge of the point of emission. The vertical angle of emission is unchanged and can still be accurately estimated. To cope with this problem of the finite target size, a new method of analysis was introduced

(see chapter 4), and proved successful.

Accuracy of Measurements. The error introduced during measurement of the track angles in the plates was very small. The track could be located to within 3μ under the magnification used, which would introduce a maximum error of 6% for high energy particles, for low energy particles the error is about 1%. On travelling through the glass and the emulsion, the particles will lose energy due to multiple scattering. Because of its greater thickness more scattering takes place in the glass. The errors arising from uncertainty in location and scattering lead to a total maximum error in p of 15%. The maximum error in ϵ is of the order of 2°.

2.3. The Construction of the Spectrograph.

The target for the exposure was to be set on an accurately machined brass base, which could then be used to locate and position the frames carrying the emulsion. The height of the target was determined by the spacing of the magnet faces, (see below) and the final dimensions were 2 x 1 x 5 cm^3, the face presented to the incident beam being 2 x 5 cm^2.

The Frames. In order to reconstruct accurately the particle trajectory, it is necessary to know the position of the track relative to a co-ordinate system in each plate, and also the relationship between the co-ordinate systems of the different plates and the centre of the target. The determination of these relationships is termed 'calibration'. This calibration must be permanent, and to achieve this, the construction must be such that individual plates can be removed from their positions, and replaced without destroying the exact relationship between them, in order to be able to measure accurately the track deflection, and to make it possible to coat, process and examine each plate separately. Since the deflection of the particles is perpendicular to the field, the plates must be supported vertically.

A kinematic method of locating the frames on the supports is employed using a hole, a groove and a plane (Fig. 8). The grooves and holes are cut in appropriate positions on the upper surface of brass pillars, placed behind the edges of the frame to eliminate as much back scattering into the plates as possible. The complementary

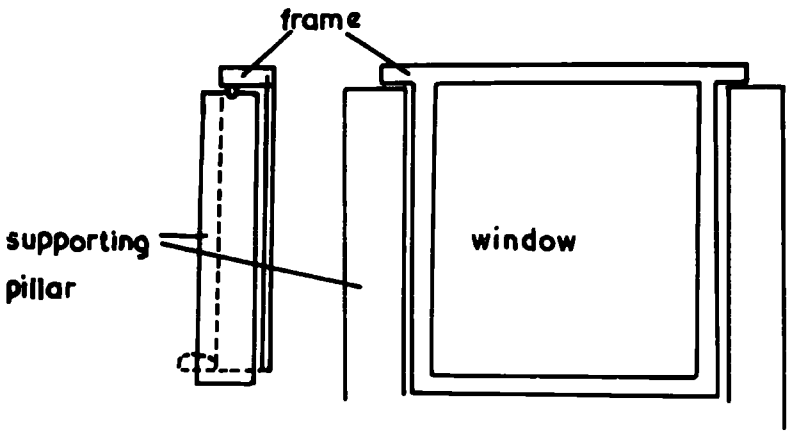

a) sectional drawing showing frame on supporting pillars

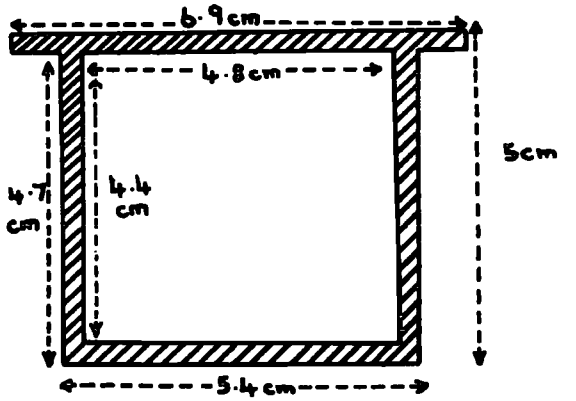

b) front of frame

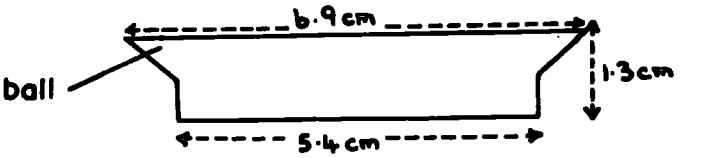

c) top of frame

Figure 8.

members of the location on the frames are steel balls 2 mm in diameter attached one at each end to the underside of the supporting extension. The balls are attached in a position slightly removed from the axial plane of the frame, so that under its own weight the frame rests with its lower end against a projection; this constitutes the third member of the location. This method of accurate location has already been used successfully in this laboratory (Allen and Apostalakis, 1961). Great care is taken to ensure that the frames are perpendicular to the brass base when resting in position on the supports. Ideally, the kinematic location should be solely under a gravity constraint but, to avoid the possibility of movement of the plates while being inserted between the magnet poles, they are clamped by exerting pressure against a small ball on their upper surfaces. Just sufficient pressure is exerted to prevent movement; no deformation of the system is introduced thereby. Even with this additional constraint, the position of each frame is reproducible to better than 1μ.

In all three sets of six frames were accurately

machined for two exposures and a dummy run, plus an additional two spare frames. The detecting circle comprises two semi-circles of three frames each around the target.

The glasses were affixed to the front of the frames by gluing round the edges of the glass, and holding the glass permanently against the frame with a metal clamp screwed to the side of the frame.

The Plates. Each plate consisted of a specially coated glass about 800μ thick, with an emulsion 100μ thick, stuck onto both surfaces. The thickness of the glass being accurately determined for each plate. The basis of the co-ordinate system is a grid of fine lines ruled on one surface of the glass of each plate. For the greatest usefulness of the spectrograph the accuracy of the calibration should be of the order of 1μ.

By means of an engraving diamond a reference grid was inscribed on the glass surface nearest the target, and the calibration carried out with the frames in position. The grid is a single line across the plate horizontally, with three lines perpendicular to it at intervals of about 1.5 cm, the intervals being known

exactly for each frame, and the lines being perpendicular to within 5'. The distances of the crossing-points on the grid from the target centre were measured accurately using travelling microscopes, with each frame in its correct position. The frames and their positions are correspondingly numbered, to ensure correct replacement. From these measurements d, and the point D, where this perpendicular meets the plate relative to the grid can be ascertained.

Once the emulsion had been affixed to the glass, they were covered with black paper to shield them from all light.

Calibration. As has been shown each plate now has a fixed position relative to the target centre. d is known, and its distance from any recognisable point, C, on the grid in the same horizontal plane (see Fig. 5b). When scanning the plates the co-ordinates of C were recorded, and the co-ordinates of each track can be obtained using C as the origin. If the co-ordinates of a track at Z, are (x', y') with respect to C, then -

$$x = x' + \delta \qquad 2.3.1.$$

and hence ρ in 2.2.2 can be found.

2.4. The Magnetic Field.

A field strength of the order of 20 kilogauss was required over the target and frames, in order to facilitate observation of the required tracks. At this field strength, even a 300 MeV pion would undergo an easily detectable deflection ($> 1°$) over a distance of 6 cm. Also low energy particles would suffer large deflections. For example, the protons emitted from the target would have a much lower momentum than the pions, and many of them would thus move in tight spirals, never reaching the plates, and therefore not adding to the background.

To achieve this high field over the detectors a pair of metal cones was attached to the magnetic poles. The cone faces were held at a fixed distance of 5.5 cm apart by three metal spacers bolted on (see Fig. 9). The face area of the cones was the detecting circle of the spectrograph. With this arrangement a high uniform field was produced, and it was still possible to slide the

Figure 9.

The spectrograph in place between the cones.

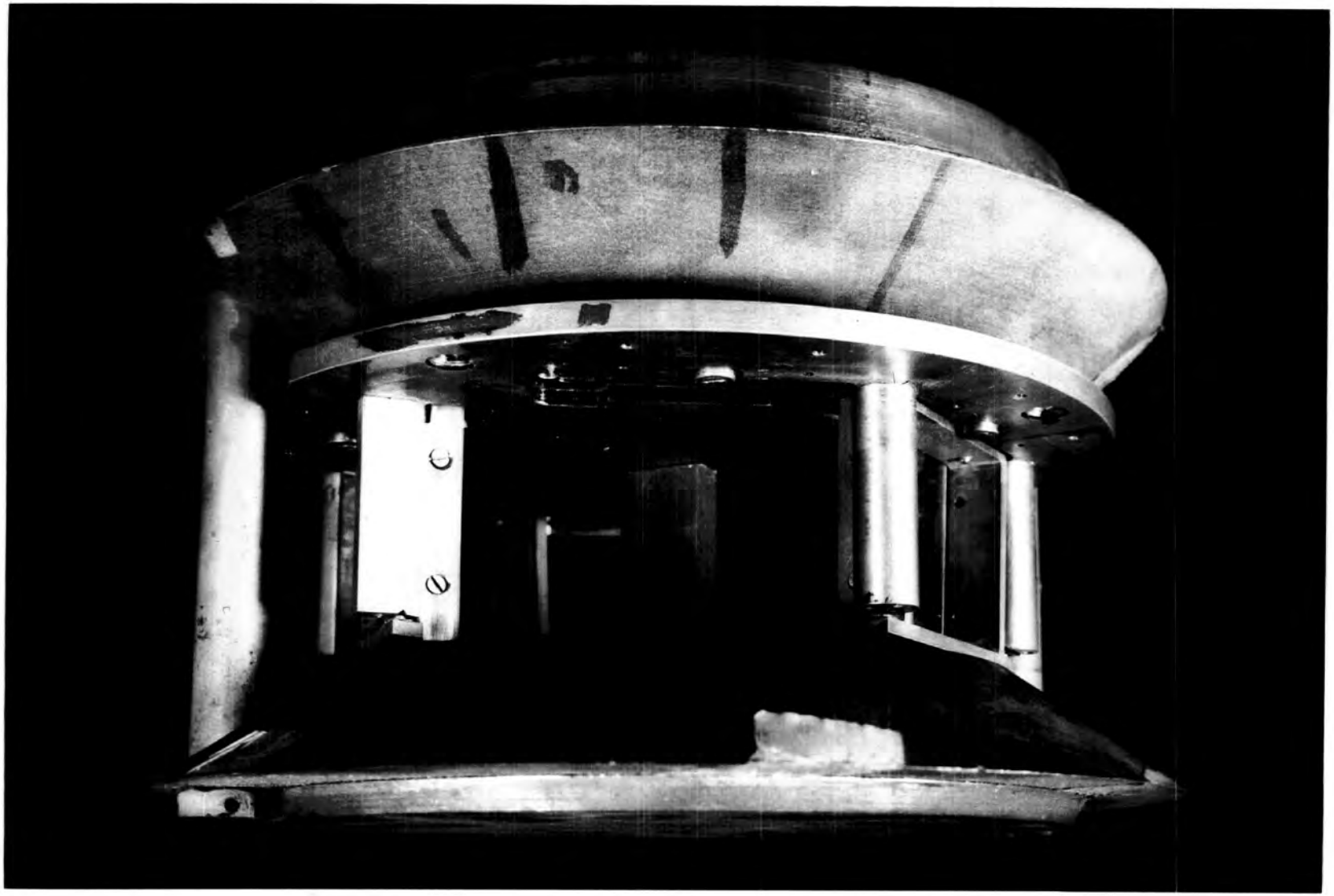

spectrograph in and out easily in order to replace target and frames.

The base of the spectrograph was so shaped that it could be slid easily into position between the spacers, and returned to its former position (see Fig. 10).

2.5. The Spectrograph as adapted to Experimental Conditions.

Experimental Adaption. It was decided to make two exposures with different targets. For one target carbon was chosen, as work with proton beams had previously stressed the need to examine closed shell nuclei (see 1.3), and many experiments had been carried out using a carbon target. The other target was to be silver, an important constituent of photographic emulsion and a heavier nucleus than carbon.

The original spectrograph (as described in 2.3) consisted of two semi-circles of three frames each; six frames in all. Each frame subtended an angle of 40° at the target, and allowing for track curvature, all angles of emission except those in the extreme forward and backward directions were covered. The exit and entrance were 2.4 cm. The magnetic field applied, caused the beam

Figure 10.

Insertion of the spectrograph between the cones.

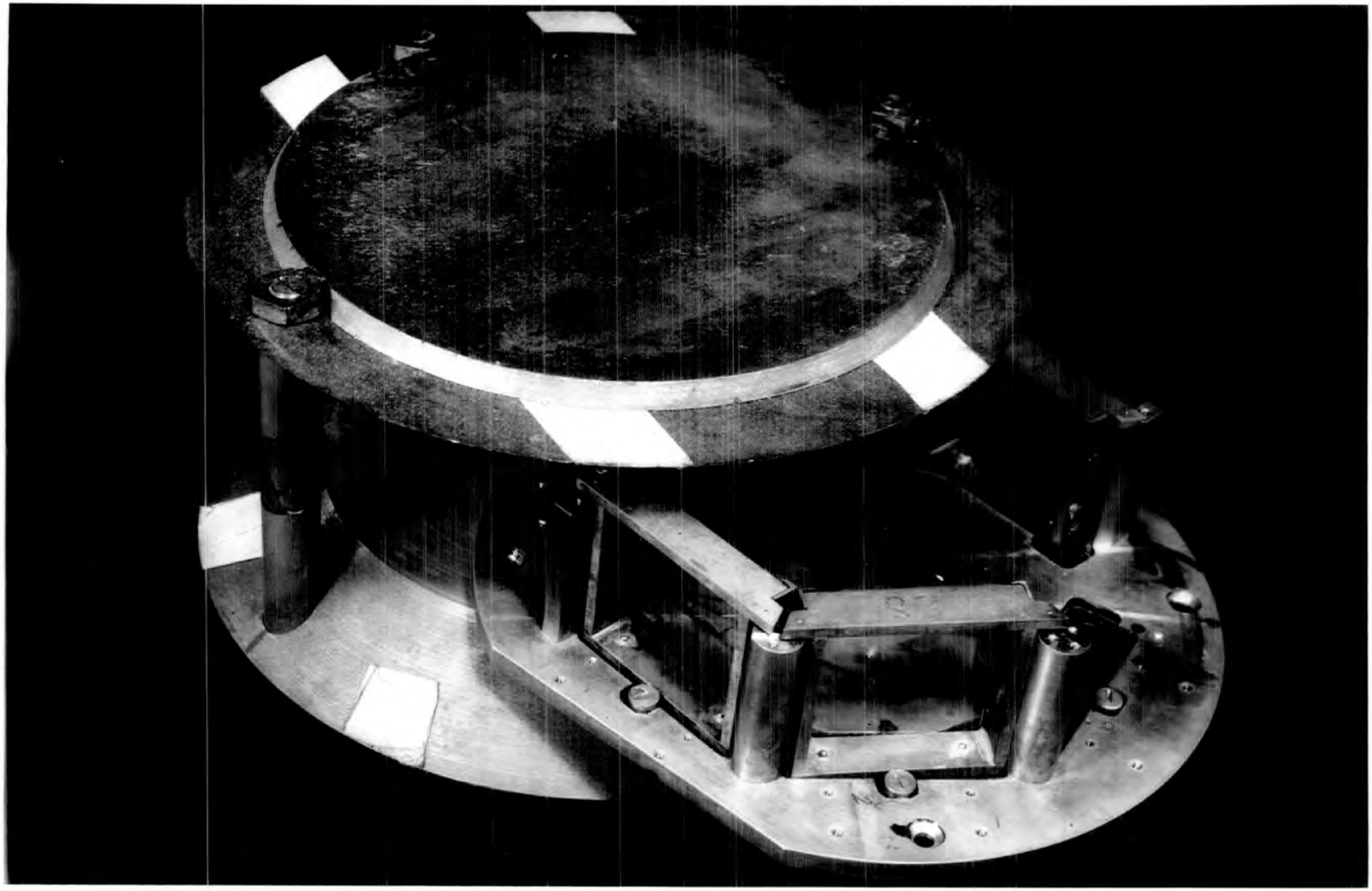

to deflect by 5 mm within the spectrograph before reaching the target. In order to focus the most intense section of the beam on the target, the target was moved 5 mm from its central position. This was necessary since the calculated number of secondaries observable depended on the centre of the beam passing into the target and being scattered. The repositioning did not alter the essential measurements to be made for each track, since the system could easily be recalibrated, and after the exposures had been made, the recalibration was performed for each of the frames, with the target in the new position.

The second modification which was made, was more important. Due to difficulties in focussing the beam (see chapter 3), its final profile laterally extended beyond the spectrograph aperture, so that a portion of low, but by no means negligible intensity passed through the pillars and plates on either side of the entrance and exit. This meant that two plates at least would have too high a background to be of any use, for not only would there be tracks directly made by the beam, but also scattering and interactions in the pillars would fill the

two nearest plates with tracks and increase the background in the others. Lead shielding and collimators did not remove this tail on the profile. It was decided therefore, to remove two of the frames, so that the spectrograph entrance and exit for the beam were increased, and the chance of scattering in the supports was considerably reduced. The frames removed were those in positions 6 and 3 in Figure 4. The whole system was then rotated until the beam was once more incident perpendicularly on the target.

The removal of these frames meant that a much smaller range of emission angles was covered, and also that the detected particles were all scattered approximately perpendicularly to the incident beam. Unfortunately this is the least sensitive region in all the nuclear models for which computations had been performed. The forward direction is the most sensitive region, and the region in which the greatest discrepancy had been observed so far in all experiments. The cross-section for scattering around 90° is almost constant, but the shape of the energy spectrum in this region

differentiates between the various models. Probably the most sensitive variable in this region is the average energy of the particles scattered into each angular interval. However, it was necessary to alter the spectrograph to make the exposures in the time available.

These modifications did not in any way alter the essential accuracy of the spectrograph. In the angular region covered it was still possible to calculate both p and $\mathcal{E}$ from simple recordings of the tracks co-ordinates relative to the grid. A dummy run without any target would be made to record the background. This run would also reveal, if the beam at any time passed through any of the remaining plates.

The spectrograph as used with four frames in position and a carbon target can be seen in the photograph Figure 11. The glasses without emulsion are affixed to the frames, but the frames are unclamped. The shaping of the base which locates it between the magnet spacers is shown. The beam enters from the right, and was deflected by the field towards the top of the photograph and back again, on traversing the spectrograph.

Figure 11.

The spectrograph.

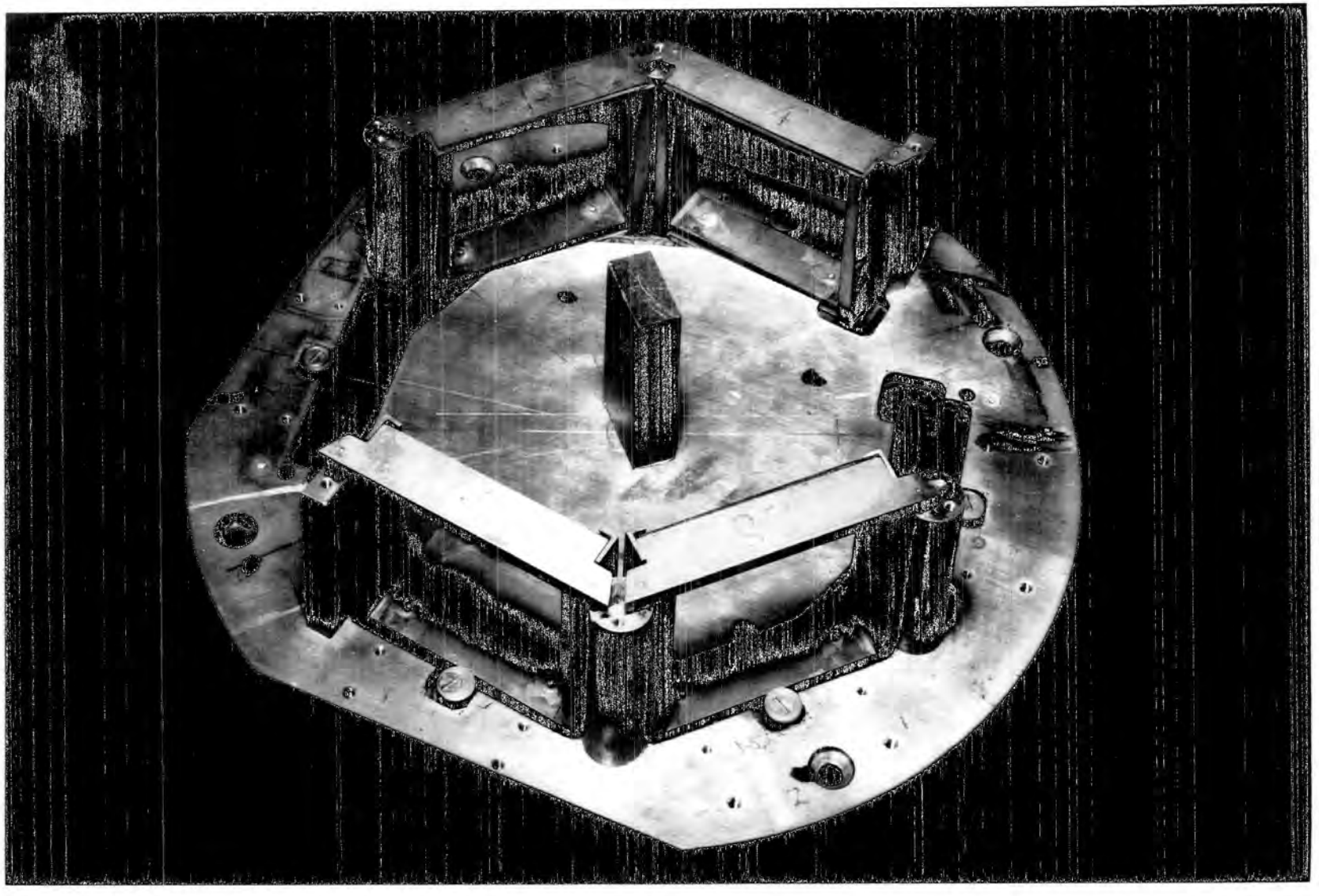

Correction Factors. It was necessary to adjust all computed values for two factors which affected the experimental data. The first was for the solid angle subtended by the plate at the centre of the target. Using diagram 3b the solid angle can be calculated. The horizontal path length for a particle is the arc of the circle cut-off by the chord ρ, $2\phi R$. In three dimensions the path length is -

$$\frac{2\phi R}{\cos\varepsilon'} = \frac{\rho\phi}{\sin\phi}\cdot\frac{1}{\cos\varepsilon'} \qquad 2.6.1$$

The angle the beam makes with the perpendicular to the plate is α and -

$$\cos\alpha = \cos\theta.\cos\varepsilon' \qquad 2.6.2$$

also $$\rho = d/\cos(\phi - \theta)$$

let $$\psi = \phi - \theta$$

The solid angle per unit area is dw, where

$$dw = \frac{\cos\alpha}{(\text{path length})^2} \qquad 2.6.3$$

Thus from 2.6.1, 2.6.2 and 2.6.3

$$dw = \frac{\cos(\phi - \psi).\cos^2\psi.\sin^2\phi.\cos^3\varepsilon'.}{\phi^2.d^2} \qquad 2.6.4$$

so that for a particular ε and p, ρ and ϕ are found for each ε, and dw can be calculated, using the relation -

$$\sin(2\phi - (A - \varepsilon)) = \frac{300Hd}{p} - \sin(A - \varepsilon) \qquad 2.6.5$$

and 2.6.4. This solid angle varied only slightly over the area scanned; the maximum variation being 6% for particles all travelling in the same plane, and 20% for all particles travelling from the target to any one plate.

The second factor was due to the selective detection at the edges of the plates. Particles emitted at the same spatial angle can have different projected horizontal angles of emission, and hence one may be detected while another misses the edge of the plate (see Fig. 6). Also it is the projection horizontally which determines the radius of curvature of the track. Hence at the plate end A for particles emitted with a vertical component of momentum more low energy particles will be lost than high energy ones. Similarly at the end B more high energy

particles will be lost. As considered here this effect is due to the finite size of the detecting area, the plates, and the curvature variation with momentum, and is independent of the target size. The effect of the target size was considered separately. The method of analysis described in chapter 4 took into account the loss due to the finite detector and shape.

Accuracy. The grid was calibrated to within 1 micron. The accuracy of location of the frames (see 2.2) was such, that with the frames in position the grid line was horizontal to within 10μ, the actual slope being known for each frame. This meant that the induced error in p and ε was negligible.

The plates were vertical to within 3μ, and have only been scanned across the central region, thus no corrections have been introduced to compensate for this very slight inclination with respect to the vertical.

Effect of the target. The chance of an incident pion making two collisions in the target is 1/400. Scattering in the target gives rise to an error in ε of less than 5°, and only below 160 MeV/c does it have an

appreciable effect on the momentum. For a particle of 120 MeV/c passing through 1 cm of target, the expected decrease in momentum is 10 MeV/c for carbon, and 19 MeV/c for silver. Therefore at a momentum as low as 120 MeV/c the error is 16%, and above 200 MeV/c it is negligible. The target size introduces errors in ρ and $\mathcal{E}$ which are considered further in chapter 4.

Effect of field. The high magnetic field causes low momentum particles to spiral, so that they never reach the frames. With 25 kg the lowest momentum which could be detected is about 50 MeV/c, which would give a very black track for a pion with θ equal to about 180°. In addition the target size would effectively prevent the detection of any particles below 80 MeV/c for carbon, and below 90 MeV/c for silver, due to absorption of secondaries within the target.

The effect of these errors is summed in Table 13 (see chapter 4) for plate 5, as an example of the variation in expected error in any one plate.

3. THE EXPERIMENTAL RUN.

3.1. Production of Pion Beam.

The beam used was produced from an internal target in the 600MeV C.E.R.N. synchrocyclotron. A similar beam had already been produced once, so the essential details of the transport system were already known. The requirement was a negative pion beam of about 300MeV with as high an intensity as could be achieved. It was necessary before the exposure to measure both the energy and the contamination of this beam, and to focus it onto the target. The actual floor space available for setting up the transport system was limited by the need to avoid the muon channel on one side, and the neutron beam on the other (see Fig. 12). In fact the geography of the neutron room where the exposures were made, determined the location of the target relative to the channel through the synchrocyclotron shielding wall.

It was hoped to finally produce a beam which in a reasonable exposure time would provide one track per field of view when scanning the plates. This meant in fact about 5×10^3 secondaries per cm^2. For this was required a beam of intensity 4×10^4 particles per second, which could be focussed sharply on to an area of 2×5 cm^2.

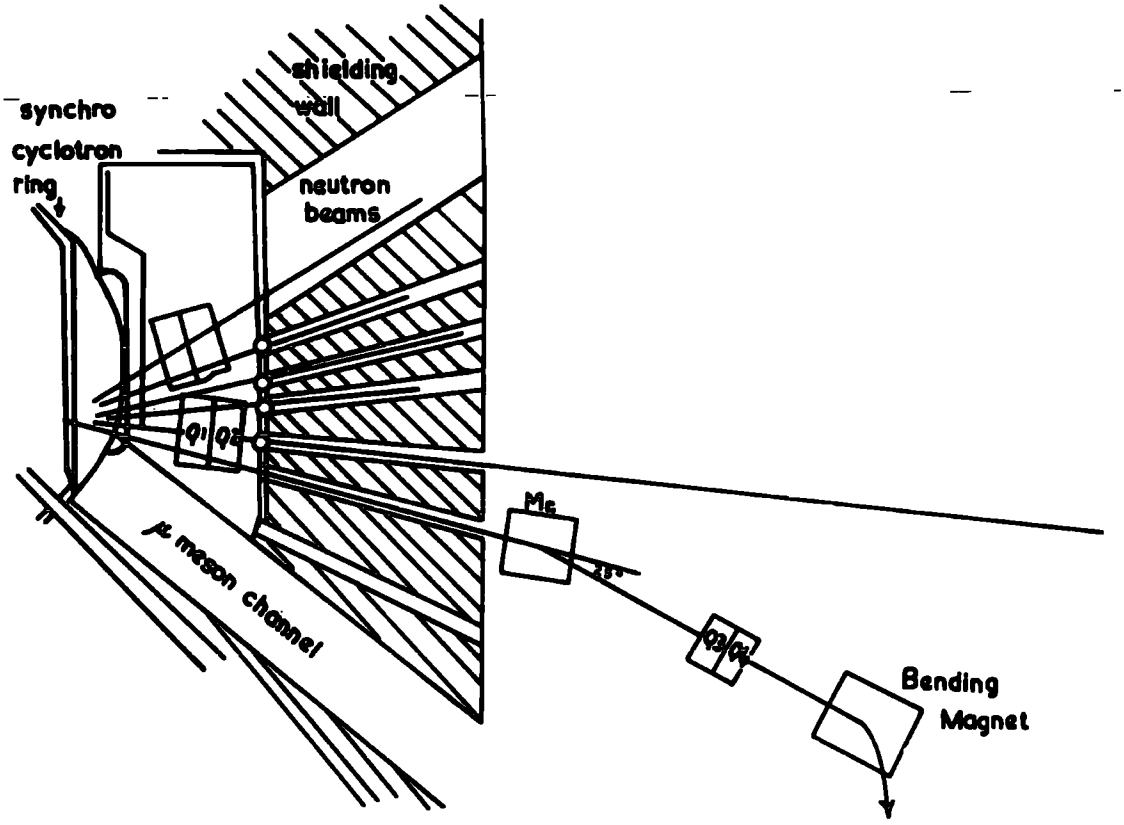

Diagram of Neutron Room
showing experimental layout

Figure 12

The exposure time would then be about eight hours. (see 2.1).

3.2 Beam Transport System.

The beam transport system consisted of the fringing field of the synchrocyclotron, and then a pair of quadrupole magnets, placed as near to the target as possible in order to obtain a high beam intensity. These magnets are marked Q1, Q2, in Figure 12. Outside the shielding wall was an analysing magnet, MC, and a further two quadrupoles, Q3, Q4, which independently focus the beam horizontally and vertically. The final component of the system was the magnet into which the spectrograph was to be inserted, hereafter referred to as the 'bending magnet'.

The magnet used for the bending magnet was a C.E.R.N. one metre bending magnet with tapered poles, which would produce a maximum field of 17.5 kilogauss (see CPS User's Handbook 02, page 2). With the cones in position near the front (with reference to the beam source) of the magnet, the magnetic field strength was measured using both a fluxmeter and a gaussmeter. The

two instruments gave equal readings within the experimental errors for the field strength, which was 25.5 kilogauss between the cones during the exposure. In order to be able to define the trajectory of the beam between the point of entry into the magnetic field and the target, it was necessary to plot the field strength over the area of the bending magnet. A typical plot of the field variation is shown in Figure 13.

In order to define the trajectory in the exposure area, use was made of the floating wire technique (see Braunersreuther, 1961). A wire carrying an electric current, had one end fixed on the axis of the beam between the analysing magnet and the second pair of quadrupoles. This wire passed through the quadrupoles and through the bending magnet between the cones, and was held taut on the far side. The correct deflection for a given beam momentum should be obtained by passing the appropriate current through the wire. The wire itself, must not pass through two focal points, since all trajectories will go through these two points and the wire therefore becomes unstable. The field strength changed so rapidly over the cones that the wire merely averaged the effect, and

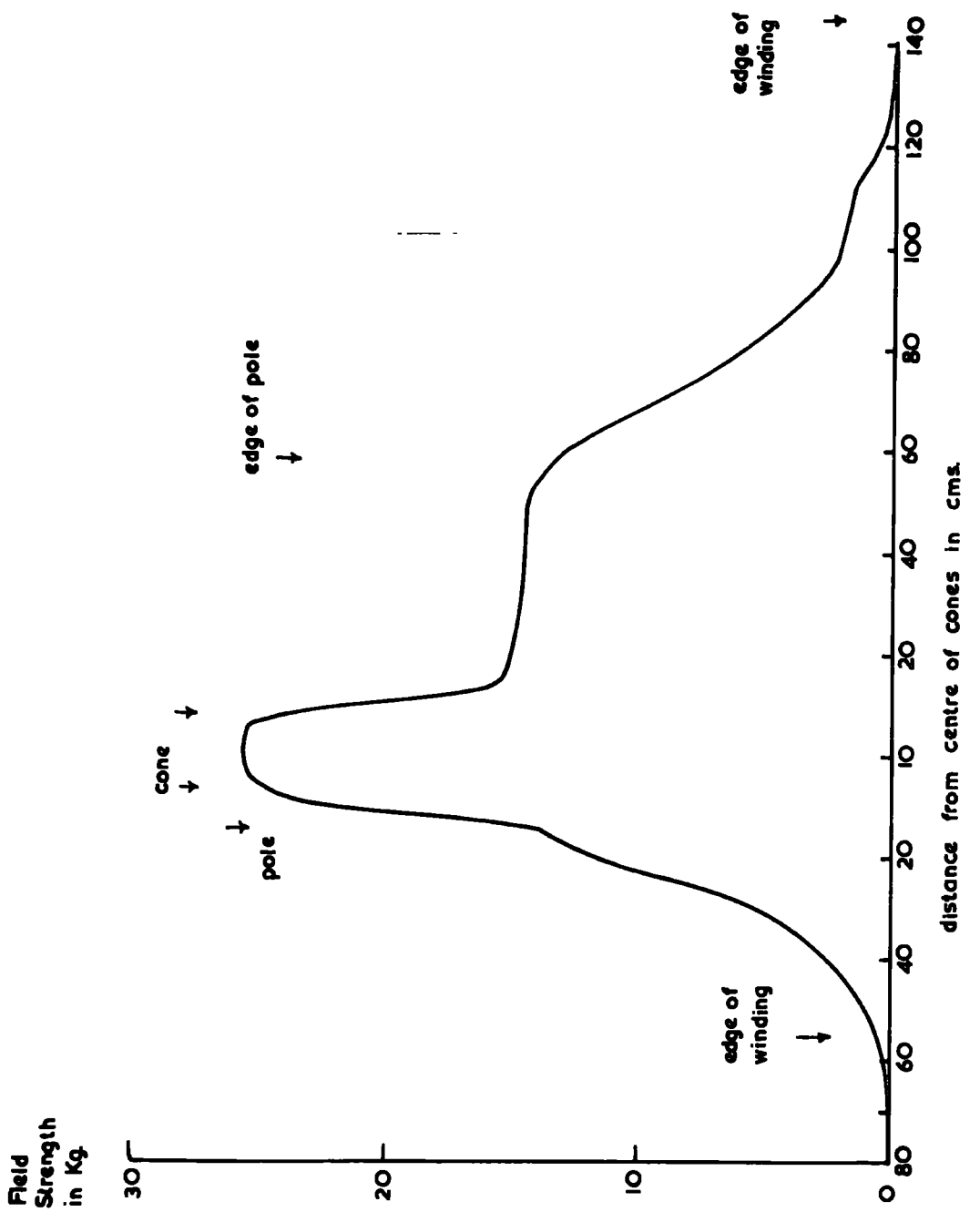
Magnetic Field Strength Variation across magnet
Field Strength in Kg
30
20
10
0
80
60
40
20
0
10
20
40
60
80
100
120
140
distance from centre of cones in cms.
edge of winding
edge of pole
cone
pole
edge of winding

Figure 13

only a rough estimate of the deflection and hence the trajectory could be estimated. However, the wire indicated that the unscattered beam would pass out through the side of the magnet, no matter which position the cones were placed in relative to the geometry of the bending magnet.

The Profile. The profile of the beam was examined with the aid of a beam scanner consisting of scintillation counters. The intensity of the beam was first optimised by varying the currents in the quadrupoles and the analysing magnet. Three counters were used. Counter 2, the monitor, was between the channel through the shielding wall and the quadrupoles Q3, Q4. Counters 3 and 4 were placed on a scanning table, beyond these quadrupoles, one directly behind the other. The table provides the means for these two counters to be moved by remote control vertically and horizontally, accurately and together, through the beam.

For optimisation the currents in each component were varied individually keeping everything else constant. When altering the currents in a pair of quadrupoles, one current was increased, as the other was decreased, and then the polarity of each was reversed. As each

quadrupole tends to focus the beam in one plane and defocus it in the perpendicular plane, this selected the best combination for focussing the beam at one unique point in both planes. The beam profile was almost guassian, both horizontally and vertically. The peak of the intensity curve at the focal point, about one metre from Q4, was made as sharp as possible by altering the magnet currents, but there was still a long, low intensity tail.

A collimator was erected beyond the second pair of quadrupoles Q3, Q4. This reduced the peak of the intensity distribution rather than the tail. The intensity was measured at the image and at various distances from it. Finally a long collimator was built with an exit pupil 1 x 4cm^2, which gave a half width for the distribution of 1cm. This still left the beam too diffuse to reach the target without the tail passing through the side of the front frames. Two of the frames, those in positions 3 and 6, were removed in order to widen the entrance and exit, and the cones were rotated slightly. The final profile is shown in Figure 14.

a) Horizontal Beam Profile collimator exit pupil 1x4 cm^2

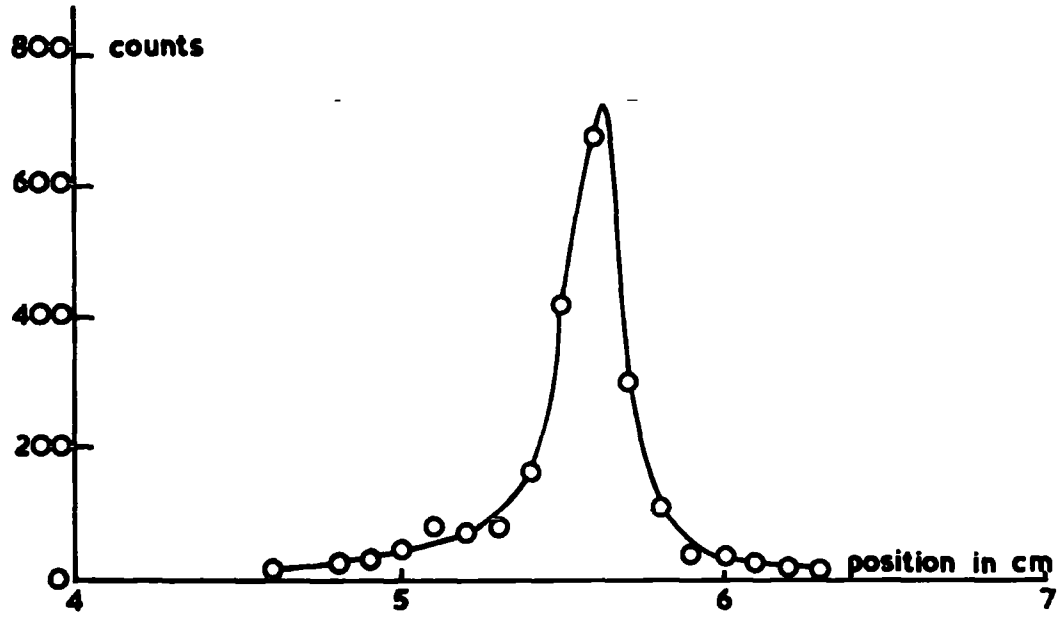

b) Vertical beam profile

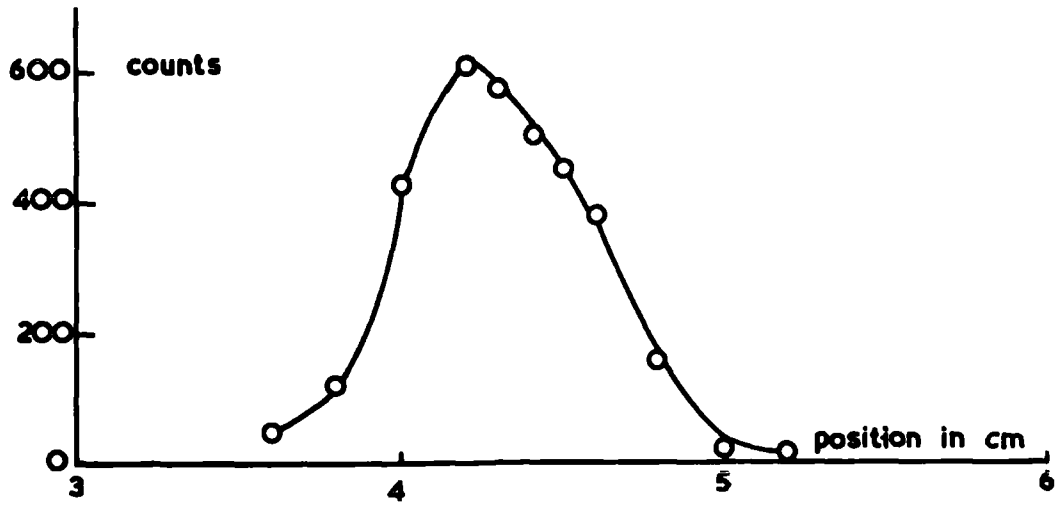

Figure 14

In order to find the correct position for the target inside the bending magnet, use was made of a scintillation counter with a long light guide. The counter could be placed between the cones, and the system adjusted so that the target was in the optimum position.

The beam intensity was also monitored using a scintillation intensifying polaroid camera made by one of the C.E.R.N. staff. (M. Roberts, private communication). This produced photographs of the beam intensity distribution, but the pion flux was so low that a long exposure was needed.

With the scintillation counter in the target position, the cones were moved across the magnet face until the counter was in the beam. The final adjustment was then made by varying the magnet current until the beam centre impinged perpendicularly on the counter. Once the cones were in their final position, this position was marked on the lower magnet face and the cones were not moved throughout the exposures. The spectrograph was inserted and removed without upsetting this arrangement. The magnetic field used for the exposures was 25.5 kilogauss.

3.3. Contamination and Radioactive Background.

Contamination. An attempt was made to measure the contamination of the beam using a time of flight technique. (Dick, private communication). Two scintillators are used, both placed in the beam, but a distance, L, apart. The final output of the equipment has a series of peaks, one for each type of particle present in the beam. The separation between two of these final peaks is given by:-

$$\Delta T = L(1/\beta_1 - 1/\beta_2)/c$$

where ΔT is the time interval between the peaks, and β_1 and β_2 are the momentum-energy ratios for the two different particles.

The distance L was 10.53 metres. The resolution of the peaks was not accurate enough with the counter separation available, so that all that could be concluded was, that there was a low muon but possibly high electron contamination. A typical curve obtained by this method is shown in Figure 15. By observing the shift of the peak when a known delay was applied between the counters, the distance between the channels could be calibrated in terms of the time interval ΔT.

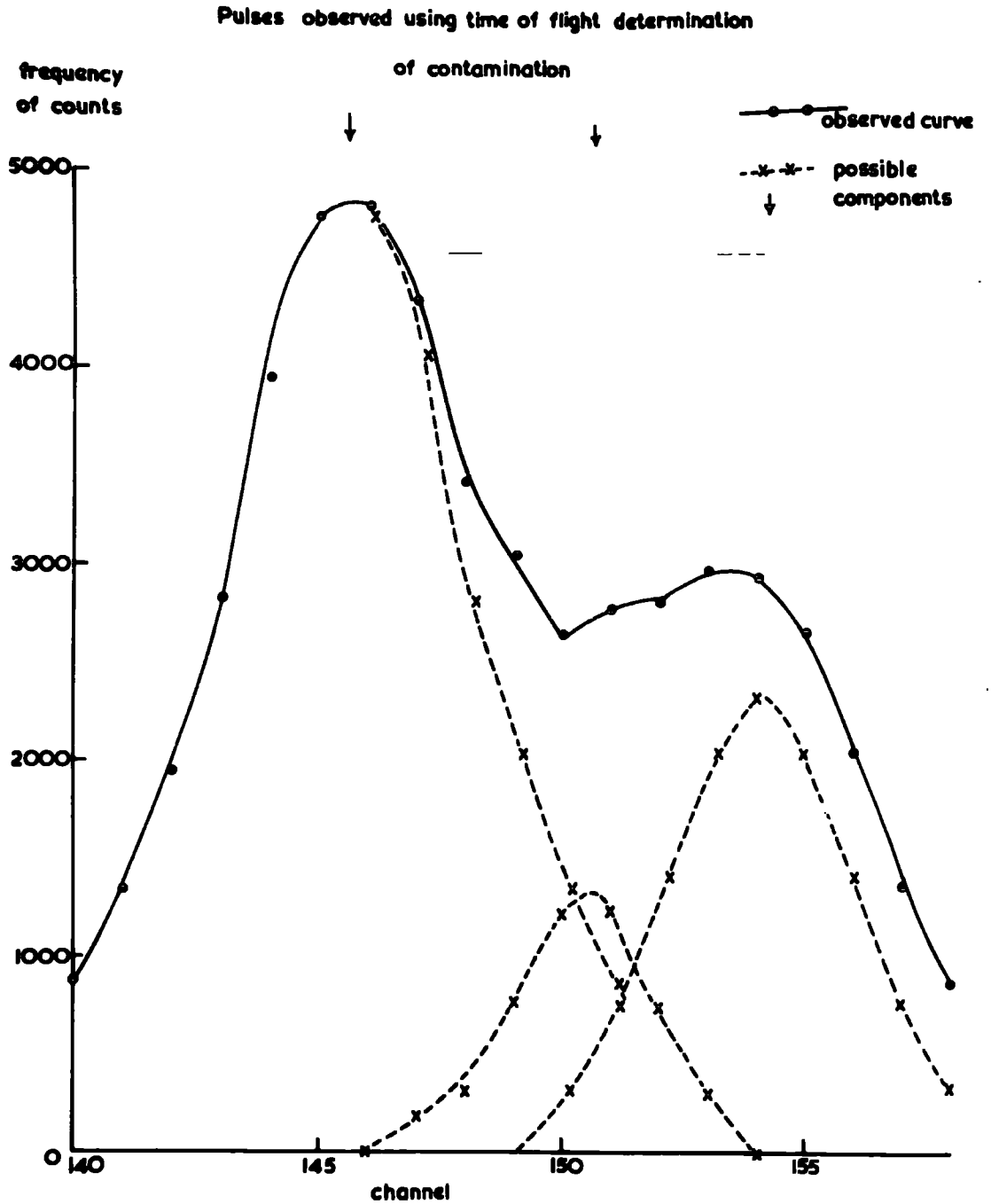
Pulses observed using time of flight determination
of contamination
frequency
of counts
observed curve
possible
components
5000
4000
3000
2000
1000
0
140
145
150
155
channel

Figure 15

The muon contamination was examined by exposing some plates for ten seconds directly to the incident beam. The plates were then rotated through 90° and exposed for one minute to the beam, after the beam had passed through 15 cm of copper. The collimator used during the exposures was in position and the stack was exposed beyond it. The range of the particles in these plates was examined and the appropriate particle masses determined. This method showed the muon contamination to be 10%.

Background. In order to reduce the background a lead wall was erected in front of the cones, with a suitable beam aperture. This would shield the plates from background originating outside the magnet, but could not reduce any background arising after the beam had entered the spectrograph. Since as already mentioned in 3.2, the beam passed out through the side of the magnet some background was inevitable. The dummy run would provide the necessary data for the subtraction of the background from the signal.

Finally the best possible arrangement in the time available was achieved.

3.4. Exposures Made.

Three four hour exposures were completed with the spectrograph and with plates in positions 1, 2, 4 and 5; (see Fig. 4) for one a silver target was used, for one a carbon target, and one was without a target. For each exposure four fresh plates were used.

Because of the high background and the broad profile of the beam, it was decided to make an alternative exposure with no magnetic field. The simplest arrangement was used, employing large solid angles, and is shown in Figure 16. Rejecting the use of a magnetic field meant that multiple scattering measurements would have to be made in order to obtain the secondary pion energies, and therefore the layout was designed with this in mind. Since the technique used is not uncommon in nuclear physics and cosmic ray work, this will be referred to as the 'conventional' exposure.

The use of iron shielding successfully limited the extent of the beam in the vertical plane, so that it was incident on a 10cm long carbon target, but not on the stack of nuclear emulsion pellicles. In the horizontal

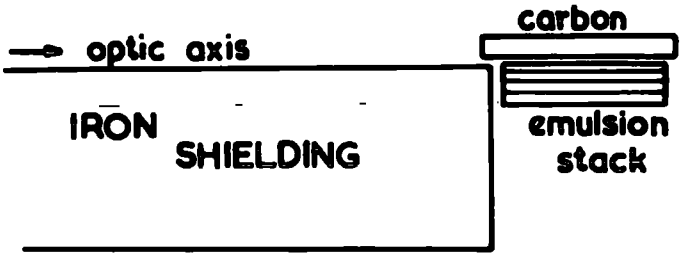

a) Arrangement for exposure

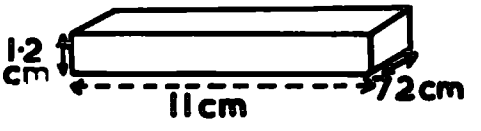

dimensions
of carbon block

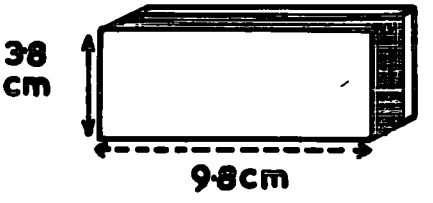

emulsion stack

Figure 16

plane the beam profile was satisfactory. The stack consisted of 25, 400μ thick pellicles, lying between two thick pieces of perspex, and the whole covered with black paper to shield the emulsion from the light. This stack was supported at a distance of 1cm from the carbon, so that low energy particles would not reach it. The exposure lasted three hours. Secondaries emitted between 6° and 174° could be recorded in the stack, but the angular interval between 35° and 145° is the most completely covered.

The disadvantages incurred by this design were those which had led in the first place to the design of the spectrograph. Aligning the plate for each angle of emission, finding and measuring the tracks was a slow and tedious process. Also, though for most tracks the pion mass could be fairly confidently assumed there was no way of determining the charge of the particle.

Momentum Determination. The exposure already mentioned in 3.3. would enable the momentum of the beam to be determined within the accuracy needed. The particles which had passed through 15cm of copper would

have lost on average all but a few MeV of their initial energy. Therefore the particles will come to rest in the emulsion and from the length of the track in the emulsion the initial energy of the particle can be estimated. The tracks running perpendicular to these stopping particles were of unscattered particles from the main beam, and on these tracks pβ measurements could be made. Thus two methods were available for determining the momentum of the beam, and the values obtained could be compared.

3.5. Processing.

Development of all the emulsions was by a temperature cycle method. The plates were presoaked and cold developed at 6°C, and then placed in a dry hot stage at 23°C. The duration of each stage depended on the emulsion thickness. This system produced even development throughout the emulsion with a clear image.

Before development the emulsions from both the conventional exposure and the momentum-contamination exposure were gridded on one surface, and numbered and

labelled on the other surface using a soft pencil. The pencil mark would show after processing since all pressure marks cause local development. The emulsion gridded side down and then affixed to a glass plate which had been specially coated by Messrs Ilford Ltd.

The spectrograph plates were removed from the frames before processing. Since these plates were so small a special developing tank was constructed. The plates, approximately 5.4 x 5cm^2, were held in a perspex rack. As there was emulsion on both sides of the glass, the rack was necessary to prevent the sodden emulsion being damaged by handling during the processing. This rack fitted comfortably into the developing tank which could then be supported in a tank of water at a suitable temperature. Before removing from the frame, each plate was marked on the surface nearest the target so that both its position on the circle, and the type of target, if any, were recorded. The spectrograph plates were processed immediately after exposure.

4. SCANNING AND MEASURING THE PLATES AND REDUCTION OF DATA

In chapter 3 three kinds of exposure have been described. Firstly exposures to determine the mean momentum of the beam were made. Secondly there were exposures using the emulsion spectrograph, and thirdly exposures to determine the scattering in carbon using emulsion in a conventional way. In this chapter the evaluation of the momentum of the beam based on scattering measurements and range-scattering measurements is described. This is followed by an account of the scanning and analysis of the plates and the results of the spectrographic exposures. The results from these exposures are compared with those from the conventional emulsion stack exposure.

4.1. Determination of the Energy of the Beam.

The experimental arrangement and exposures for determining the incident beam energy have already been described in 3.3. It was arranged that the kinetic energy would be in the region of 300 MeV (see 1.7), and the apparatus was designed with this energy in mind. In order to be able to estimate the energy loss of the

scattered pions, it was necessary to know as accurately as possible the average energy of the incident particles, and their energy distribution. Without these values the determination of the number of low energy transfers which take place would not be possible. Two methods were used to measure the beam energy.

a) Absorption of the beam. The stack which had been exposed behind the copper absorber was scanned as follows. Tracks, which from their inclination and position must have passed through the copper were picked up 1 centimetre from the edge of the plate. Each track was aligned parallel to the motion of the microscope stage, and its length and angle of inclination recorded. Using a cell length of 200μ, the scattering of the track was measured, moving away from the plate edge, and hence $p\beta$ for each track was determined. About 50 readings were made for each track.

Nineteen tracks were measured thus, and three of these were rejected after measurement since their $p\beta$ were too high for them to belong to a 300 MeV π^- beam, but were consistent with them being muons. For the remaining sixteen tracks, the average $p\beta$ was (122 $\pm$ 3) MeV/c with

a standard deviation of 15 MeV, corresponding to a kinetic energy of 62 MeV after 15 cm of copper. The range-energy determinations of Barkas (1958) were used in conjunction with the data of Sternheimer (1959) to evaluate the initial energy incident on the copper. From the measurement of $p\beta$ the energy and therefore the residual range of the particle leaving the copper can be deduced. This residual range added to the equivalent path in emulsion for 15 cm of copper gives the total range and hence the energy.

The incident kinetic energy was calculated by the above method to be (285 ± 2) MeV.

b) Measurements on the incident beam. Scattering measurements for determining $p\beta$ were made as follows. Beam tracks were picked up 1 cm from the plate edge, aligned parallel to the traverse of the stage, and the scattering recorded on cell lengths of 200 or 300μ. Over 40 readings were made on each track, so that $p\beta$ was determined to 10% accuracy.

31 tracks had an average $p\beta$ of (376 ± 12) MeV/c, which is equivalent to a kinetic energy of (285 ± 15) MeV.

c) Final estimate of energy. Good agreement for the energy of the incident meson beam was obtained using the two methods described above. The value used in all subsequent calculations for the incident kinetic energy was (285 ± 15) MeV, equivalent to a total energy of 421 MeV and a momentum of 400 MeV/c.

4.2. Scanning of the Plates from the Spectrograph Exposure.

a) Details of the method. The plates were examined on Cooke microscopes under a magnification of 45 x 1.5 x 15.

The upper emulsion surface, that which had been nearer the target during the exposure, was area scanned. Suitable tracks were picked up and followed to the emulsion-glass interface, and were paired in the other emulsion, matching similar lengths and the same apparent directions at the emulsion-air interface; the direction at this surface is not affected by distortion because the emulsion can move freely here (Fig. 17a). The co-ordinates (X, Y) of the track at the two emulsion-glass interfaces were recorded, and at the beginning of each days scanning

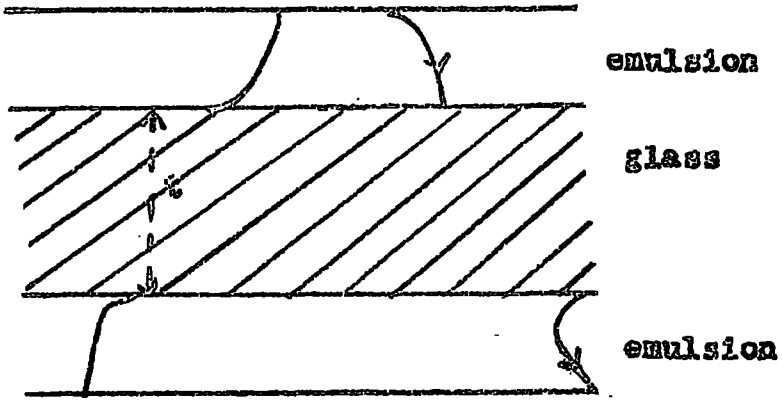

a). Track directions in emulsions and glass.

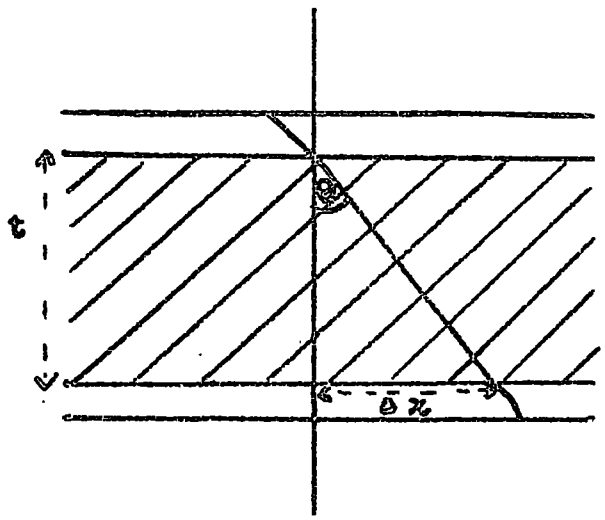

b). Determination of θ.

Figure 17.

the co-ordinates of the central crossing-point of the grid-lines on the glass were also recorded all to an accuracy of $\pm 2\mu$.

Equal areas either side of the central grid line were scanned, each scan starting and finishing at least $\frac{1}{2}$ cm from the edge of the emulsion thus eliminating edge distortion. The scanning was started above the horizontal cross grid line, and that section of the plate which had been the upper area vertically during the exposure was scanned.

To eliminate obvious low energy and background particles, tracks whose length was greater than 250μ in the upper emulsion were rejected. Even if a particle were emitted from the extremes of the target, its track length should be less than 250μ in the upper emulsion, and most low energy secondaries will have been absorbed by the target (i.e. those with momentum $\leq$ 80 MeV/c, see 2.5). Thus any long tracks should be background or secondary scatters.

b) Collection of data.

Horizontal component. From the co-ordinates of

the track at the emulsion-glass interfaces, the horizontal component of the track length, Δx, in the glass was obtained by subtraction (see 17b). Now

$$\tan\theta = \Delta x/t. \qquad 4.2.1$$

where t is the glass thickness (see 2.2). At low θ therefore there is an almost linear relationship between θ and Δx. From this stage, in all subsequent work, only tracks for which a partner had been found in the lower emulsion are considered. On a piece of graph paper, with X in the upper emulsion and Δx as co-ordinates, the positions of all such tracks were recorded. Δx runs from -250μ to +250μ, the corresponding value of θ depending on t. X depends on the area scanned but was in the range 0 to 25 mm in all cases. On the X scale was recorded the average position of the fixed point, the central crossing point (C in Fig. 5b) of the grid lines.

Vertical components. The vertical distribution of the tracks was examined, where

$$\tan \varepsilon' = \Delta y/t. \qquad 4.2.2.$$

In figure 18 the vertical distribution of emission points in the target as recorded in C5 is compared with the vertical beam profile (Figure 14). Allowing for the distortion of the distribution due to emission angle, and emission points off centre in the target, it can be seen that particles detected in the central region of the plate were detected predominately in the same horizontal plane.

The maximum vertical angle of emission to reach the centre of the plate is 27°. For this angle the horizontal component of the momentum will be at its minimum value of 90% of the total momentum. This will tend to shift the highest momenta down by 40 MeV/c, but at 200 MeV/c the error is only 20 MeV/c. From figure 18 it can be seen that 82% of the particles have a horizontal component of more than 99% of their total momentum. Therefore, as assumed in chapter 2, the curvature of the track will give an accurate estimate of the momentum.

4.3. Method of Analysis

a) Reason for this method. Already in chapter 2 (see 2.2. and figure 6) the effect of the target has been

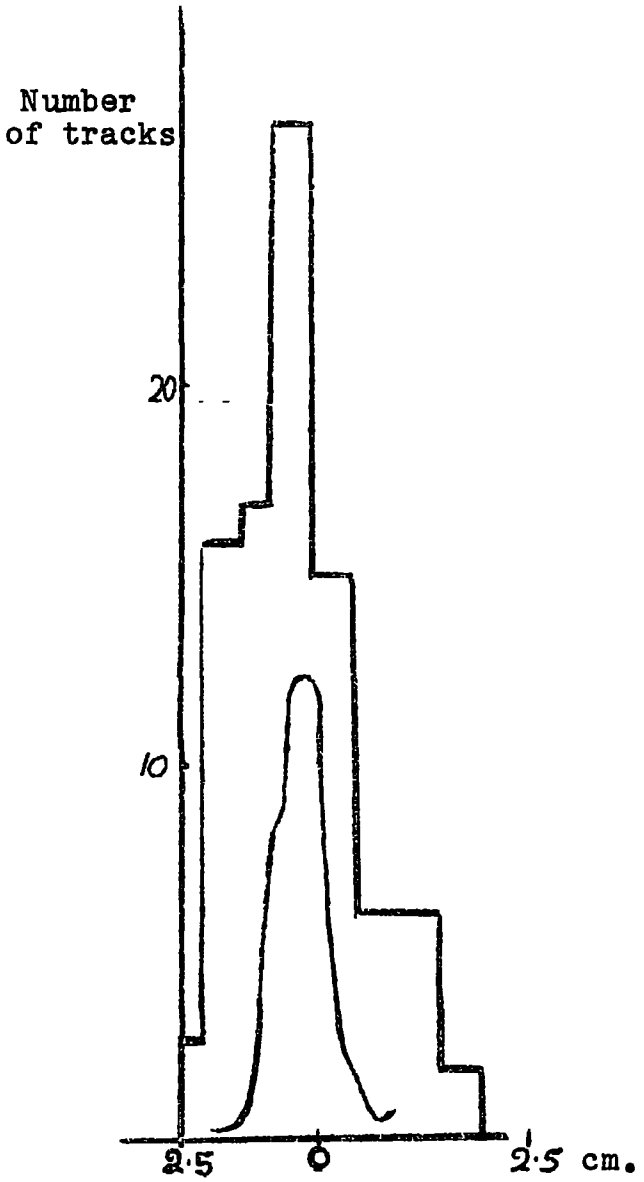

Vertical distribution of emission points in target for particles dectected in C5.The distribution in C4 was very similar.
The vertical intensity variation of the beam(see figure I4) is shown with the same horizontal scale.

Figure I8.

mentioned. If all the particles come from a point target, the charge on the particle would be easily determined from the curvature of the track, but the extent of the target in the horizontal plane alters both the apparent charge (see Fig. 19a) and the apparent momentum (see Figs. 6a and 19). Consider the tracks in figure 19b, OF is a straight line from O to the plate, and in fact represents infinite momentum of either charge at a given emission angle. P is the track of a negative particle emitted from O with 400 MeV/c. Many particles from the target of high momentum which strike the plate between P and F will leave a track of little or no apparent curvature with respect to O. The particle therefore will appear negative and of even higher energy, the nearer to F the higher the energy. This is so only for tracks which appear to have very little curvature with respect to O. Track A, the same curvature as P and therefore actually with the same momentum, when traced back to O, appears as a very high energy positive particle. Similarly track B, also the same curvature as P, appears as a negative particle of much lower energy, if O is the

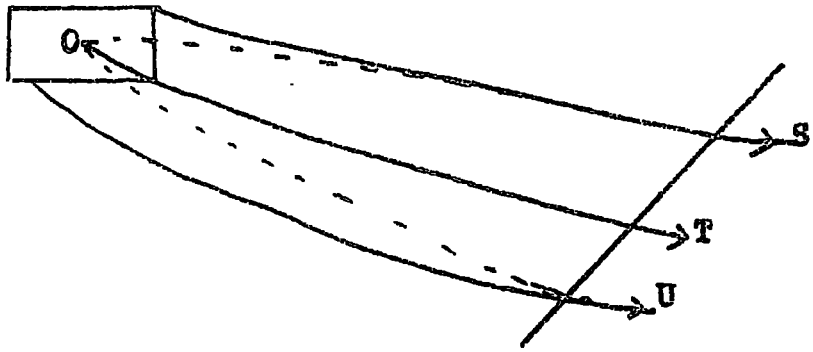

a) If O is taken as the point of origin then S and U which are negative and of the same momentum, appear to have different track curvatures, and S in fact appears to carry a positive charge.

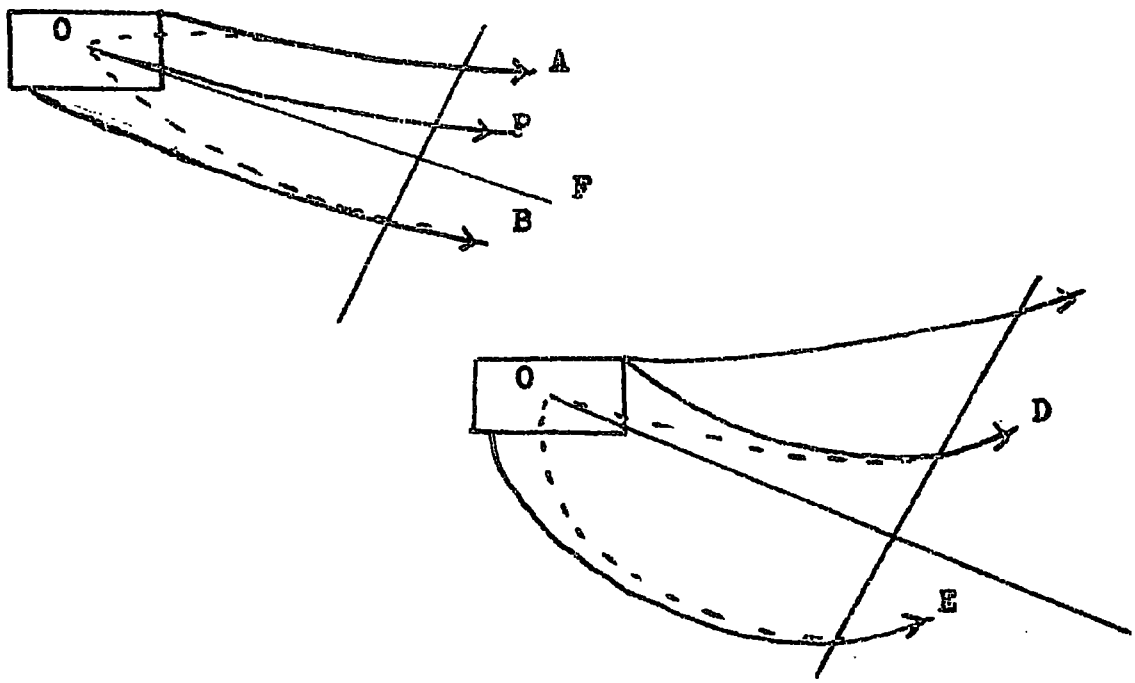

b) Alteration of track charge and momentum.
P is a negative particle emitted from O with about 400 MeV/c.

Figure 19.

assumed emission point. Thus tracks of 400 MeV/c negative pions emitted uniformly from all points in a horizontal cross-section of the target will appear with respect to O as very low energy negative pions through the whole range to infinitely high energy pions of either charge and as high energy positive pions.

Similarly tracks D and E are of low energy negative particles. If traced back to O, D appears to be of much high energy, and can even appear as of positive charge, while E appears to be of much lower energy.

When a simple computer program was run using O as the sole point of emission, as many positive as negative particles were obtained with apparent momenta running all the way up to infinite. Therefore a new method of analysis was used.

b) The analysis. For a particular plate of thickness t, the values of sinθ and Δx were plotted (see equ. 4.2.1). For this same plate the values of d (see 2.2) and A (equ. 2.2.3) are calculated from the original calibrations for each of the points B_o, O, and F_o (see Fig. 20a). Selecting a particular point of emission, values of x (Fig. 5a) (equivalent to different angles of

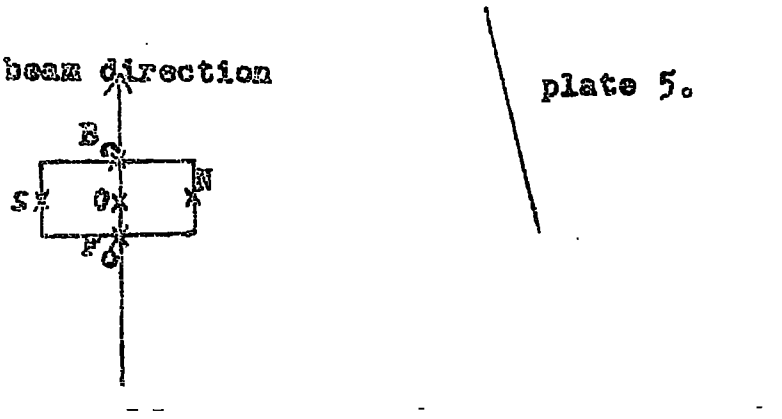

a) Path length and direction of beam in target.

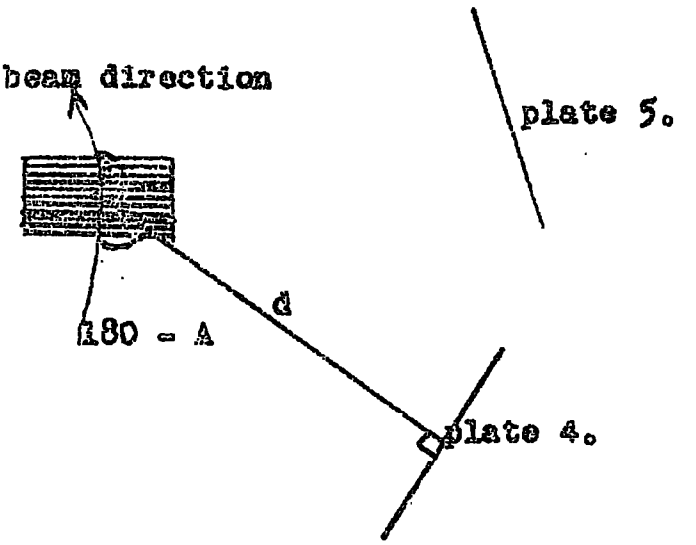

b) Division of target into equal segments.

Figure 20.

emission) from 0 to 2 cm are chosen, and values of $(\theta - \phi)$ (equ. 2.2.1) can then be obtained, also values for ρ for each x (equ. 2.2.2). The steps are as follows. Once x is chosen, then from equation 2.2.2, ρ is uniquely determined. A value of p is now selected. From equation 2.1.4, it can be seen that these values of ρ and p fix ϕ. ϕ is then substituted in $\theta - \phi$ in equation 2.2.1 and θ is obtained. Using this value of θ, Δx can now be calculated (see 4.2.1). For each p therefore we have x and Δx. Five values of p, 100, 200, 300, 400 and 500 MeV/c, were used. So it is now possible for each emission point, for example F_o, to choose a particular momentum, and from the above calculation determine the values of Δx and x which will be observed for a particle emitted from F_o with this momentum.

On the X- Δx plot (see 4.2b) curves are drawn for each momentum, showing where the tracks will occur for target positions corresponding to B_o, 0 and F_o. For any one target position, the momentum curves turn out to be almost parallel and sensibly straight lines. The diagram is then divided into equally spaced channels,

which are arbitrarily numbered. The channels run parallel to the lines of constant momentum. Figure 21 shows a typical plot without the points for the observed tracks. All plates which occupied the same position in the spectrograph, have the channels marked off in the same x- Δx positions. The relative values of x and X depend on the co-ordinates of C, and its distance from d (see 2.3). It can be seen in figure 21, that particles of different momentum can reach the same parts of a plate with identical inclinations provided they originate in different regions of the target. Moreover, any high momentum positive particles will fall into the channels expected for the high momentum negative particles.

If the initial momentum spectrum of the scattered particles is known, from the distribution of scattering points in the target the number of particles falling into each of these channels could in theory be calculated. In fact the number of target scattering points is uniform in depth ($F_o \rightarrow O \rightarrow B_o$) and proportional to the beam intensity ($S \rightarrow O \rightarrow N$, Fig. 19a). The number of tracks falling into some arbitrary channel A is N_A, where

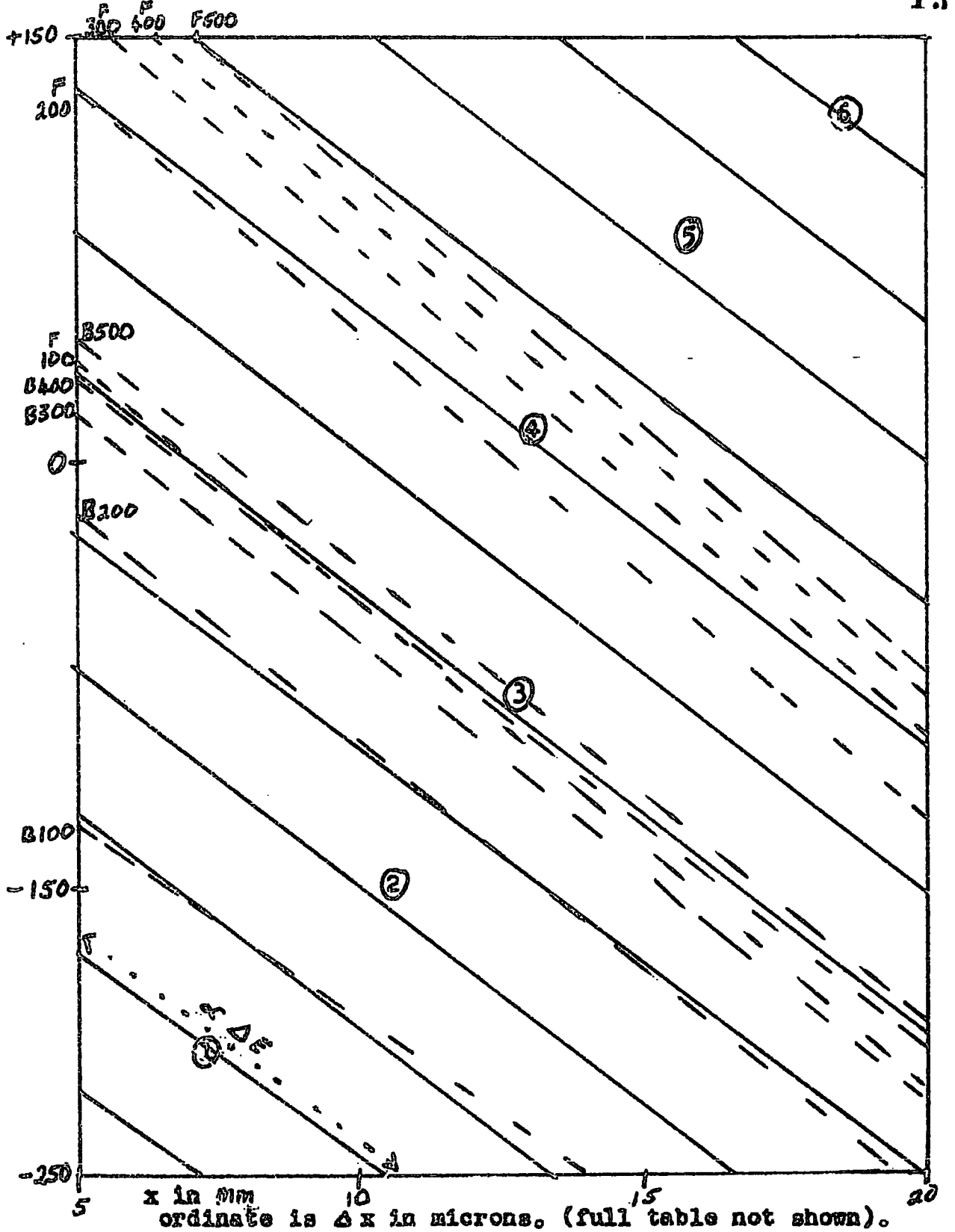

ordinate is Δ x in microns. (full table not shown).

F and B refer to target positions, number is momentum in MeV/c.

Figure 21.

$$N_A \propto \frac{d\sigma}{d\Omega} \cdot \Delta\mathcal{E} \cdot \left(n(p_o)\Delta p_o + n(p_{F_o})\Delta p_{F_o} + n(p_{B_o})\Delta p_{B_o}\right.$$

$$\left. + \text{all intermediate positions}\right)$$

for $B_o \rightarrow 0 \rightarrow F_o$.

where $n(p_1)$ is the number emitted in momentum interval p at position 1.

Now $\Delta\mathcal{E}$, the angular width subtended by channel A at the target, is proportional to the length of the straight line on the graph (see Fig. 21), and is constant over a large area of the plot and $\frac{d\sigma}{d\Omega}$, the differential cross-section is approximately constant. Therefore the 'density' of tracks is

$$\frac{N_A}{\text{Length of A}} \propto \frac{N_A}{\Delta\mathcal{E}} \propto \sum_{i=F_o}^{B_o} n(p_i)\Delta p_i \qquad 4.3.1.$$

i.e. the track density automatically eliminates the angular dependence and depends only on the momentum spectrum of the scattered particles.

The problem is to find n(p) from the track density, for this a fixed Δp of 50 MeV/c is assumed. A matrix

is formed which gives the proportion of this Δp at a particular value of p which falls into channel A, channel B, etc. for particles scattered at a particular level in the target.

The target is divided into 10 0.1 cm strips parallel to the beam, as shown in figure 20b. For a target position in the centre of each strip, X and Δx for each p are determined. In practice it is possible to interpolate between positions, and calculations need not be made for every strip.

The channels into which the various momenta from each target position fall, are plotted as shown in figure 22. The matrix is assembled from this graph by tabulating as follows:-

Channel A contains - 110 - 140 MeV/c from B_o 60% of $\Delta p = 50$

Channel B contains - 140 - 160 MeV/c from B_o 40% of $\Delta p = 50$

and 100 - 120 MeV/c from C 40% of $\Delta p = 50$

etc.

The matrix is then modified to allow for emission points across the width of each strip (S→O→N). The beam intensity however falls off rapidly, dropping to half-

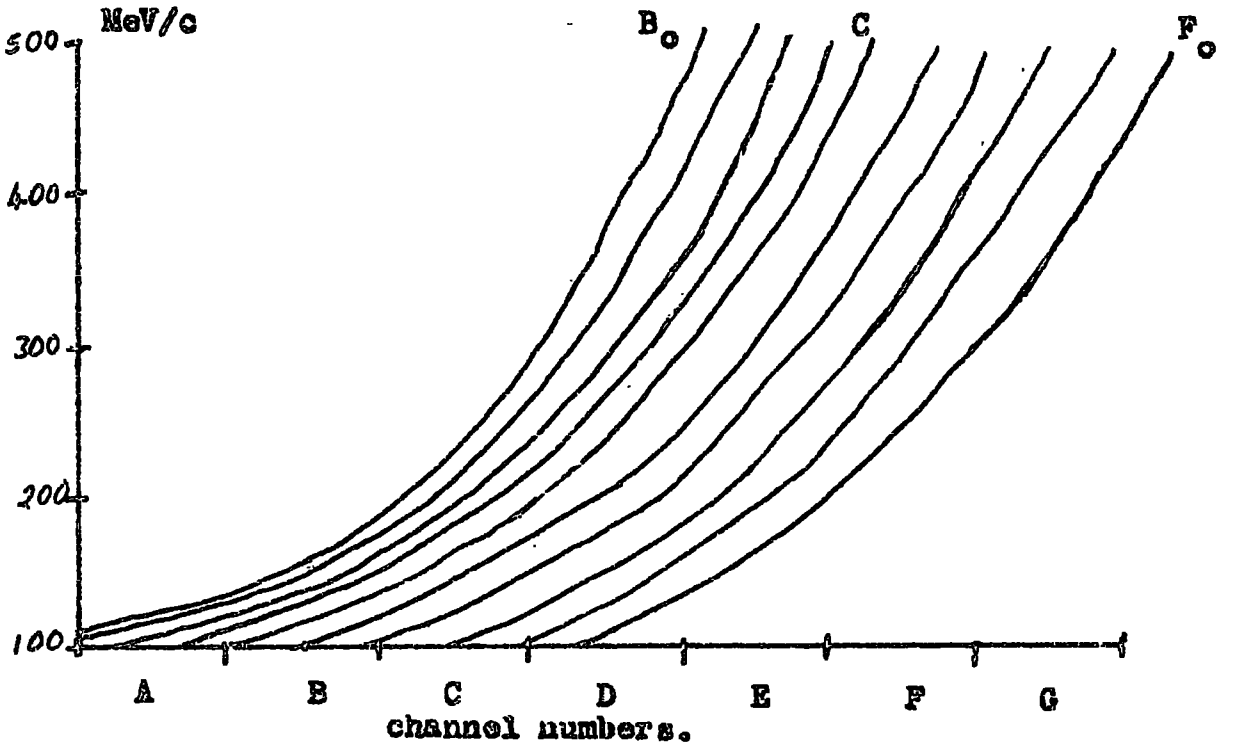

The channels into which the various momenta from each target position fall.

Figure 22.

height at 0.1 cm from the central peak and having a total width of less than 0.4 cm altogether (see figure 14). Therefore the modification for beam width is quite small. Then the matrix is normalised to 100% for each momentum interval. This gives the matrix N(s, p) where s is the channel number and p the momentum.

A computer program was written, which, given an initial momentum spectrum I(p) of particles emitted from the target, would calculate the expected distribution of tracks per channel. For each particular plate the matrix N(s, p) was calculated as given above for channel number s and for momentum p from 100 to 500 MeV/c. An assumed emission spectrum I(p) for the target was then chosen, and the matrix M(s) formed, where

$$M(s) = N(s, p) \times I(p).$$

M(s) is the expected track density in channels and can be compared after correction for spurious contribution from the dummy run.

As has already been mentioned, high energy positive

particles will fall into the same channels as the high energy negative particles. Those channels in which positive particles will be found can be determined, but the exact positive contribution cannot be determined with accuracy. The effect is more important in C4 where the negative particles occupy a smaller number of channels. The momentum spectrum I(p) was therefore fitted over those channels which could not be occupied by any contribution from positive particles, channels 1→3 in C4, and channels 1→6 in C5. The positive particles cannot be identified since only momenta and charge, but not mass, occur in the trajectory equations (see section 2.1).

4.4. Results of the Spectrographic Exposures

a) Results of the dummy run. The conditions under which the dummy run was made have already been described in 3.3 and 3.4. Despite the changes made in the spectrograph, a preliminary scanning of the plates revealed a very high background in plates from positions 1 and 2. After comparing the dummy plates with those exposed around a carbon target, it was concluded that the

ratio of background to secondary tracks was too high in these two positions. For the dummy run therefore plates from positions 4 and 5 were concentrated on, and hereafter are referred to as plates D4 and D5 respectively.

Table VII shows the results as the density of tracks per channel for D5. As expected for general background, the density is evenly distributed over all channels, and therefore over the whole area of the scan. This background will include external radiation, and particles scattered within the detecting system.

The results for D4, Table VIII, show the same even background distribution per channel. The fluctuations are within the experimental error.

b) The exposure to a carbon target. The plates exposed with the carbon target in position were labelled C4 and C5 in positions 4 and 5 respectively. The angle A the perpendicular to the plate makes with the beam (alreadt defined in chapter 2) is 68° for positions 5 and 121° for position 4. Sampling is therefore predominantly centred on these two angles.

Observed Track 'Densities' in D5.

channel no:	0	1	2	3	4	5	6
'density'	0.50	0.95	0.84	0.83	0.88	1.04	0.69
error ±	0.20	0.20	0.17	0.14	0.13	0.13	0.10

channel no:	7	8	9	10	11	12
'density'	1.04	1.08	1.01	1.27	0.93	0.78
error ±	0.13	0.13	0.13	0.15	0.13	0.13

channel no:	13	14	15	16
'density'	0.86	0.96	0.51	1.06
error ±	0.14	0.20	0.16	0.30

TABLE VII

Observed Track 'Densities' in D4.

channel no:	0	1	2	3	4	5	6
'density'	0.97	1.24	1.25	1.15	1.08	0.78	0.99
error ±	0.25	0.21	0.18	0.15	0.14	0.16	0.20

TABLE VIII

Table IX gives the value for t, d and δ (see figures 5b and 17) for the plates on which extensive measurements were made. The most important variation is in δ, which was therefore measured with a very high degree of accuracy.

In C5 and D5, equal areas of 51.7 mm^2 were scanned. The results are shown in Table X, and figure 23. The central channels can clearly be seen to contain the scattered pions.

The channels in C4 are spaced and numbered as in D4, the foot of the perpendicular to the plate being used as the reference in both cases. The area scanned in C4 was 13.2 mm^2 compared with 24.7 mm^2 in D4. A greater area was scanned in the dummy plate in order to achieve better statistics for the background. Unlike D4, the track density in C4 varies with channel number with a maximum in channel 3 (see Table XI).

c) <u>The plates exposed with a silver target</u>. Preliminary examination of the plates exposed with a silver target in position revealed that because of the extremely high background, the signal/background ratio was very small. Much larger areas would have to be

Plate constants

Plate	t in μ error ± 20 μ	d in mm error ± 0.1 mm	δ in mm error ± 0.005 mm
D5	865	53.84	-2.19
C5	845	54.16	-1.68
D4	850	54.50	+2.79
C4	885	54.50	+2.79

t is shown in figure 17.

d and δ are shown in figure 5b.

TABLE IX

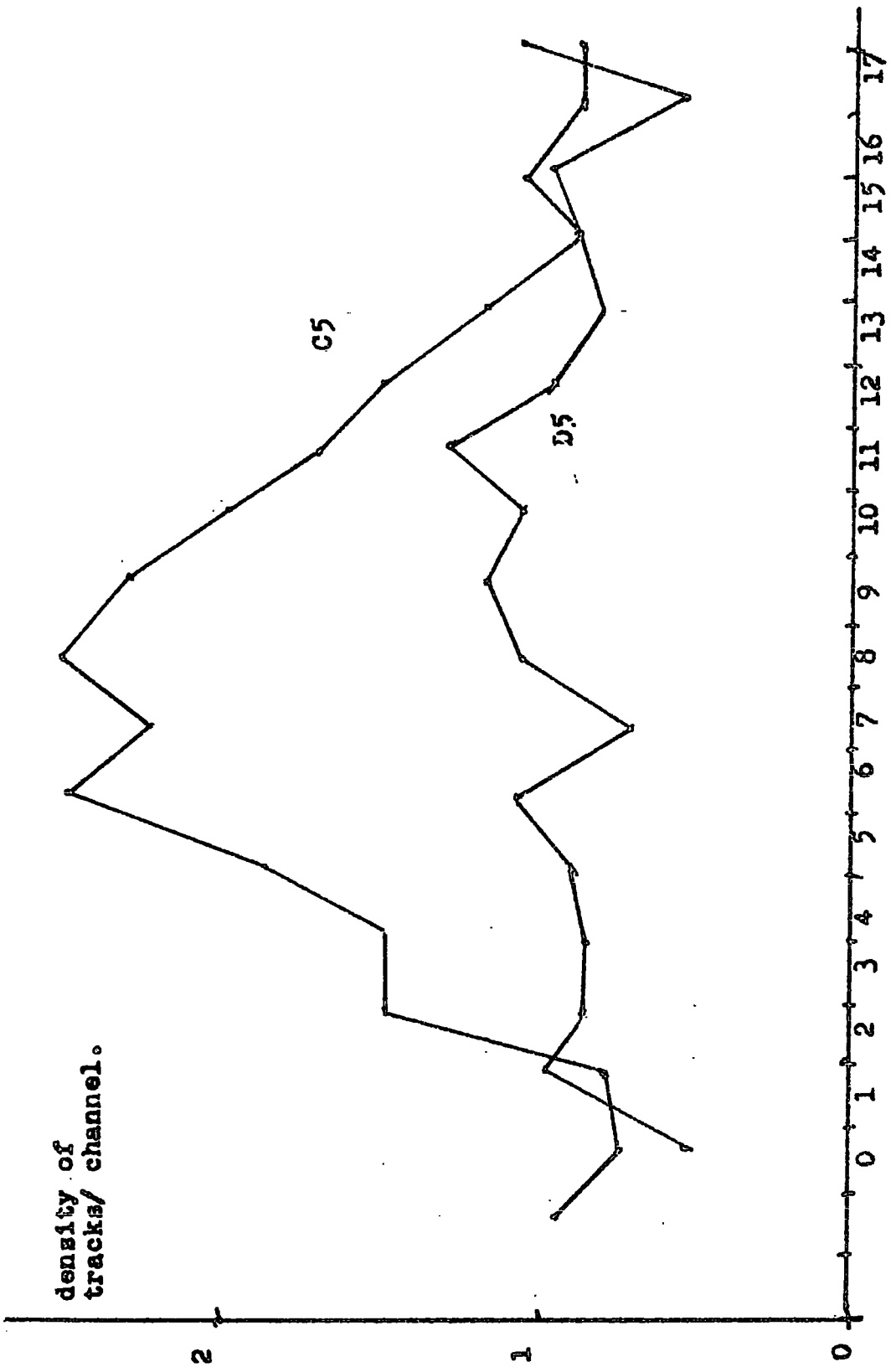
density of
tracks/ channel.
2
1
0
C5
D5
0 1 2 3 4 5 6 7 8 9 10 11 12 13 14 15 16 17
channel number

Figure 23.

scanned, than in the plates exposed with a carbon target, in order to achieve good statistics.

d) The signal. In order to estimate the signal accurately it is necessary to normalise the results from the dummy plates so that the total exposure and area scanned are equivalent to that in the plates exposed with a target.

Equal areas have been scanned in C5 and D5, therefore D5 was normalised, so that the densities were corrected only for the different exposure times by the factor

$$\frac{\text{length of C exposure}}{\text{length of D exposure}} = 1.07 \qquad 4.4.1.$$

The normalised densities in D5 and the resulting signal are shown in Table X

The densities in D4 naturally require the same correction for exposure time as those in D5, see equ. 4.4.1. In C4 the area scanned was 0.53 (13.2/24.7) of that scanned in D4. An additional correction was needed since the channel lengths were not equal in the two plates. This additional correction was the ratio of the

channel	D5 unscaled	D5 scaled	C5 density	signal
1	0.95 ± 0.20	1.02 ± 0.20	0.76 ± 0.16	-0.26 ± 0.3
2	0.84 ± 0.17	0.90 ± 0.17	1.48 ± 0.20	0.58 ± 0.3
3	0.83 ± 0.14	0.89 ± 0.14	1.46 ± 0.18	0.57 ± 0.2
4	0.88 ± 0.13	0.94 ± 0.13	1.83 ± 0.18	0.89 ± 0.2
5	1.04 ± 0.13	1.11 ± 0.13	2.47 ± 0.20	1.36 ± 0.2
6	0.69 ± 0.10	0.74 ± 0.10	2.20 ± 0.18	1.46 ± 0.2
7	1.04 ± 0.13	1.11 ± 0.13	2.29 ± 0.17	1.18 ± 0.2
8	1.08 ± 0.13	1.16 ± 0.13	2.28 ± 0.19	1.12 ± 0.2
9	1.01 ± 0.13	1.08 ± 0.13	1.98 ± 0.17	0.90 ± 0.2
10	1.27 ± 0.15	1.36 ± 0.15	1.68 ± 0.16	0.32 ± 0.2

In channels 0 and 11 to 16, the signal is very low and oscillates around zero.

The signal in C5.

TABLE X

lengths of the channel in D4 and C4. The final correction was therefore

$$1.07 \times 0.53 \times \frac{\text{length in D}}{\text{length in C}}$$

The scaled densities and resulting signal are shown in Table XI.

e) Plate efficiencies. The plate detection efficiency has already been discussed in chapter 2 (see 2.5), where the solid angle subtended at the centre of the target was calculated, and the selective detection of momentum was mentioned.

The size of the target has a negligible effect on the solid angle, the variation for different emission points naturally being of the same order as that for the different emission angles - an average of 12%. For particles in the same plane, it is 6%.

The selective detection of momenta at the plate edges can be seen from the channel-momenta matrices. Channel 1 which lies to one side of the plate contains predominantly low momenta. However as long as $\psi(\tan^{-1} X/d)$ remains small ($\lesssim 20°$) the channel length

channel	D4 unscaled	D4 scaled	C4 density	signal
1	1.24 ± 0.21	0.98 ± 0.17	1.13 ± 0.25	0.15 ± 0.3
2	1.25 ± 0.18	0.99 ± 0.14	1.97 ± 0.25	0.98 ± 0.3
3	1.15 ± 0.15	0.91 ± 0.12	3.16 ± 0.29	2.25 ± 0.2
4	1.08 ± 0.14	0.85 ± 0.11	2.54 ± 0.25	1.69 ± 0.2
5	0.78 ± 0.16	0.62 ± 0.13	1.77 ± 0.22	1.15 ± 0.2
6	0.99 ± 0.20	0.78 ± 0.16	1.23 ± 0.18	0.45 ± 0.3

The Signal in C4

TABLE XI

is proportional to the emission angle over which particles are detected. Table XII shows this range for C4 and C5. The total angular range detected by the plate for any one target emission point is about 20°. The emission angle detected falls off very slowly with the vertical co-ordinate of the emission point on the target, the greatest variation being 5° between the centre and the extremity of the target. If the mean emission angle is calculated for the target centre, and taken as the mean for the whole target, the error is only $\pm$ 1°. The 'density' of tracks per channel was the variable used, and this should be proportional to the density of tracks per angle of emission. In those cases where approximate calculations were made to check this assumption, the error was $\pm$ 5%. The matrix method therefore automatically corrects for plate efficiencies during the calculation.

f) Scanning efficiency. The efficiency of detecting a track depends on its total projected length in the top emulsion. Steep tracks perpendicular to the surface are more efficiently detected than those tracks with a much greater projected length, since it was the

Plate	$\bar{p}$ MeV/c	centre of target angular range	mean angle
C4	100	126 - 140	132
	200	120 - 135	127
	400	117 - 132	124
C5	100	69 - 91	80
	200	63 - 87	75
	400	61 - 82	72

angular range - average range from total height of target along central certical line.

mean angle - mean angle for central point of target, the error on this is only $\pm$ 1° if it is taken as the mean for the whole target (see text).

TABLE XII

steep tracks for which the scanner was looking, and longer tracks were to some extent lost in the background of long tracks running across the emulsion. Usually therefore high momenta were detected more efficiently than low momenta. The corrections are shown in Table XIII.

g) The determination of the initial momentum spectrum. The best fit to the observed data, tables X and XI, was obtained using the computer program mentioned above (section 4.3.b) by which the momentum spectrum of the scattered mesons is determined. It is shown in figure 24 for plate C5 and figure 25 for plate C4. The corresponding momentum distributions are shown in table XIV. The program was originally run ignoring the possibility of positive particles reaching the plates. Under these circumstances the results for C5 were acceptable because 6 channels receive negatively but not positively charged particles. Plate C4 requires a double peaked momentum curve, the peaks occurring at 125 MeV/c and 325 MeV/c, if all track densities are assumed to be due to negative particles. Fits were therefore made to those channels which could not contain positive particles.

Scanning Efficiency

Momentum MeV/c	C4	C5
100	90 ± 10%	64 ± 20%
400	92 ± 6%	84 ± 12%

Estimated Errors

Error as % due to -	Plate	Momentum MeV/c. 100	200	400
	C5			
solid angle		0	11	6
energy loss in target		10	2	0
Total		10	13	6
	C4			
solid angle		0	0	0
energy loss in target		10	2	0
Total		10	2	0

TABLE XIII

[illegible] progress

to the final density/channel results for plate 65.

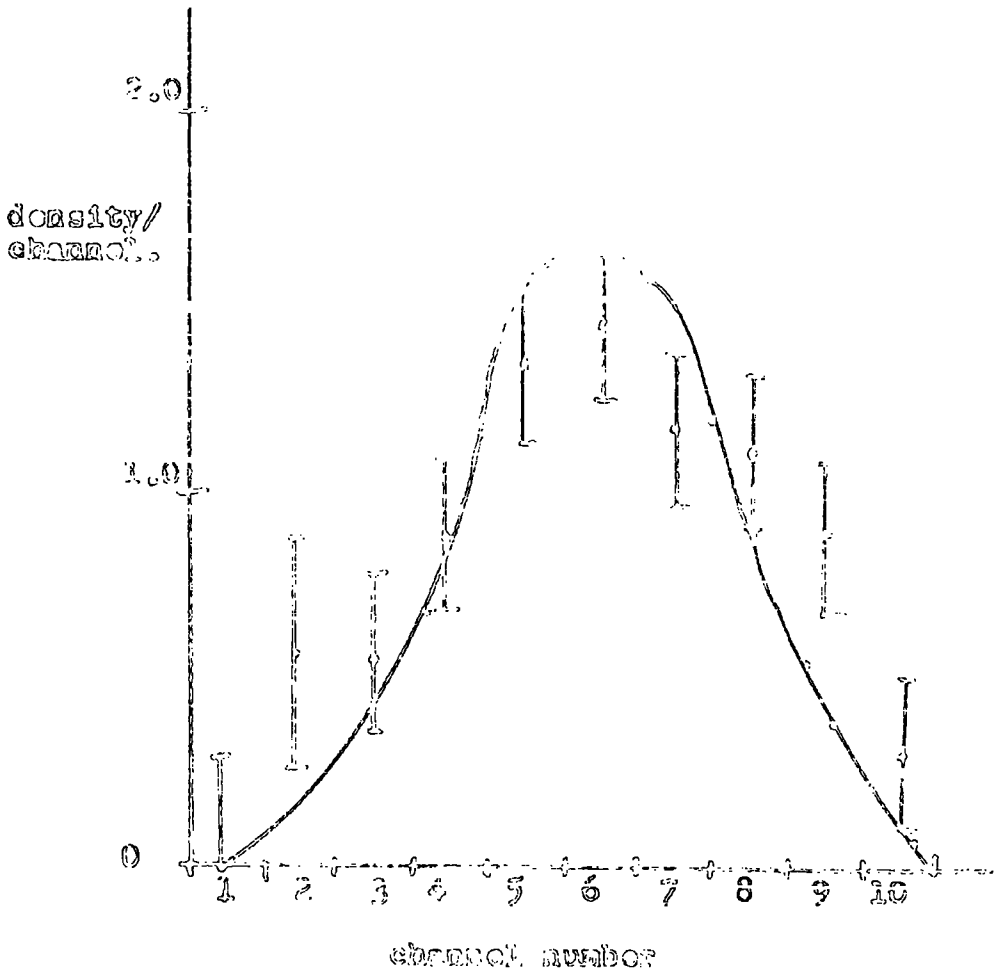

Figure 46.

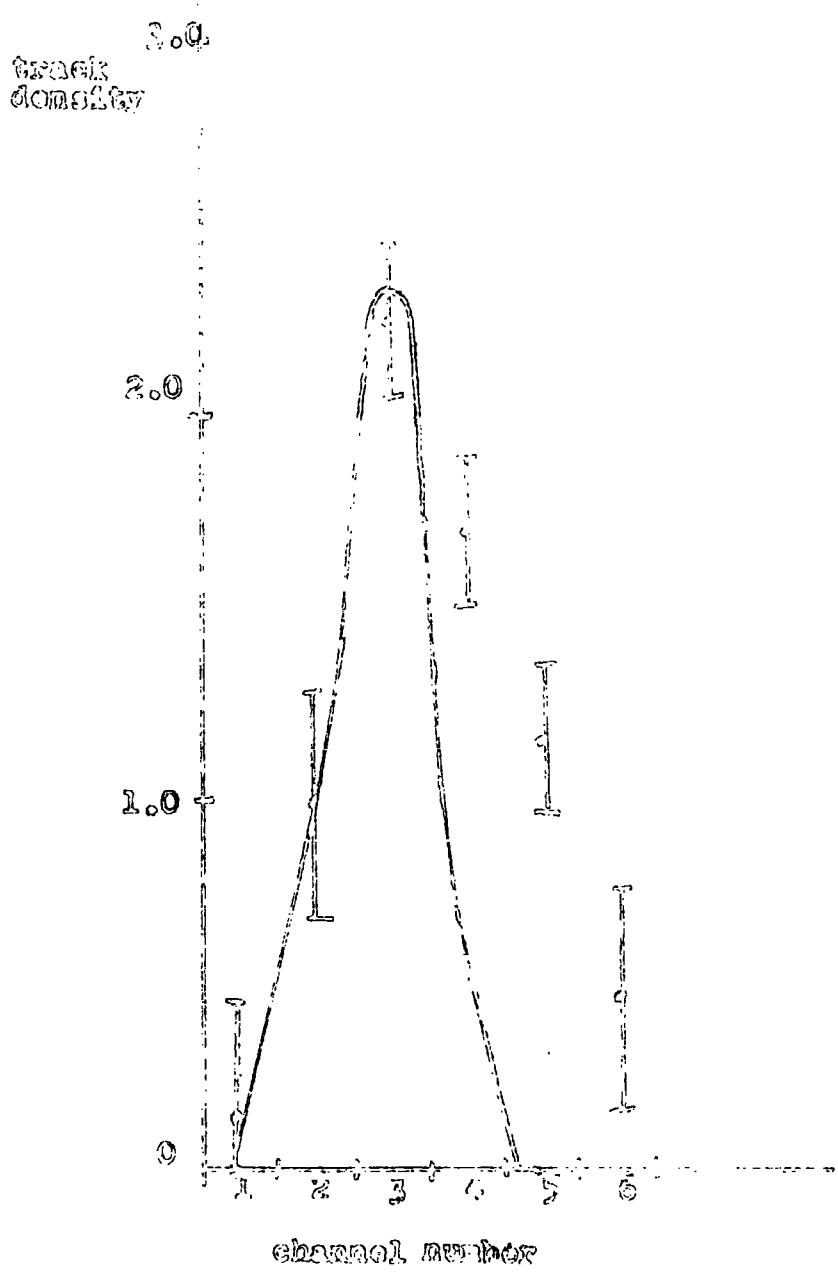

Figure 25c

In plate C5 the fit was made to channels 1 - 6, since any positive particles would be expected to fall in channels 7 - 14. It is this fit which is shown in figure 24.

Plate 24 samples angles in the backward direction, where the momentum is expected to be low. It is precisely this area where the greatest uncertainty will occur. Firstly, for example, pions with momenta of 100 MeV/c after scattering may leave the target with only 80 MeV/c because of energy loss (see section 2.5). This will tend to bias the measured momenta towards low values, that is the lower momentum channels will contain particles whose original scattered momenta belonged to higher channels. This effect is only important for momenta below 150 MeV/c. Secondly, pions emitted with very low momenta are so strongly deflected in the magnetic field, that they never reach the recording plate. For this spectrograph, pions emitted with momenta less than 80 MeV/c will firstly lose energy in the target, and secondly be trapped in the magnetic field. The bias to low momenta and the trapping in the field are important in momentum channels 1 and 2. Channel 1 will

The momentum spectra which provide the best fit to the channel density curves.

Spectra were fitted over channels 1 - 6 in C5 and channels 2 and 3 in C4.

momentum MeV/c.	C4	C5
100 - 150	15 (20)	2 (5)
150 - 200	10 (15)	20 (22)
200 - 250	7	33
250 - 300	4	20
300 - 350	2	5
350 - 400	1	3
400 - 450	0	2
450 - 500	0	0
mean p	188 $\pm$ 20 MeV/c	239 $\pm$ 10 MeV/c

TABLE XIV

contain particles originally scattered with momenta of less than 100 MeV/c, and also particles which have lost energy in the target. This means that a momentum spectrum fit can only be made to channels 2 and 3, and that only the very roughest estimate of the spectrum can be made. The channel contents for plate C4 are summarised in table XV.

Since low momenta particles are lost, and high momenta particles are obscured by positive tracks, the ends of the momentum spectrum are uncertain. The errors quoted on the mean p in table XIV are due to the uncertainty of the momentum spectrum at high and low momenta. The figures in brackets, in table XIV show the corrected figures if maximum absorption took place.

4.5. Pβ Measurements in Conventional Exposure.

The plates from the emulsion stack were examined on a Cooke microscope under a magnification of 80 x 1.5 x 15, and on a Koristka R4 under a magnification of 62 x 2 x 15. Tracks within five degrees of a chosen angle to the beam direction, were picked up 1 cm from the

Occupation of channels in plate C4.

channel	contribution
1	a) negative particles below 100 MeV/c from back of target.
	b) negative particles between 100 - 150 MeV/c, which have undergone further energy loss.
2	negative particles between 100 - 150 MeV/c, from the back half of the target.
3	negative particles between 100 - 500 MeV/c.
4	a) negative particles of 200 - 500 MeV/c, from front half of target.
	b) positive particles of 500 - 250 MeV/c, from back half of target.
5	positive particles between 500 - 80 MeV/c.
6	positive particles of below 200 MeV/c, from the front half of the target.

The momenta quoted are those of the secondary meson after the initial scatter in the carbon target.

TABLE XV

edge of the plate, and scattering measurements made on them. The cell lengths used were 200μ and 300μ, and the angles selected were 20°, 45°, 75°, 90°, 135° and 157° (see Fig. 26). The accuracy on each measurement was about 10%. Ten or more individual measurements were made at each angle.

The evaluated pβ was assumed to refer to the centre of the track. The distance of this point from the emulsion edge at the point of entry was measured, and the momentum calculated at entry from the tables of Barkas (1958). Further correction was made for the range of the secondary in the carbon target. It was assumed that the scattering occurred along the central axis of the target. In the case of 20° scatterings the interactions take place near the entrance of the target; for 135°, near the exit. The primary energies differ by about 25 MeV. To allow for this the secondary pion energies were scaled so that the primary energy is 285 MeV.

a) 75°. Detailed measurements were made at 75 ± 5° to the original beam direction. 79 pion tracks were measured in all. The results after correction for energy loss in emulsion and carbon are shown in figure 27.

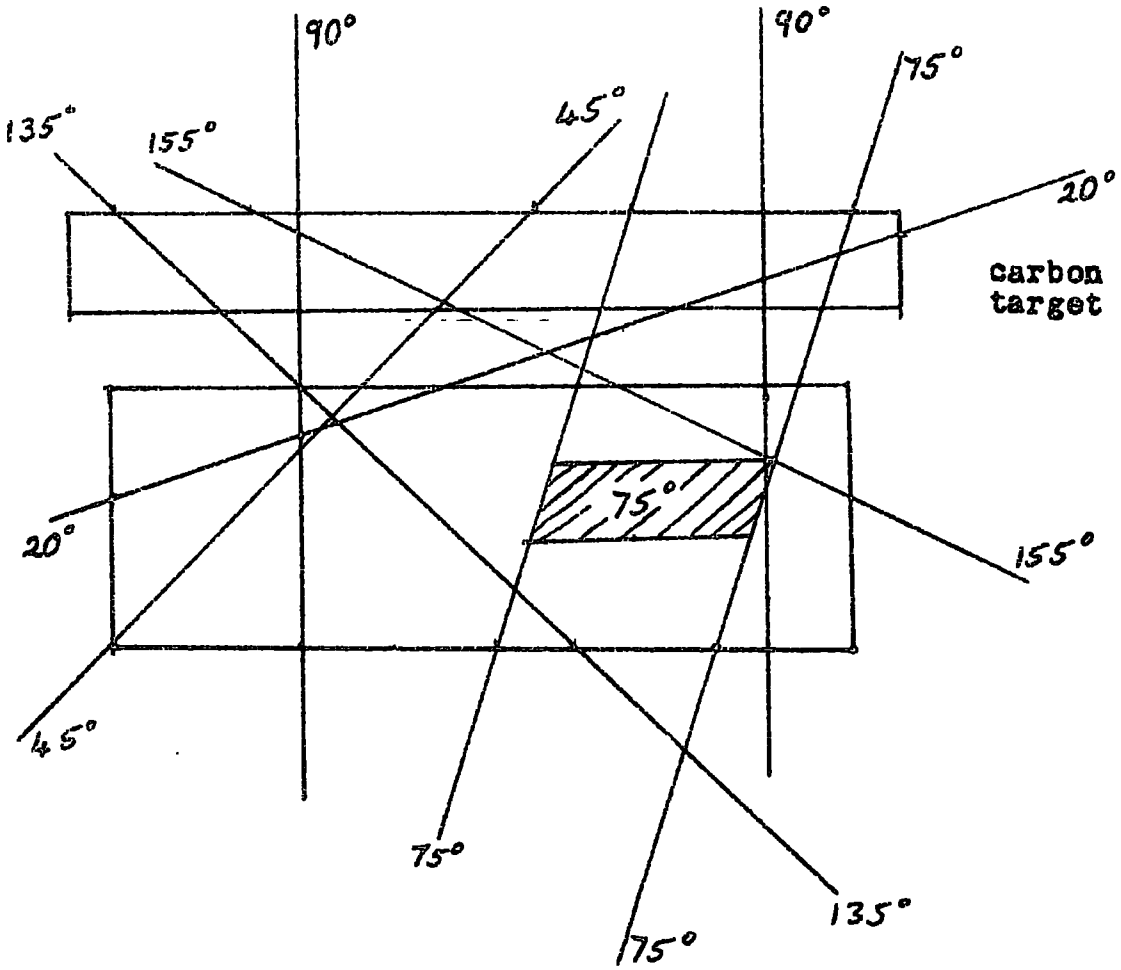

Regions of the solid block over which $p\beta$ measurements were made. (Drawn to size.)

Figure 26.

Scattering at 75°

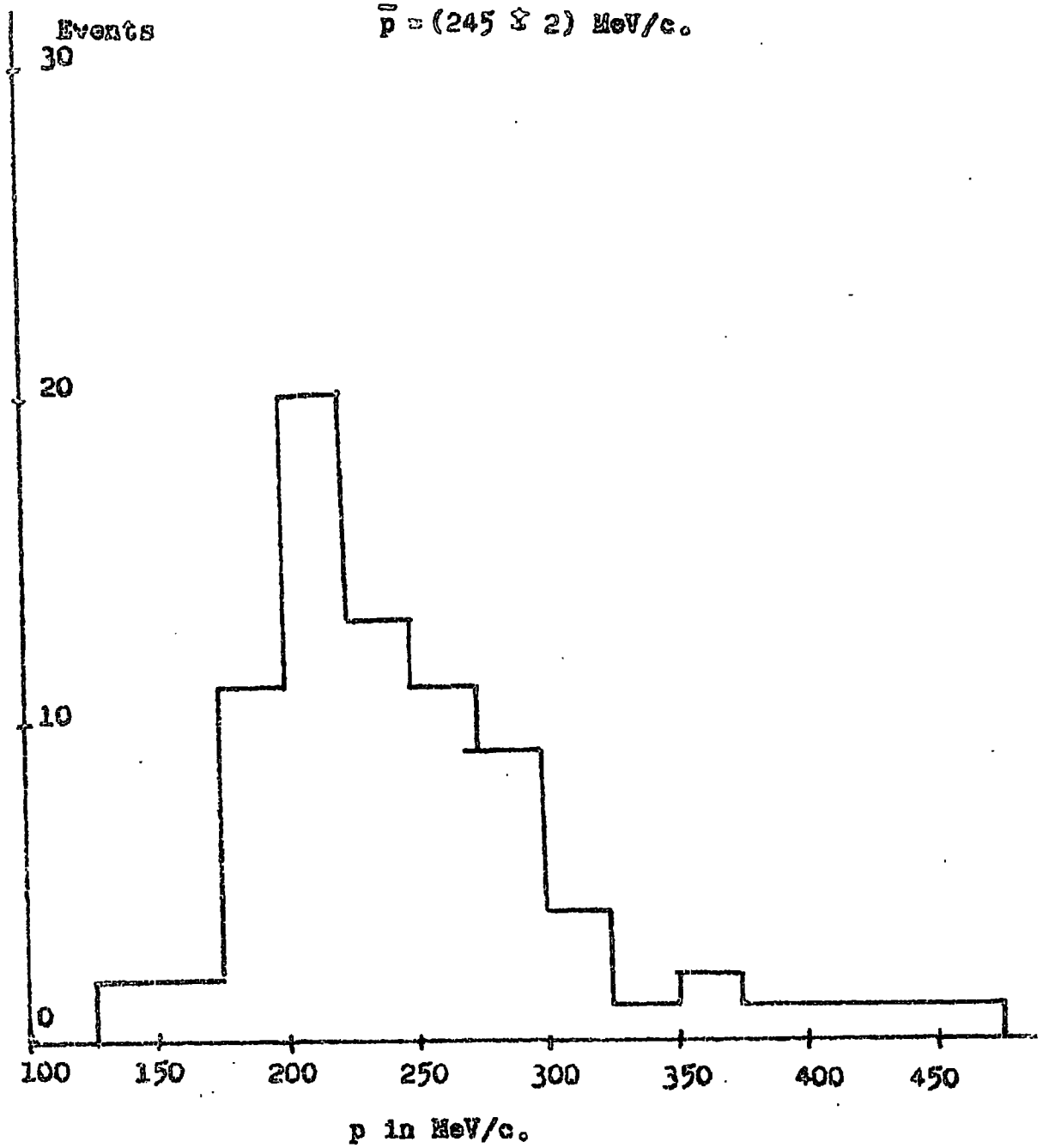

79 tracks. Average measuring error 22 MeV/c.

pβ measurements corrected for energy loss in target and in emulsion.

Figure 27.

The distribution is uniquely peaked between 200 and 225 MeV/c, the peak being broader on the high momentum side. The average momentum is 245 ± 2 MeV/c.

b) 90°. 180 tracks whose angle with the beam direction was 90 ± 5° were measured. The values for pβ were corrected for energy loss in the target and emulsion as before. The results are shown in figure 28. There is one broad peak at around 200 MeV/c, and the average momentum is 228 ± 2 MeV/c.

c) Other angles. Only a brief inspection of the secondary momentum at other emission angles was made.

10 tracks were measured up whose average emission angle was (20 ± 1)°. Of these 10 tracks, one appeared to be an elastic scatter with momentum approaching that of the incident beam. The average momentum of the remaining 9 was 343 ± 13 MeV/c.

At 45 ± 2° to the incident beam, 17 tracks gave an average momentum of 283 ± 15 MeV/c.

9 tracks at (135 ± 5)° to the main beam had an average of 171 ± 12 MeV/c, and ten tracks at (157 ± 3)° gave an average of 181 ± 12 MeV/c. All momenta have

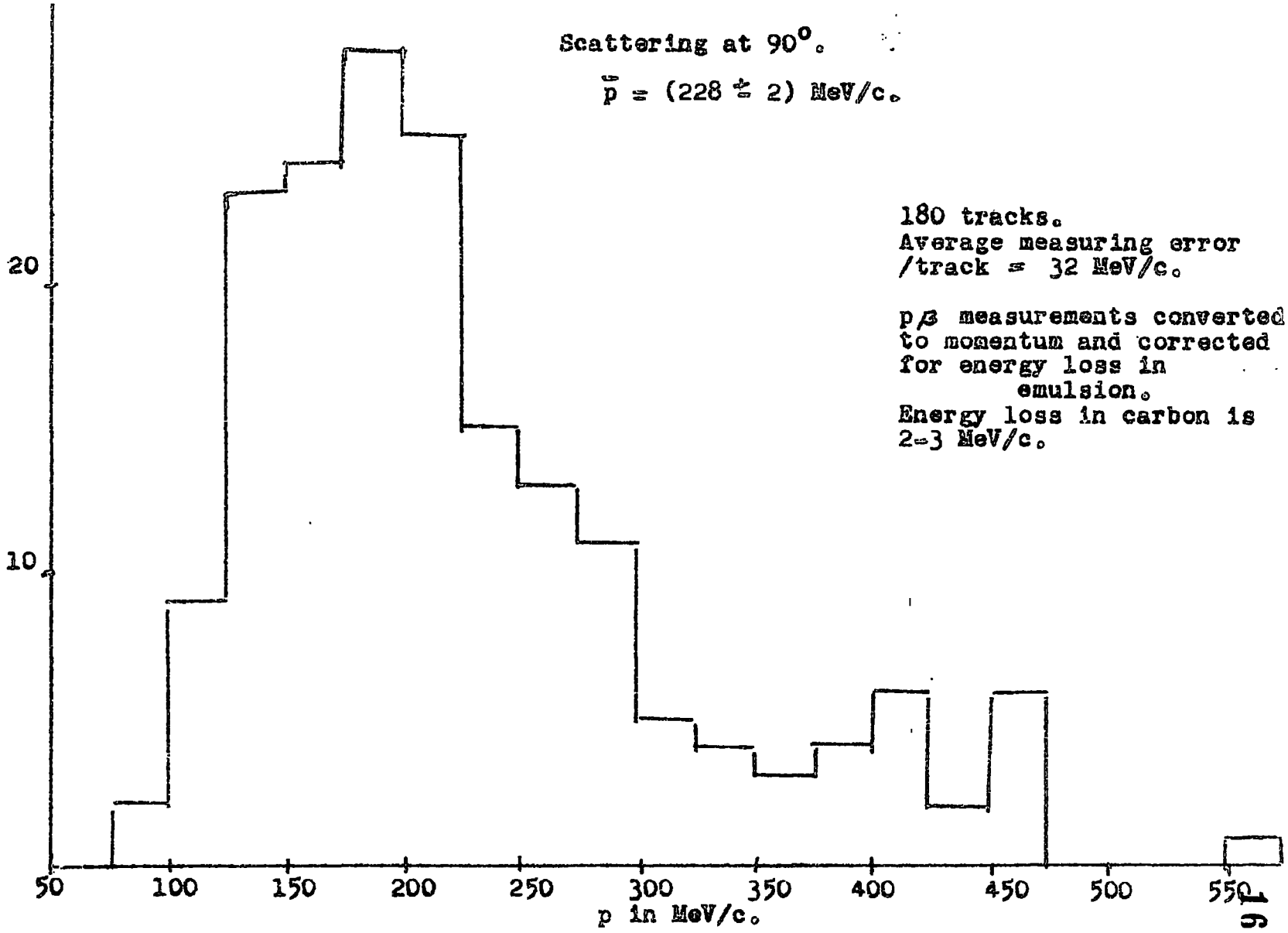
Scattering at 90°.
$\bar{p}$ = (228 ± 2) MeV/c.
180 tracks.
Average measuring error /track = 32 MeV/c.
pβ measurements converted to momentum and corrected for energy loss in emulsion.
Energy loss in carbon is 2-3 MeV/c.
20
10
50
100
150
200
250
300
350
400
450
500
550
p in MeV/c.

Figure 28.

been corrected for energy loss in the emulsion and target.

d) Momentum spectrum. In figure 29 is shown the secondary momentum versus emission angle spectrum obtained from the $p\beta$ measurements. This shows the expected decrease in momentum at high angles of emission, the average momentum in the backward direction being around 180 MeV/c. At each emission angle the actual momentum spread is quite considerable however, as can be seen from figures 27 and 28.

4.6. Results and Conclusions on Technique.

a) Comparison of conventional and spectrographic exposures. If the mean momentum in table XVI for C5 is compared with that obtained at 75°, very good agreement is observed. Comparison of the actual momentum distributions using a χ^2 test, has a probability $p = 0.5$. In the conventional $p\beta$ measurements, particles with low momenta would lose energy and be scattered as in the spectrographic exposure, and therefore this end of the distribution has the largest errors. The distributions

Variation of average secondary momentum with emission angle from $p\beta$ measurements.

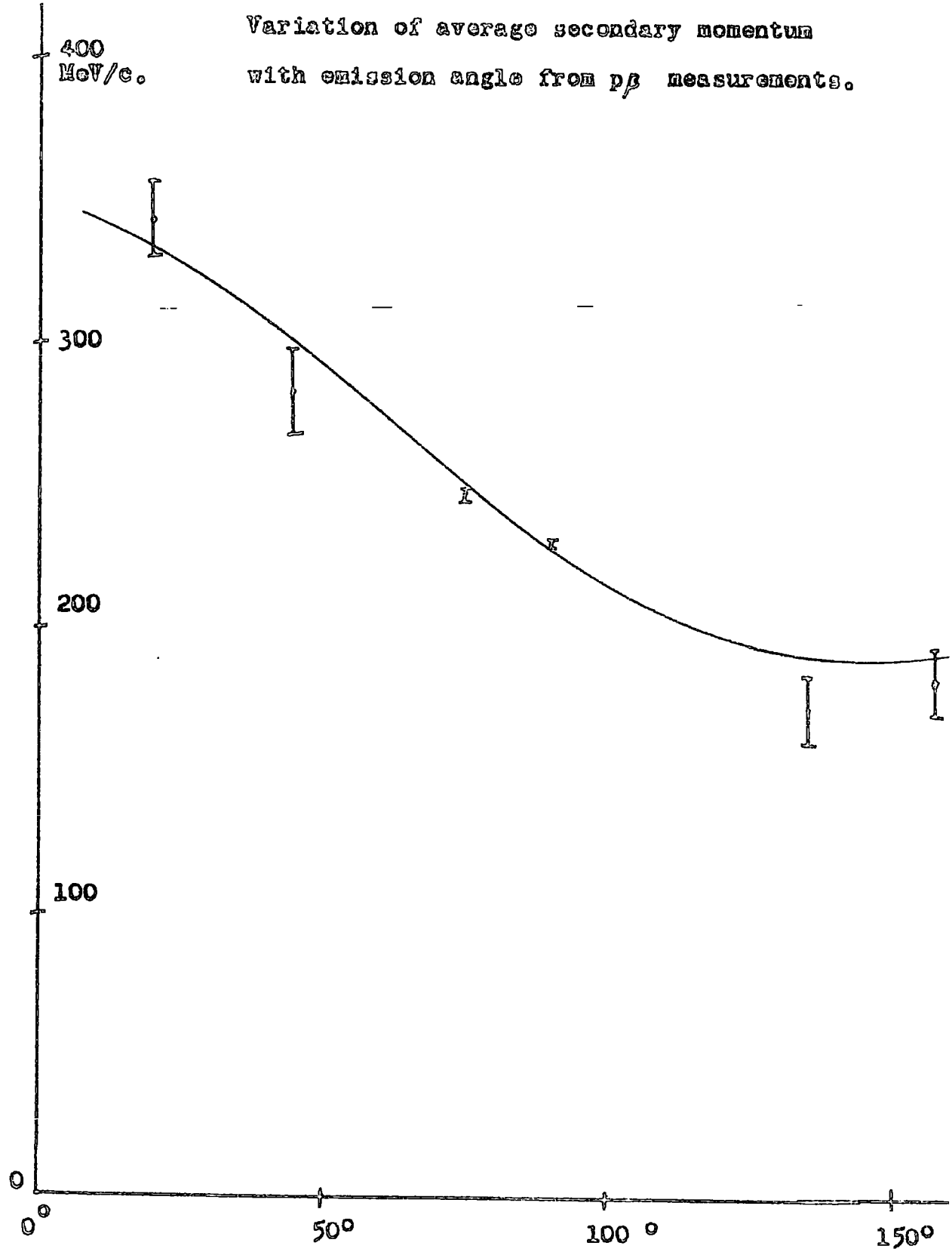

Figure 29.

The momentum spectra which provide the best fit to the channel density curves. A correction is then applied for scanning errors etc.

Momentum MeV/c.	C4 best fit	C4 corrected	C5 best fit	C5 corrected
100 - 150	15	18	2	3
150 - 200	10	12	20	19
200 - 250	7	7.9	33	33
250 - 300	4	4.4	20	17
300 - 350	2	2.2	5	5
350 - 400	1	1	3	3
400 - 450	0	0	2	1
450 - 500	0	0	0	0
mean p.	188 $\pm$ 20	185 $\pm$ 20	239 $\pm$ 10	234 $\pm$ 10

TABLE XVI

are compared in figure 30, normalised to equal areas.

For C4 the mean angle is 127°. If the results are compared with those at 135°, the mean momenta are seen to be compatible. As the pβ of only a small number of tracks was measured at 135° meaningful comparison of momentum distributions is impossible.

b) Conclusions on the technique. Scanning is much quicker of the spectrographic plates than by the conventional pβ method. The analysis of the present spectrographic exposure was made difficult by the high background, which could in future be avoided. Much of the background arose from scattering of the beam particles in the side of the magnet. The availability of a differently constructed magnet, a smaller face area for instance, would have reduced the background considerably, and made scanning easier, quicker and more efficient. The high background not only slowed up the task of achieving good statistics but also made it extremely difficult, almost impossible in plates 1 and 2, to pick out tracks of the right type.

A good beam is essential for both methods. In the spectrographic exposures, a higher flux of particles per

[illegible] of the recoils of Pb accelerated
[illegible] at 75°, and the recoils of Pb[illegible]

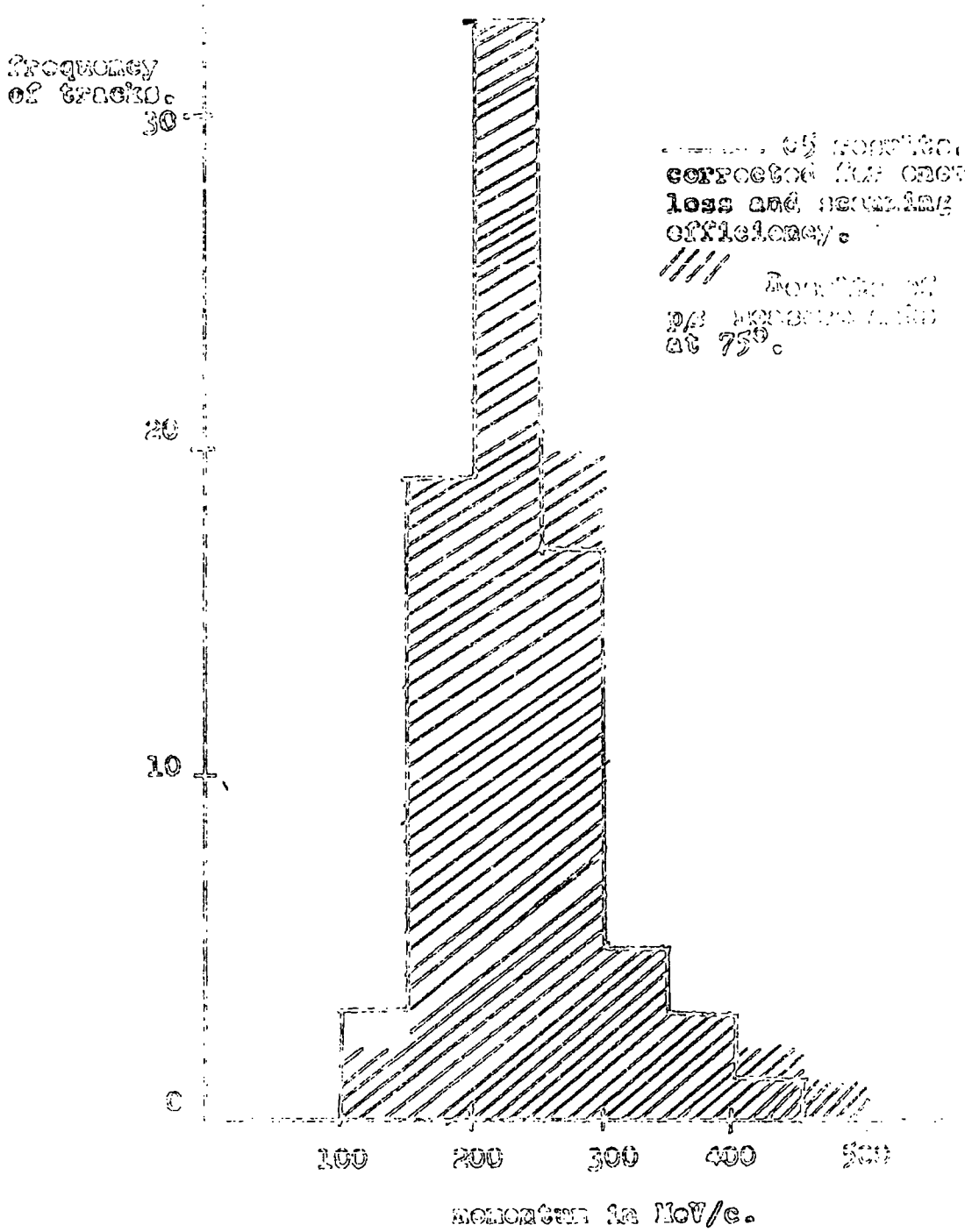

Figure 39.

unit area would be preferable. With such a higher flux and a sharper beam it would be possible to use a much smaller, thinner, target, and still obtain a reasonable flux of detectable secondaries. The shorter the path length of the particles in the target, the less absorption will take place (see chapter 2), thus reducing the uncertainty on the momentum. A smaller target area would also simplify the matrix in the Δx - X system of analysis, and simplify the range of the emission angles selected by each plate.

The method of analysis of the spectrographic plates, while needing good statistics, proved in fact simple to use. The matrix for each plate can be worked out beforehand and the particle positions entered on the Δx - X plot as the plate is scanned. Comparison with the conventional $p\beta$ exposure shows that the method is accurate.

Further use of this method would therefore require first of all the production of a high flux (of the order of 2×10^4 particles/sec cm^2) well-defined beam, and the use of a magnet whose structure allows the primary

beam to pass through unimpeded. All six plates of the spectrograph can then be used with a much smaller target volume (about 0.25 cm square horizontal cross-section). The great reduction in background should then render scanning much more efficient with a much higher signal to background ratio.

5. DISCUSSION OF THE RESULTS.

In chapter 4 the momenta of scattered pions were determined at angles of scattering around 75° and 127° using the emulsion spectrograph. The "conventional" exposure was made to check the results at 75°, and to confirm the use of the spectrograph. Further measurements were made at 90° with the conventional exposure, and at other angles, i.e. 20°, 45°, 135° and 155°; small numbers of tracks were measured to establish the variation of mean energy with angles of scattering.

In this chapter the distribution of pion momenta at fixed angles of scattering, and the distribution of mean momenta (or energies) as a function of the scattering angle are compared with the calculations that were described and summarised in chapter I, and with the Monte Carlo calculations of Bertini (1963). Evidence is sought for the effects of a) nucleonic momenta and to determine if possible their distribution, b) pion potentials, and c) the exclusion effect and its magnitude.

5.1. Distribution of Pion Momenta at Scattering Angles of 75° and 90°.

From figures 27 and 28 it can be seen that a distribution of nucleonic momenta is indicated, rather than a line spectrum from a stationary nucleon. Figure 2d shows the expected spread of secondary momenta at 90° using a nucleonic momentum distribution. The momentum spread is over some 300 MeV/c. The observed momentum spread at 90° is greater than this.

The type of exclusion principle applied was discussed in chapter I, section 10, where it was decided that the depth of the potential well, V, was the determining factor. Carbon has 4 nucleons in the $1s_{\frac{1}{2}}$ and 8 nucleons in the $2p_{3/2}$ (see 1.2, the shell model). Using Strnad's estimations of V_s and V_p (see 1.3), two-thirds of the nucleons require momentum transfers of greater than (40 - KE) MeV, and the remaining nucleons of greater than (79 - KE) MeV. If the average kinetic energy is 20 MeV, the average energy loss to the nucleons is therefore 43 MeV.

a) Bertini's Monte Carlo calculations. Bertini

(1963) performed a series of nuclear cascade calculations, assuming a varying nuclear density. A pion potential was incorporated, which was equal to the potential of the nucleon with which it was interacting. The nuclear potential being in fact 7 MeV greater than the corresponding zero temperature Fermi energy (see section 1.5).

Bertini ran his Monte Carlo calculations for 300 MeV π^- - C interactions (private communication). Our incident energy was 285 MeV, so assuming that over such a short range the variations are proportional, the results have been scaled. The energy - angle distribution is shown on figure 38 and there is good agreement with our results.

The angular distribution from the Bertini calculations is shown in figure 31. In figure 32, a comparison is made of the predicted energy distribution and the observed one at 90°. The comparison is only fair. As with other π-nucleon calculations (see Bertini 1963), the observed peak is at a much lower energy than the predicted peak. The observed peak includes some

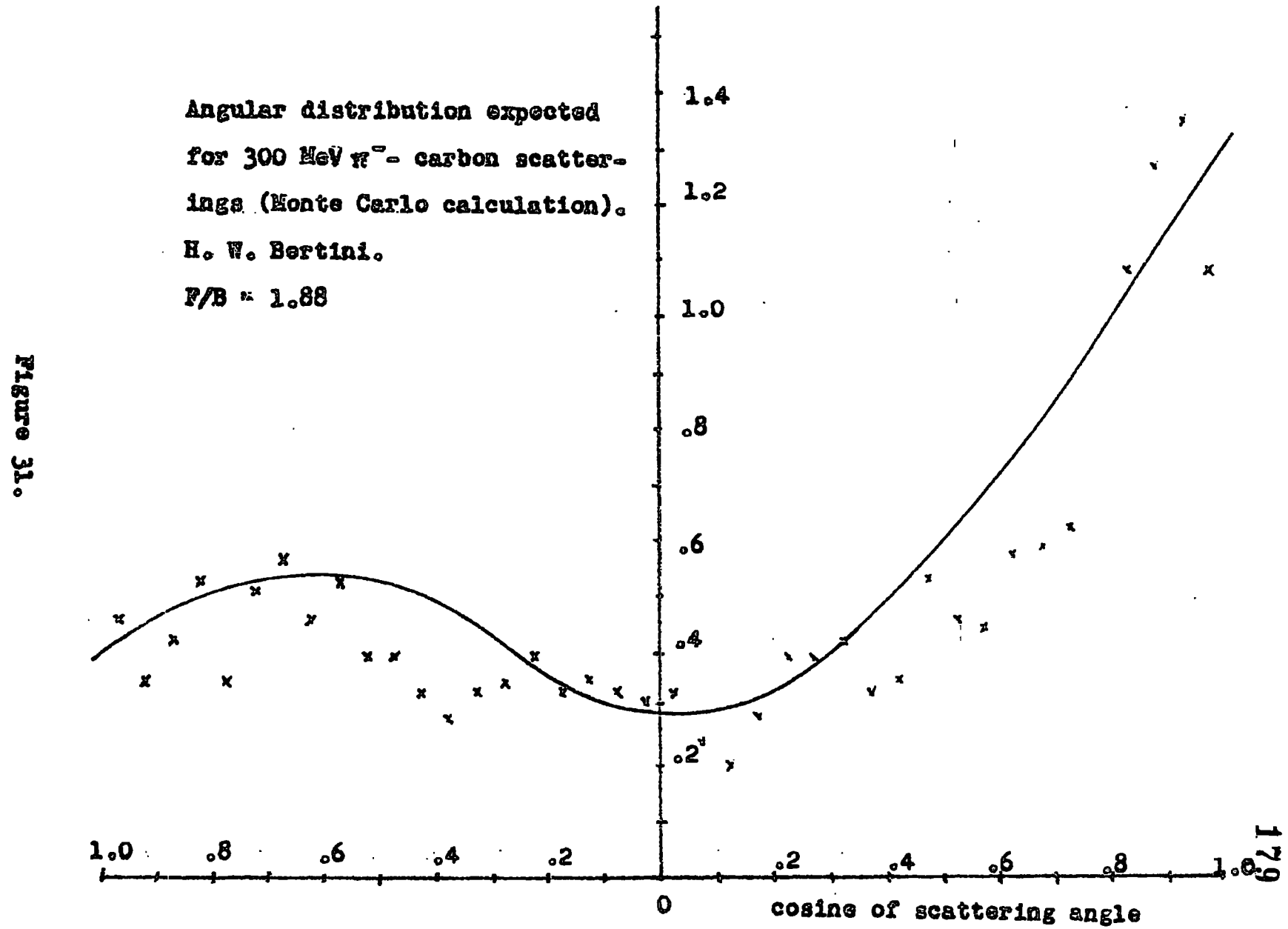
Angular distribution expected
for 300 MeV π⁻- carbon scatter-
ings (Monte Carlo calculation).
H. W. Bertini.
F/B = 1.88
1.4
1.2
1.0
.8
.6
.4
.2
1.0
.8
.6
.4
.2
0
.2
.4
.6
.8
1.0
cosine of scattering angle

Figure 31.

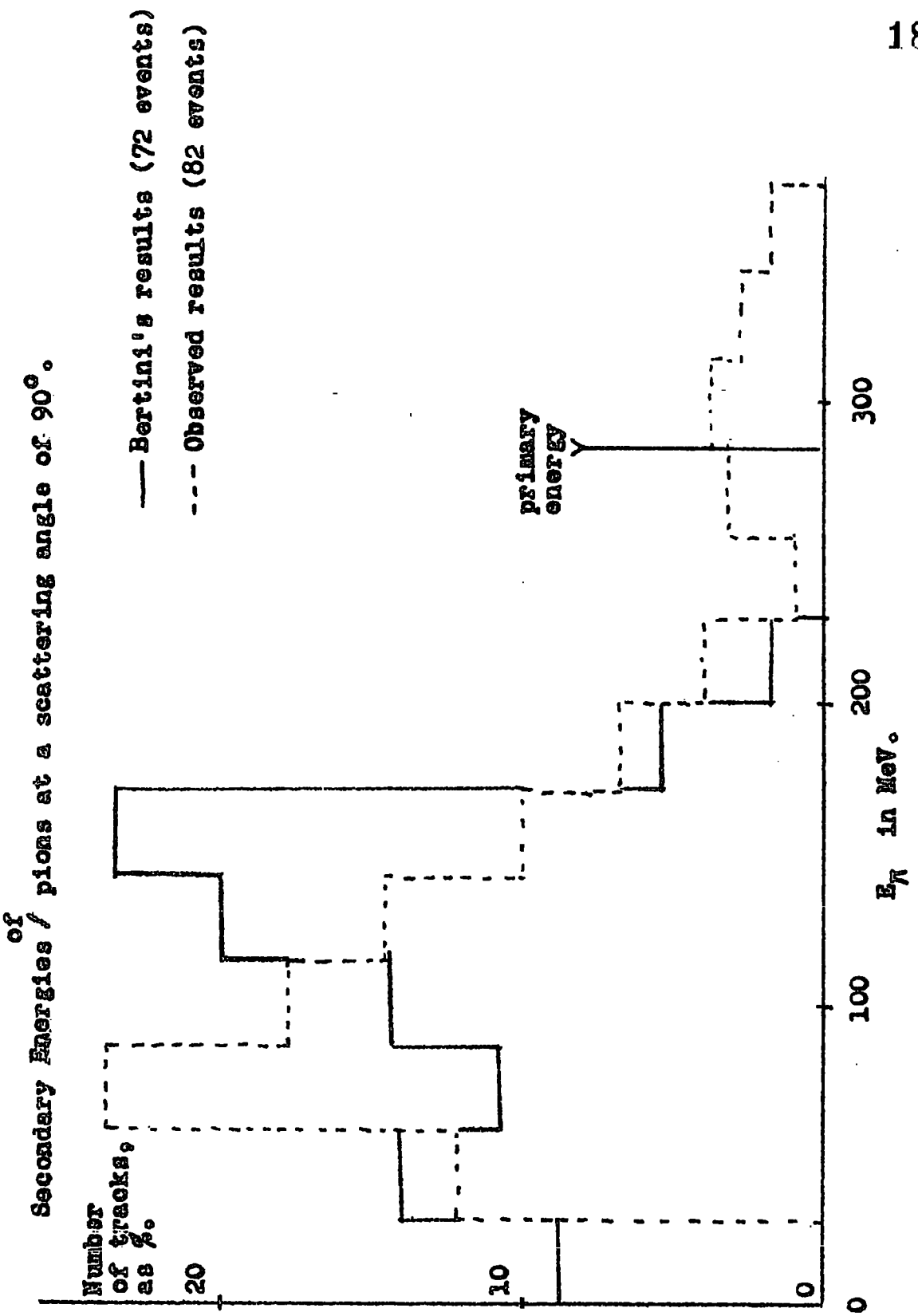
Secondary Energies of π pions at a scattering angle of 90°.
—— Bertini's results (72 events)
--- Observed results (82 events)
primary energy
Number of tracks, as %.
20
10
0
0
100
200
300
E_π in MeV.

Figure 32.

pions of high estimated energy, which the restrictions on the calculations do not allow to occur. The difference between the peaks is about 90 MeV and therefore outside the range of the postulated exclusion principle effect for one nucleon.

b) Momentum distribution of nucleons and pion potential. As stated in chapter I, three possible nucleonic momentum distributions have been considered; the Fermi, the Gaussian and a composite Gaussian. In many instances the Gaussian results were identical with those from the Fermi, and never differed very much from the calculations using one of the other two distributions.

In figures 33 and 34 are shown the results of pβ measurements at 90° compared with the expected results for two nucleonic momenta distributions. One distribution is the Fermi with a p_{max} of 225 MeV/c (KE = 12.8 MeV) as an average for all nucleons. The other is the composite Gaussian with a p_{max} of 275 MeV/c (average nucleonic KE = 18.6 MeV). For the composite distribution raising p_{max} to 425 MeV/c, alters only slightly the expected distribution of secondary pion

Comparision of Momentum Spectra of Pions Scattered through 90°.

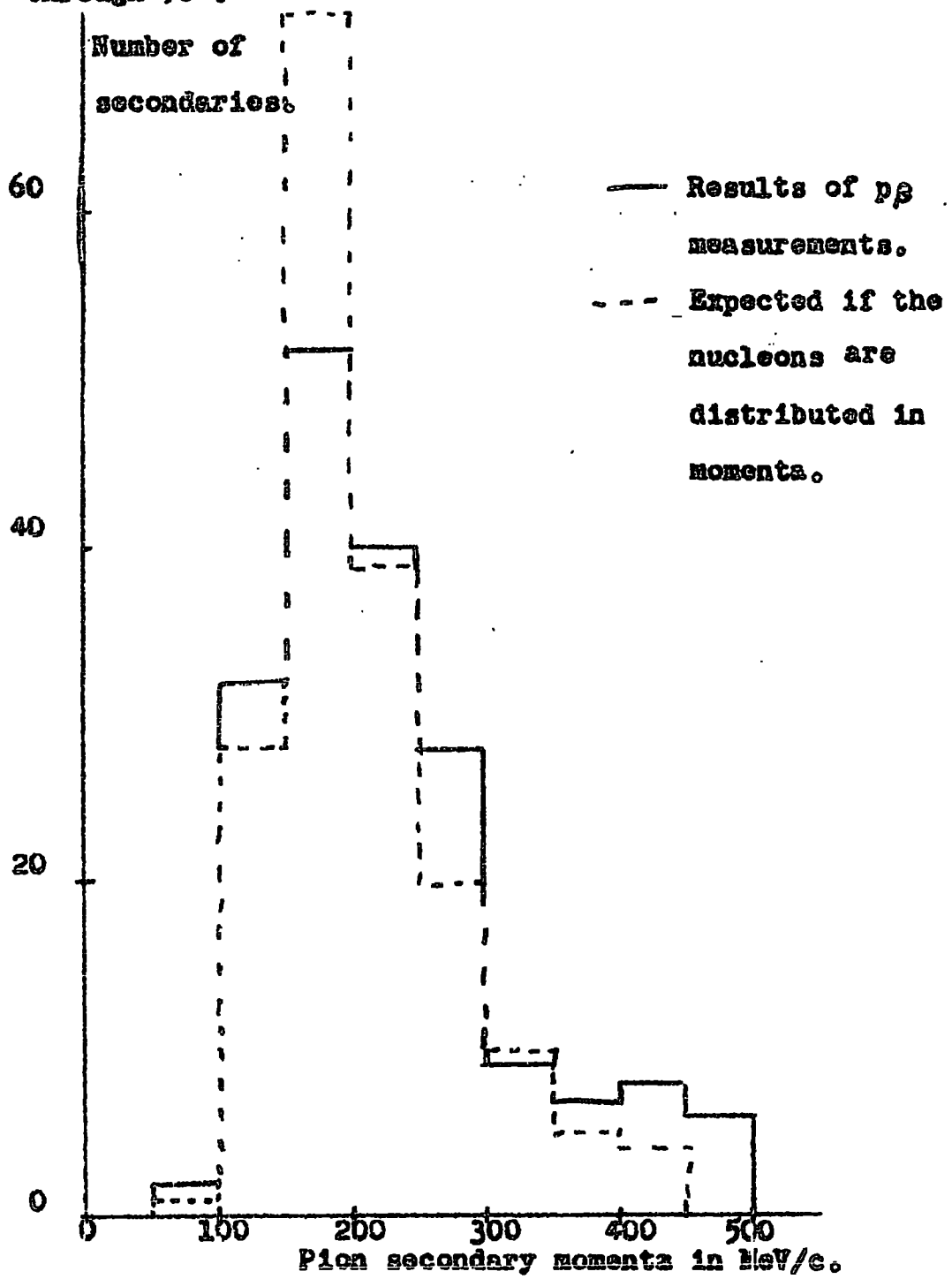

Nucleonic momentum distribution is assumed to be a composite Gaussian. Same total number of events for each.

Figure 33.

Comparision of Momentun Spectrum of Pions Scattered through 90^{o}.

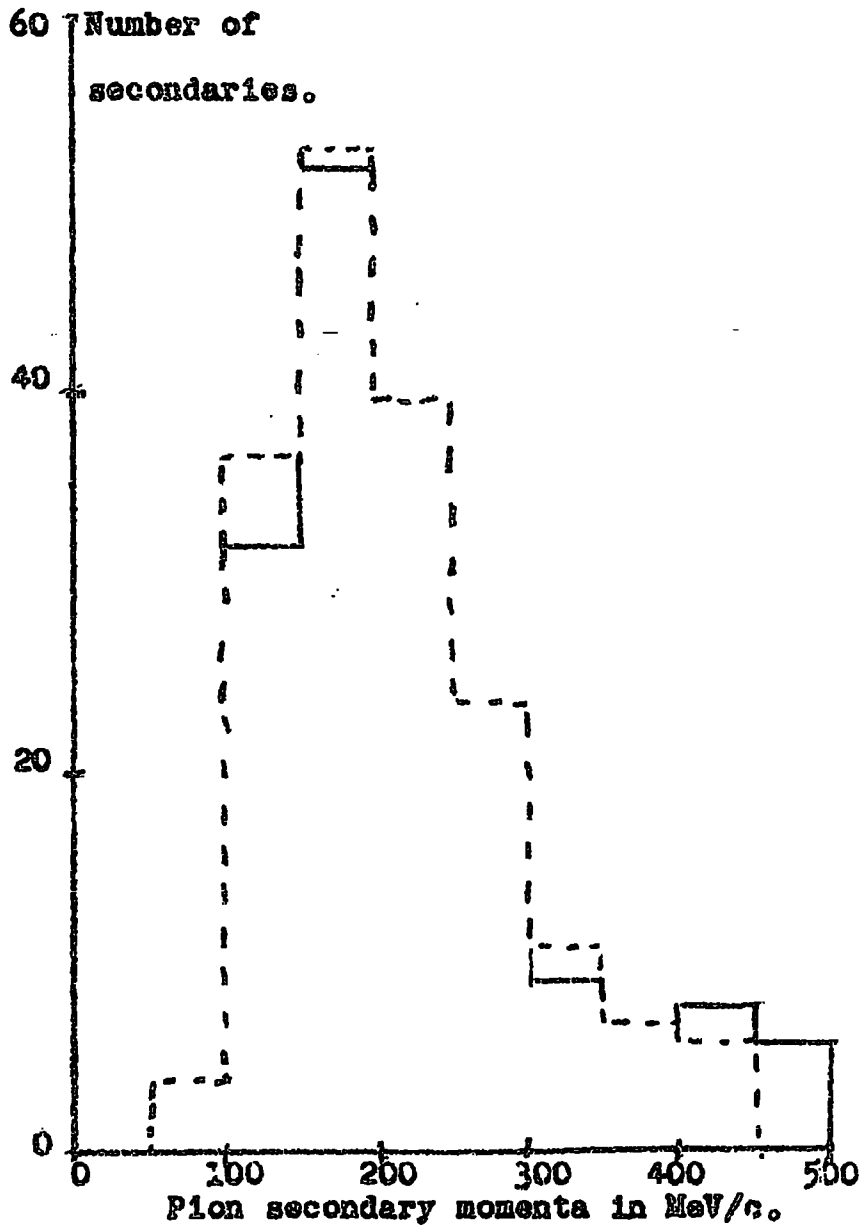

—— Results of $p\beta$ measurements. - - - - Expected if the nucleons have a Fermi distribution of momenta. Same total number of events for each.

Figure 34.

momenta, but raises the average nucleonic kinetic energy to 24 MeV, which is rather higher than expected (see section 1.3). Both the distributions shown in figures 33 and 34 were obtained by assuming that under the influence of the potential, the pion energy at the moment of impact is 260 MeV (see section 1.10) and after the collision there is a further potential effect as the pion leaves the nucleus. The laboratory energy is estimated from the curve in figure 2c. Both distributions fit better than Bertini's, but the Fermi gives the better fit.

At 75° (see figures 35 and 36) the fits for the two distributions to the observed histogram are again good.

A momentum distribution of the nucleons will therefore explain the spread in secondary momenta, if in addition the pion potential is considered. This potential both tends to shift the peak of the momentum distribution at any given scattering angle, and effectively increases the momentum spread.

Momentum Spectrum of Pions Scattered through 75°.

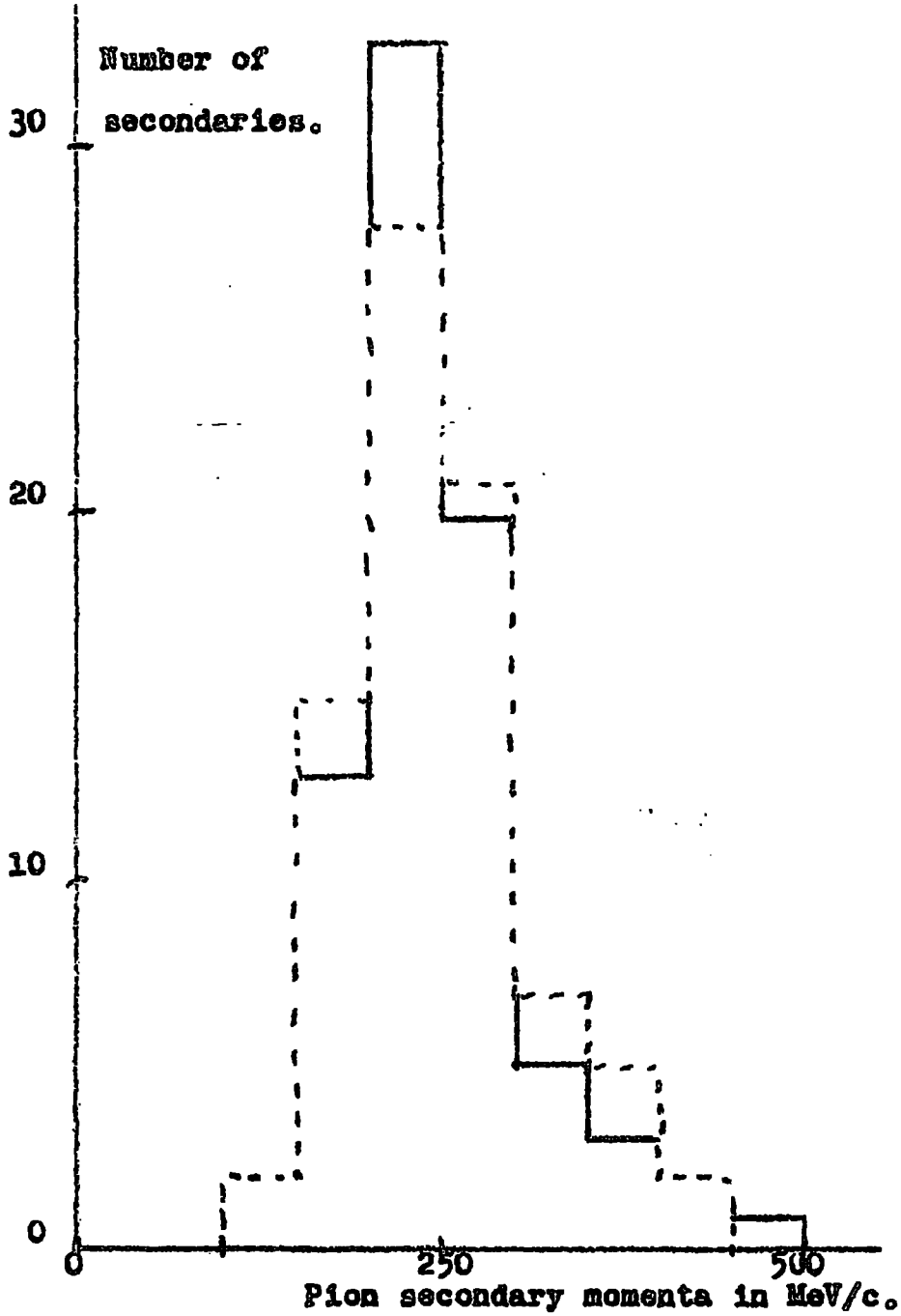

— Results of $p\beta$ measurements. --- Expected if the nucleons have a composite Gaussian distribution of momenta. Same total number of events for each.

Figure 35.

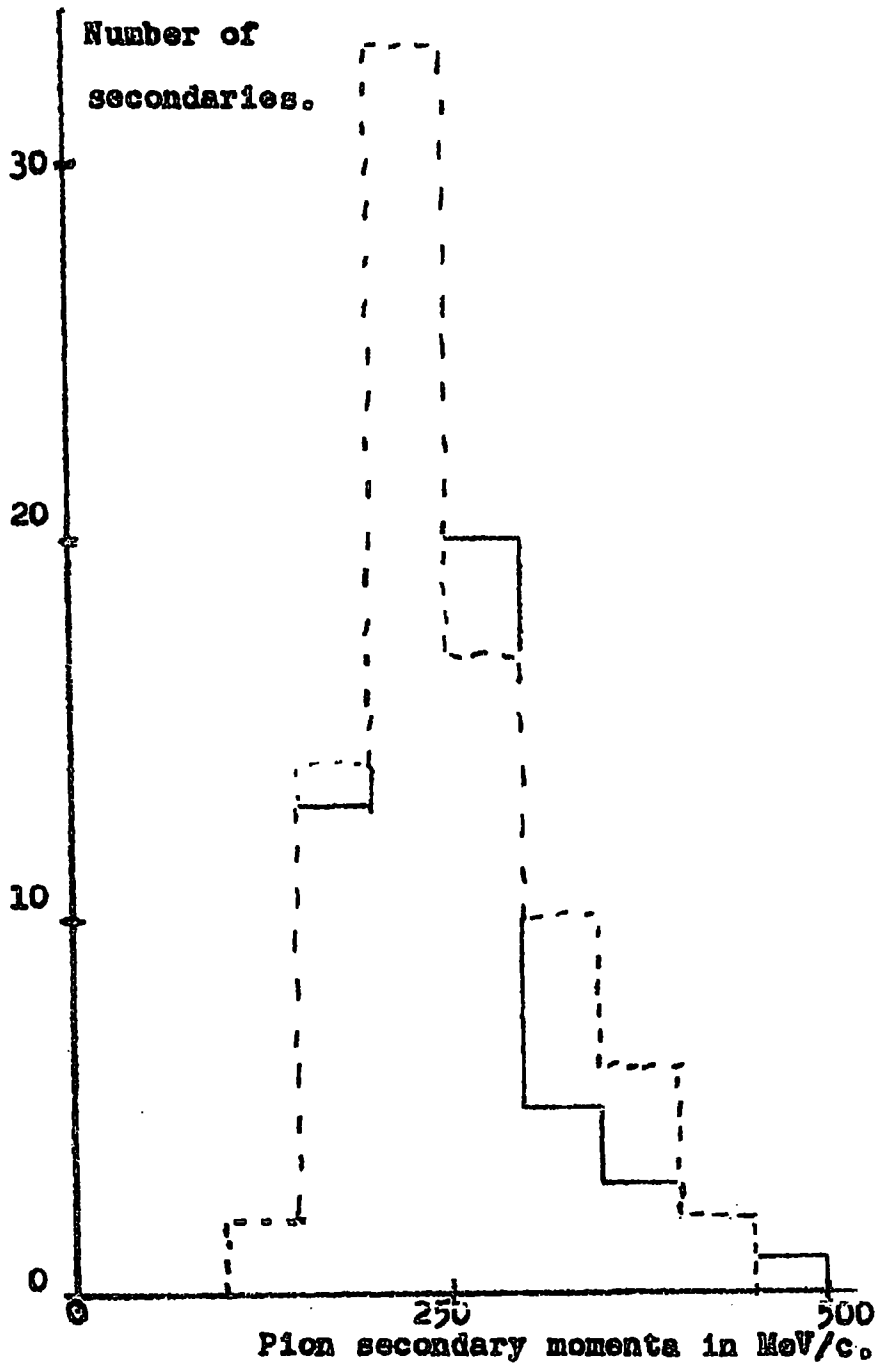

— Results of pp measurements. - - - Expected if the nucleons have a Fermi distribution of momenta. Same total number of events for each.

Figure 36

5.2. Variation of Momentum and Energy with Scattering Angle.

In figure 37 the results for the variation of momentum with emission angle are shown. The dotted curve shows the results expected for scattering off a stationary proton. The general shape of the curve is followed by the experimental results, but the observed energy of the scattered pion is consistently less than that expected from free proton scattering.

In figure 38 the results are compared with the expected curve if a distribution of nucleonic momenta is assumed and the pion potential effect is taken into account (see figure 2a). The general agreement is good in the backward, but bad in the forward direction. The potential effect for the average energy is not dependent on the particular momentum distribution chosen.

In figure 39 the results expected for the calculations are shown with an exclusion effect (see section 5.3) in addition to the pion potential. This exclusion effect depends upon the depth of the nuclear well and the nucleonic momenta within the nucleus.

Variation of Secondary Momentum with Scattering Angle.

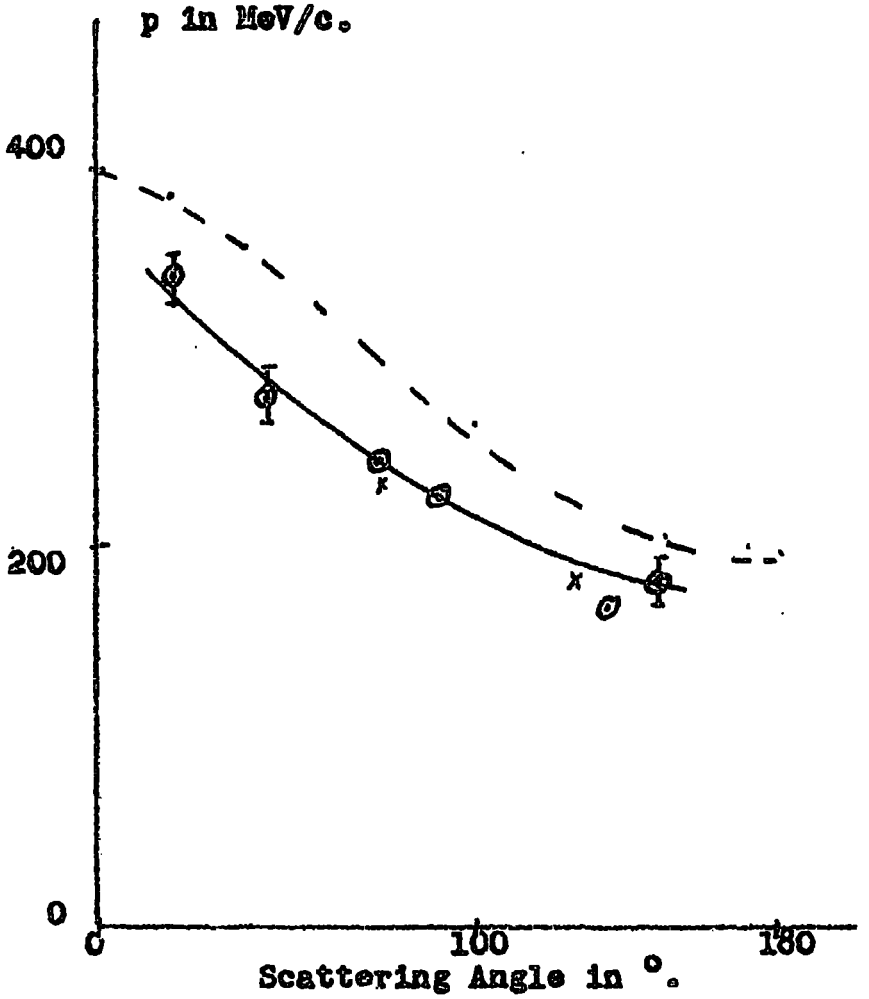

⊙ - Results of pβ measurements. × - results of spectrographic exposure. - - - expected results if target is a stationary nucleon.

Figure 37.

Variation of secondary pion energy with scattering angle.

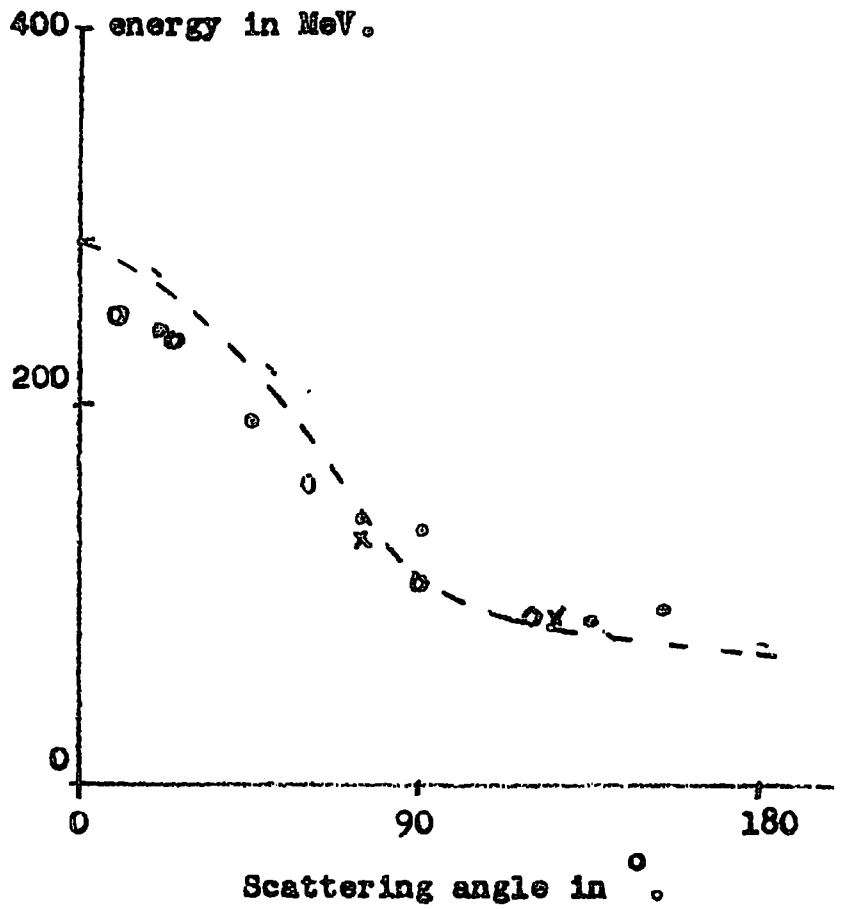

o - Results of pβ measurements. x - results of spectrographic exposure. O - Bertini's results. - - - - Expected curve if 290 MeV pion is acted upon by a pion potential in the nucleus, nucleonic momentum ~~m~~ has negligible effect.

Figure 38.

Variation of secondary pion energy with scattering angle.

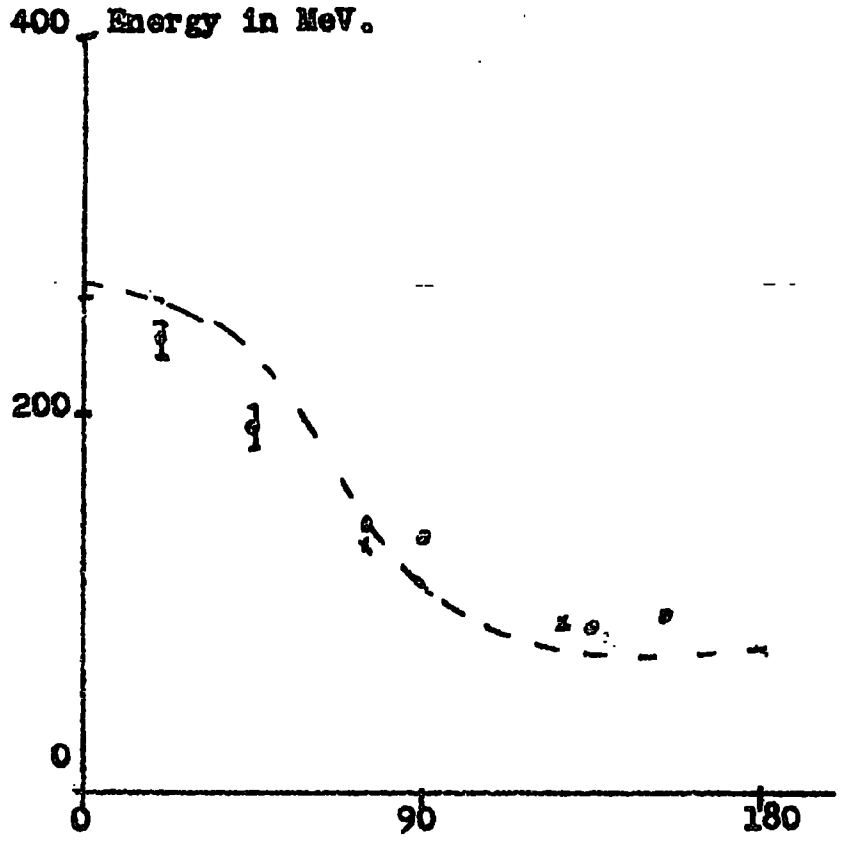

Scattering angle in degrees.

ϕ - Results of $p\beta$ measurements. $\times$ - results of spectrographic exposure. - - - Expected curve if the nucleons have a composite Gaussian momentum distribution, and the pion is acted upon by a pion potential and the exclusion principle applies with a well depth of 53 MeV.

Figure 39.

The results of Bertini's Monte Carlo calculations are shown on the same graph. All give good agreement with one another.

Comparison with other results. Belovitskii (1959) measured the scattering angles and energies of 300 MeV π^- and π^+ in G5 emulsion. In figure 40, the average energy of the scattered meson is shown from Belovitskii's results. These are to be compared with our results at 285 MeV in figure 38. Generally the Belovitskii data give a lower average energy and thus a greater energy transfer. The statistics are not good enough to permit comparison of the energy distributions over a given angular range.

Belovitskii's average energy was 133 MeV. Since only tracks 1500μ long had measurements made on them, there is a lower cut-off in the region of 60 MeV. The forward-backward ratio was, $F/B = 1.15 \pm 0.1$ (all $E\pi > 60$ MeV). Only a third of the particles which should be forward scattered were found (see comparison with the results of Finney et al. below).

Conclusion. The results of scattering experiments

Variation of secondary pion energy with scattering angle, from the data of G.E. Belovitskii (1959)

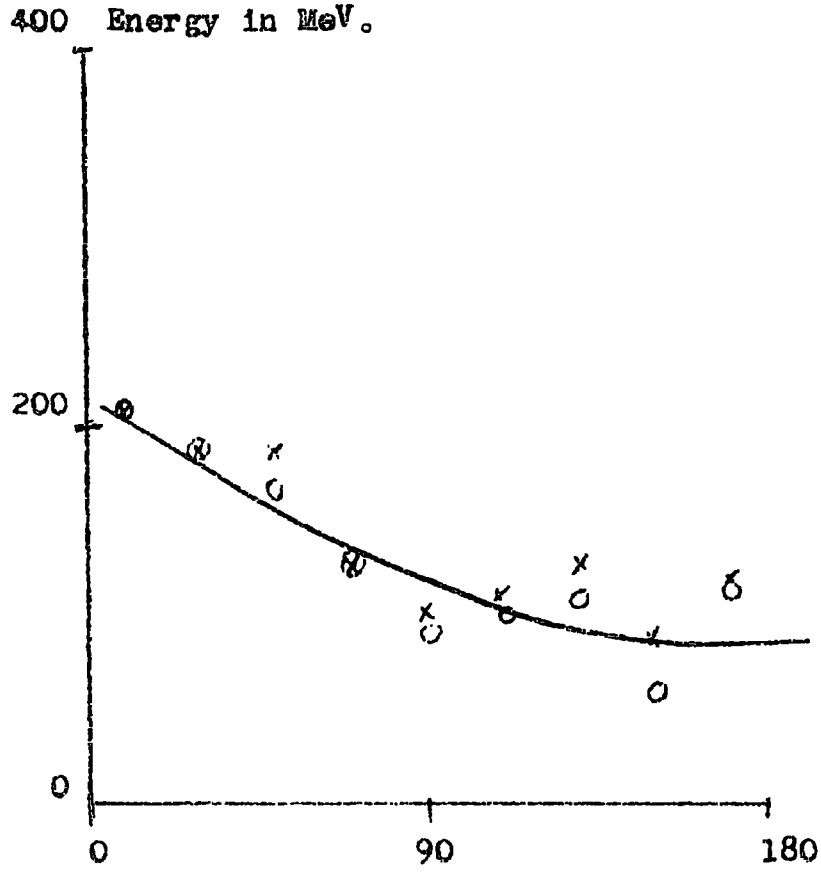

π-π^+ - with energy greater than 125 MeV. (90 in all).

o -all π^- particles.

Figure 40

require the struck nucleons to be distributed in momenta within a potential well, and an exclusion principle depending on the depth of the nuclear potential well applies.

5.3. The Pauli Exclusion Principle.

Since both the Fermi distribution and the composite Gaussian distribution account for the reduction in mean energy and scattering of pions, it is of interest to calculate the reduction in cross-section.

As already stated an exclusion principle which requires the nucleon to escape with greater than a given minimum momentum, did not give the observed decrease in mean energy at low scattering angles. If however V is assumed to be 53 MeV (average for carbon s and p nucleons), then the decrease shown in figure 39 is obtained. If energy transfers of less than the required amount to escape from the well are forbidden then at both 75° and 90° only a very small effect is expected. Calculations made using both the Fermi and composite Gaussian distributions, revealed that the forbidden transfers

occurred only at emergent pion mementa at 275 MeV/c and above, and at the most reduce the expected frequency by one-sixth.

The effect of the exclusion principle via the composite Gaussian distributions with a maximum momentum of 275 MeV/c, is to reduce the pion nucleon cross-section by 64%, and to give a forward/backward ratio of 0.89 ± 0.1. The Fermi distribution when the exclusion principle was applied gave a cross-section reduction of 62%, and a forward/backward ratio of 1.00 ± 0.1. This can be compared with the results of Finney et al. (1962) who concluded that the deviation of pion-complex nuclei interactions from the prediction of the optical model of the nucleus required a reduction of the pion nucleon cross-section by 63%, and forward/backward ratio of 1.1 ± 0.35 (all $E\pi > 85$ MeV). The average energy of the secondaries was 164 ± 26 MeV. The statistics were too low (80 tracks over complete 180° range) to compare in detail. Altogether the results of Finney et al. and of Belovitskii (see 5.2) are in good agreement with our results using either momentum distribution and the exclusion principle.

By contrast the forward/backward ratio from Bertini's calculations is 1.88 without any cut-off, and the ratio would be increased if any low energy cut-off were applied. If it is assumed that forward scatters of less than 20° are rarely detected then the Bertini ratio does drop to 1.16, but this is a very unlikely assumption as 20° is an easily detected scatter.

5.4. Conclusion and Summary

The results quoted here are consistent with the pion being acted upon by a potential of the order of 30 MeV. The potential is energy dependent. The angular distribution agrees well with Bertini's predictions. Bertini has in fact used a nuclear momentum distribution which approximates to a Gaussian with a kT value of 15 MeV. This value agrees well and lies within the range of α values quoted in 1.3.4 (Azhgirey, 1959).

The momentum results at 90° are not however compatible. Our results have a much greater high energy tail, whereas the Bertini results have a sharp cut-off

on the high energy side. It is obvious that in some interactions much more energy is transferred to the nucleus than is allowed for on Bertini's model. It would seem that the pion potential and well depth used by Bertini are not large enough. However, if the spread above 285 MeV (figure 32) is taken as an indication of the general error at high pβ measurements, then the average energy is lowered slightly in figure 38, but the distribution peak in figure 32 remains at 80 MeV.

Assuming a range of nucleonic momenta from 0 to 275 MeV/c and using experimentally determined pion potentials we can obtain a better fit to the results at 90° than Bertini's model, and this fit is also good at 75°. The exclusion principle has however, a negligible effect at these two angles.

Summary.

a) Momentum distribution.

The nucleons have a range of momenta from 0 to at least 275 MeV/c. Extending the composite Gaussian to 425 MeV/c

makes only a small difference to the parameters discussed here. The biggest difference is in the average nucleon energy, raising it from 20 to 24 MeV. Measurements at small scattering angles may lead to a determination of the momentum distribution. The two alternatives found suitable so far are:

$N(p) \propto p^2$ the Fermi distribution.

$N(p) \propto p^2 e^{-p^2}/(191)^2$ the composite Gaussian distribution.

b) Pion potentials.

A potential in the region of 30 MeV, which is very sensitive to the pionic energy is needed to explain the experimental results. The function used is shown in figure 2c.

c) Pauli Exclusion Principle.

An exclusion principle is applied such that the struck nucleon must receive (53 - KE) MeV is the reaction is allowed. The exact value of the nucleonic potential has not been determined, 53 MeV having been averaged from the calculations of Strnad, but it gives reasonable agreement

with the experimental results (see figure 39).

Acknowledgements

The author wishes to thank Professor G.D. Rochester for his interest and encouragement and provision of facilities. The author is indebted to Dr. J.V. Major and Dr. A.J. Apostalakis for constant help and fruitful discussion, for doing most of the pβ measurements and for checking many calculations.

Dr. H.W. Bertini very kindly ran his π-nucleus Monte Carlo program at 300 MeV so that it could be compared with the results reported here.

The author would also like to thank: the staff of the Computing Laboratory of the University of Newcastle-on-Tyne, especially Miss E. Barrington, for much help during the initial stages of programming; Mrs. E. Templeton of the Computing Laboratory, the University of Durham; Mr. D. Jobling of the physics department workshop for constructing the spectrograph; the members of the various groups at CERN whose advice we sought especially Dr. Michaelis, Mr. M. Roberts and Dr. L. Hoffmann; and past and present members of the emulsion group, namely, Dr. G.A. Briggs, Mrs. E. Errington, Dr. P.J. Finney, Professor N.A. Kahn and C. Kitchen.

Finally the author would like to gratefully acknowledge the Department of Science and Education for the provision of a research studentship without which the work would not have been done.

REFERENCES

Ajzenberg-Selove, F. and Lauritsen, T., 1959, Nuclear Phys. 11, 1.

Allen, J.E., Apostalakis, A.J., Lee, Y.J., Major, J.V. and Perez Ferreira, E., 1959, Phil. Mag., 4, 858.

Allen, J.E., Apostalakis, A.J., Lee, Y.J., Major, J.V. and Perez Ferreira, E., 1961, Phil. Mag., 6, 833.

Allen, J.E. and Apostalakis, A.J., 1961, Proc. Roy. Soc. A., 265, 117.

Ashkin, J., Blaser, J.P., Feiner, F. and Stern, M.O., 1956, Phys. Rev., 101, 1149. CERN Symposium II 1956, p. 225.

Ashkin, J., Blaser, J.P., Feiner, F. and Stern, M.O., 1957, Phys. Rev., 105, 724.

Azhgirey, L.S., Vzorov, I.K., Zrelov, V.P., Mescheryakov, M.G., Neganov, B.S., Ryndin, R.M. and Shabudin, A.F., 1959, Nuclear Phys., 13, 258.

Baqui Beg, M.A., 1960, Phys. Rev., 120, 1867.

Barkas, W.H., 1958, Nuovo Cim., 8, 201.

Belovitskii, G.E., 1959, Soviet Phys. JETP., 8, 581.

Bertini, H.W., 1963, Phys. Rev., 131, 1801.

Braunersreuther, E., Chabaud, V., Delorme, C. and Morpurgo, M., 1961, C.E.R.N. reprint, 61 - 12, p. 12.

Brueckner, K.A., 1958, Rev. Mod. Phys., 30, 561.

Chew, G.F. and Goldberger, M.L., 1950, Phys. Rev., 77, 470.

Clarke, J.O. and Major, J.V., 1957, Phil. Mag., 2, 37.

Deahl, J., Derrick, M., Fetkovich, J., Fields, T. and Yodh, G.B., 1960, Proceedings of the 1960 Annual International Conference on High Energy Physics at Rochester, p. 185.

Deahl, J., Derrick, M., Fetkovich, J., Fields, T. and Yodh, G.B., 1961, Phys. Rev., 124, 1987.

Elton, L.R.B. and Gomes, L.C., 1957, Phys. Rev., 105, 1027.

Fernbach, S., Serber, R. and Taylor, T.B., 1949, Phys. Rev., 75, 1352.

Feshbach, H., Porter, C.E. and Weisskopf, V.F., 1954, Phys. Rev., 96, 448.

Feshbach, H. and Weisskopf, V.F., 1949, Phys. Rev., 76, 1550.

Finney, P.J., Major, J.V. and Parkhouse, P.G.J.T., 1962, Phil. Mag., 7, 237.

Garron, J.P., Jacmart, J.C., Riou, M. and Ruhla, Ch., 1961, Journ. de Phys., 22, 622.

Garron, J.P., Jacmart, J.C., Riou, M., Ruhla, C., Teillac, J. and Strauch, K., 1962, Nuclear Phys., 37, 126.

Glauber, R.J., 1956, Physica, 22, 1185.

Gooding, T.J. and Pugh, M.G., 1960, Nuclear Phys., 18, 46.

Gottschalk, B. and Strauch, K., 1960, Phys. Rev., 120, 1005.

Haxel, O., Jensen, J.H.D. and Suess, H.E., 1949, Phys. Rev., 75, 1766L.

Helland, J.A., Devlin, T.J., Hagge, D.E., Longo, M.J., Moyer, B.J. and Wood, C.D., 1962, 1962 International Conference on High Energy Physics at C.E.R.N. p. 3.

Henley, E.M., 1952, Phys. Rev., 85, 204.

Hofstadter, R., 1956, Rev. Mod. Phys., 28, 214.

James, A.N. and Pugh, H.G., 1962, Nuclear Phys., 42, 441.

Karplus, R. and Yamaguchi, Y., 1961, Nuovo Cim., 22, 588.

Kellman, S., Kovacik, W.P. and Romanowski, T.A., 1963, Phys. Rev., 129, 365.

Kim, Y.S., 1963, Phys. Rev., 129, 1293.

Maris, T.A.J., Hillman, P. and Tyren, H., 1958, Nuclear Phys., 7, 1.

Mayer, M.G., 1949, Phys. Rev., 75, 1969L.

Metropolis, N., Bivins, R., Storm, M., Turkevich, A., Miller, J.M. and Friedlander, G., 1958, Phys. Rev., 110, 185.

Metropolis, N., Bivins, R., Storm, M., Miller, J.M., Friedlander, G. and Turkevich, A., 1958, Phys. Rev., 110, 204.

Nikol'skii, B.A., Kudrin, L.P. and Ali-Sade, S.A., 1957, Soviet Phys., JETP., 5, 93.

Oda, N. and Harada, K., 1958, Nuclear Phys., 7, 251.

Sarjant Singh and Alexander, J.M., 1962, Phys. Rev., 128, 711.

Sternheimer, R.M., 1959, Phys. Rev., 115, 137.

Strnad, J., 1962, Nuclear Phys., 35, 451.

Tyren, H., Hillman, P. and Maris, T.A.J., 1958, Nuclear Phys., 7, 9.

Watson, K.M. and Zemach, C., 1958, Nuovo Cim., 10, 452.

Winsberg, L. and Clements, T.P., 1960, Phys. Rev., 122, 1623.

Yuan, L.C.L., 1956, CERN Symposium, 1956, 2, 195.

Zhdanov, A.P. and Fedotov, P.I., 1961, Soviet Phys., JETP., 14, 1330.

Zinov, V.G. and Korenchenko, S.M., 1959, Soviet Phys., JETP., 36, 429.